Dynamics of molecular beams in a traveling-wave Stark decelerator

Zapara, Artem

Dynamics of molecular beams in a traveling-wave Stark decelerator

Artem Zapara

university of groningen / faculty of science and engineering / van swinderen institute for particle physics and gravity

Nederlandse Organisatie voor Wetenschappelijk Onderzoek

This work is part of a research program VIDI 680-47-519 funded in part by the Stichting voor Fundamenteel Onderzoek der Materie (FOM), which is financially supported by the Nederlandse Organisatie voor Wetenschappelijk Onderzoek (NWO).

ISBN: 978-94-034-1647-2 (printed version)
ISBN: 978-94-034-1646-5 (electronic version)

Cover design: Artem Zapara
Cover image: Simulated propagation of the molecular beam throughout the Stark decelerator in guiding mode of operation.
Printed by: Gildeprint - Enschede

university of groningen

Dynamics of molecular beams in a traveling-wave Stark decelerator

PhD thesis

to obtain the degree of PhD at the
University of Groningen
on the authority of the
Rector Magnificus Prof. E. Sterken
and in accordance with
the decision by the College of Deans.

This thesis will be defended in public on

Friday 24 May 2019 at 12.45 hours

by

Artem Zapara

born on 9 February 1989
in Mishelevka, Russia

Supervisor
Prof. S. Hoekstra

Co-supervisor
Prof. K.H.K.J. Jungmann

Assessment Committee
Prof. G. Palasantzas
Prof. E. Pallante
Prof. W.M.G. Ubachs

Contents

1

Introduction

The driving force of many particle physics experiments is to test the validity of our present understanding of nature. One of the theories that describes the properties of the Universe at the microscopic level is the Standard Model (SM). It is a theoretical framework that includes three out of four known fundamental interactions and categorizes all known fundamental particles [1]. The SM was developed in the 1960s by Glashow, Weinbeng and Salam [2–4] and is currently one of the most accurate physics theories. Its predictions and consequences have been extensively tested in many experiments for several decades with high accuracy. The success of this theory came after the experimental demonstration of the existence of all predicted elementary particles, including the first observation of the Higgs boson in 2012. Despite its huge predictive power, the SM is not considered complete, since it does not incorporate some fundamental properties of our Universe and cannot adequately explain a series of important observations. The main shortcomings of this theory are missing gravity, dark matter and dark energy. Moreover, the SM cannot explain in an appropriate way matter-antimatter asymmetry. In the previous years, many speculative theories appeared to account for the missing terms in the SM equations, and hence their extensions or modifications are natural and inevitable. The modified versions of the SM typically involve the existence of new, yet undiscovered particles or new hidden dimensions. One of the extension theories, supersymmetry, tries to explain observable discrepancies by introducing hypothetical supersymmetric particles. Several theories beyond the SM can already be rejected by high-accuracy experiments. Others still need to be confirmed or ruled out by a new generation of fundamental physics tests, where more stringent limits can be set and where higher experimental precision is involved (see e.g. [5, 6]).

Two approaches exist to search for physics beyond the Standard Model (BSM). The first one is a direct probe of physics at high energy scales by colliding particles at high energies (∼10 TeV), as it is performed at the Large Hadron Collider. This can possibly lead to the production of new particles or the observation of new phenomena. This approach, however, is limited by challenging technologies, such as constraints on achievable magnetic fields, engineering challenges in cryogenics etc. [7]. Another approach is table-top experiments with high precision where physics at even higher energy scales can be probed by performing BSM-sensitive tests. In order to perform such a test, one has to find a system sensitive to possible "New Physics", and this sensitivity can be manifested by a difference in the observable parameters from the SM predicted values. Among many quantities, experimenters have advanced the most in measuring the energy difference between atomic or molecular levels, i.e. the transition frequencies. The main idea is to measure the energy level structure of an atom or a molecule very accurately and compare the results with the prediction of theory. The best coincidence between measured and predicted values should indicate that the corresponding model is the best description of the Universe, until proven otherwise. In the process of searching for new valid theories, the SM has passed all sophisticated tests in numerous experiments. However, there are still many ways to go beyond the current limits. In this thesis, we focus on the possibilities that contribute to this field using cold molecules.

From an experimental point of view, the statistical uncertainty of a table-top high-precision spectroscopic measurement depends on three parameters: the number of species that can be probed, the interrogation time, and the intrinsic sensitivity of the system to a new effect in question. The first two parameters can be optimized by improving the control over the experiment, while the latter comes from theoretical studies of the relevant parameters of the system. Thus, one should look for an atomic system that possesses the required internal properties and can be efficiently manipulated in the laboratory in preparation for the ultimate experiment. It turned out that some molecules have an internal structure giving rise to their enhanced sensitivity to "New Physics". On the other hand, molecules are typically more difficult to manipulate in the laboratory compared to atoms because of their extra rotational and vibrational degrees of freedom. Hence, during the selection of a candidate molecule for an experiment, one has to take into account the level of complexity of the molecule and its susceptibility to external control. In practice, control is achieved by means of external electric and magnetic fields, or by laser light.

In our group at the Van Swinderen Institute in the University of Groningen, we have developed techniques to decelerate heavy diatomic molecules. In the large class of such molecules, we are interested mostly in the alkaline-earth monohalides

(SrF, BaF), since they have all necessary features to be promising candidates for new fundamental physics tests. These molecules are effectively single valence electron systems with a sizable electric dipole moment[1], whilst the large mass of the alkaline-earth constituent is important for enhanced sensitivity to "New Physics". Typical molecular sources produce molecular beams at velocities compared to the speed of sound which is too fast for performing high-resolution molecular spectroscopy. That is why we slow them down in a traveling-wave Stark decelerator by means of time-dependent electric fields that provide moving electric traps [9]. A decrease in velocity corresponds to a linear increase in coherent measurement time in e.g. a slow beam spectroscopic experiment. One important parameter is the number of molecules being probed in the ultimate experiment. Therefore, it is essential to maximize the loading efficiency in moving electric traps from the source and to minimize possible losses during the deceleration process.

In the remainder of this introductory chapter, we cover in more detail the basic ideas of the Standard Model; aforementioned tests of this model using different experimental methods; basic ideas of manipulating heavy molecules including producing them in a supersonic source; the interaction of molecules with an optical field; the basics of the Stark deceleration; and the strategies for loading molecules into static traps. The outline of the dissertation is given at the end of this chapter.

1.1. The Standard Model and its problems

The Standard Model (SM) has been developed as an attempt to unite the strong, electromagnetic and weak forces in one theoretical framework. Its modern form includes all the elementary particles of the visible matter and the force carriers between them. The SM is successful in describing properties of many different processes that can occur at a microscopic level between elementary particles. So far, no significant deviation from the SM has been found in high-energy experiments. Recently, some experiments reported slight differences (below 5-sigma confidence level) between the SM predictions of certain parameters [10, 11], giving rise to lively discussions.

Despite the success of the SM, it is not a perfect theory and has some drawbacks both in the theoretical and experimental sector. The problems in the theoretical part are due to a lack of comprehensibility of some SM features, such

[1] We refer here to the electric dipole moment of a molecule that is an eigenstate of the Hamiltonian [8].

as the mass hierarchy of elementary particles, the origin of spontaneous symmetry breaking in the Higgs mechanism, or the number of free parameters. Other shortcomings have to do with the fact that some of the fundamental properties of nature do not have an adequate explanation within the SM. One of the largest difficulties with the SM is obviously the absence of gravity. The situation is even more severe because there is no common theoretical framework that combines the SM and the very successful theory of gravity until now, General Relativity. The next important issue is to explain the dominance of matter over anti-matter in nature, which does not reflect the assumption of a production of equal amounts of particles and antiparticles at the origin of the Universe. Experiments with neutrinos demonstrate evidence that they are not massless particles, which has required some refinement of the SM. Finally, cosmological observations strongly indicate that particles of the SM are responsible for only about 5 percent of the mass-energy in the observable Universe. Another substantial part of the Universe consists of dark matter that seems to interact only gravitationally, and dark energy which is an acceptable explanation of an observed accelerating expansion of the Universe. All aforementioned open questions concerning the SM suggest that there is "New Physics" beyond that covered by the current model. Recently, new proposals for models appear in the literature which have the SM as a basis. It requires time and many experimental efforts to confirm or rule out these new theories. Currently, many projects worldwide aim to search for new hints of some BSM physics.

1.2. Fundamental physics tests with cold molecules

The field of cold molecules is a rapidly developing branch of modern physics with diverse potential applications. The examples are cold chemistry, quantum computing, and few- and many-body physics. A recent overview of these utilizations can be found elsewhere [12]. Here we focus on one particular application of cold molecules, namely high-precision tests of fundamental physics, including prominent examples of discrete symmetry violations and spaciotemporal variation of fundamental constants.

1.2.1. Parity nonconservation

The $\mathcal{CPT}$-theorem states that all fundamental physical laws are symmetric under the product of charge conjugation (particle-antiparticle replacement, or $\mathcal{C}$-symmetry), parity transformation (space reflection, or $\mathcal{P}$-symmetry) and time

reversal (time inversion, or $\mathcal{T}$-symmetry) [13, 14]. To be more specific, this theorem always holds in Lorentz-invariant quantum field theories, such as the SM. $\mathcal{CPT}$ conservation has been tested in many experiments to an extraordinary level of precision [15]. So far, it was found to be a fundamental property of nature. However, individual symmetries ($\mathcal{C}$-, $\mathcal{P}$- and $\mathcal{T}$-) do not have to be exact in order to respect the $\mathcal{CPT}$-theorem.

Parity is a very fundamental property of a quantum mechanical system, as it determines a sign of a complex wavefunction under spatial inversion, or mirror reflection around a reference point. The eigenvalues of the parity operator $\hat{P}$ acting on a wavefunction are $+1$ or -1, which are correspondingly referred to as parity-even or parity-odd transformations. The latter transformations break the symmetry of the quantum system. In 1956, Lee and Yang proposed a parity violating mechanism due to weak interactions between electrons and nuclei [16], which was followed by the discovery of parity nonconservation (PNC) in the β-decay of ^{60}Co atoms [17] and in meson decays [18]. Later, Zel'dovich pointed out a possibility for the displacement of electron levels of opposite parity in a free atom [19]. However, this type of PNC was beyond the experimental reach in the hydrogen atom at that time. It took more than a decade before Bouchiat and Bouchiat realized that the amplitude of parity violation is significantly enhanced in heavy atoms [20]. The enhancement factor depends strongly on the nuclear charge Z, and scales faster than Z^3. For example, if one considers atomic lead, the PNC signal is $\sim 5\times10^6$ times larger compared to hydrogen. At this size, atomic parity violation is in principle detectable. This theoretical finding triggered experimental searches for atomic parity violation in different systems. Over the following decades, up until now, different experiments reported PNC effects in many heavy atoms: bismuth (Bi, Z=83) [21], thallium (Tl, Z=81) [22], lead (Pb, Z=82) [23], cesium (Cs, Z=55) [24], and ytterbium (Yb, Z=70) [25, 26]. All of these results lie within the predictions of the SM. However, they enable the searching for BSM physics. It is worth mentioning that atomic PNC effects are nuclear-spin independent as they are caused primarily by the weak charge of the nucleus, i.e. essentially the number of neutrons. Molecules possess a much more complicated internal structure compared to atoms. Hence, experiments on them can shine a light on the same and similar phenomena but from different points of view.

Electroweak interactions inside molecules are manifested by nuclear-spin dependent parity violation (NSD-PV) that has three different sources of contributions [27]. The Feynman diagrams for these processes are shown in Fig. 1.1(a-c). The first contribution originates from the electroweak neutral coupling between electrons and nucleons inside a nucleus [28]. The second one arises from the nuclear anapole moment [29]. It is a parity-odd magnetic moment associated

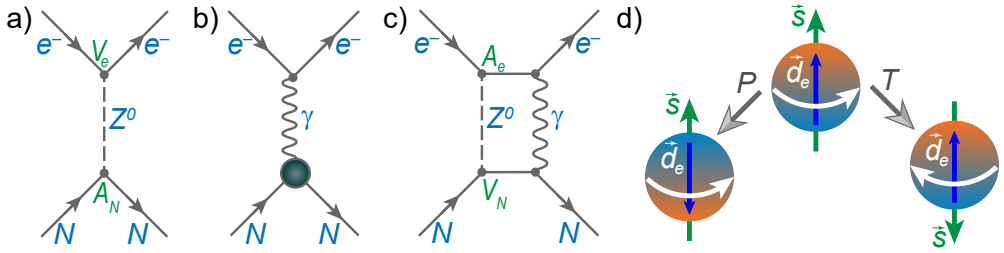

Figure 1.1 | Examples of violations of discrete symmetries that can be probed in molecules. Nuclear-spin dependent parity violation (a) due to Z^0-boson exchange between electron vector and nucleon axial-vector currents, (b) electromagnetic coupling between electrons and nuclear anapole moment, shown as a ball, (c) combined effect of the hyperfine interaction and spin-independent Z^0-exchange interaction from nucleon vector currents. (d) $\mathcal{P}$-, and $\mathcal{T}$-reversal symmetry breaking due to an electric dipole moment of the electron.

with electroweak nucleon-nucleon interactions mediated by meson exchange. The anapole moment can couple electromagnetically to the electrons penetrating a nucleus and thus leads to hadronic parity violation. And finally, the third NSD-PV effect is due to the combined result of the electronic hyperfine interaction and spin-independent Z-boson exchange [30]. Experimentally, PNC in molecules can be observed by measuring the coupling between energy levels of opposite parity that can be tuned to almost degeneracy in external electric or magnetic fields.

Recently, the most sensitive technique to measure NSD-PV in molecules was demonstrated by the group of DeMille [31]. They used a Stark-interference method for a beam of ^{138}BaF. The projected uncertainty of this experiment already surpasses that of the best atomic measurement of NSD-PV in ^{174}Yb. Similar experiments with heavy diatomic molecules open a pathway to measure purely hadronic PNC signals.

1.2.2. Electron electric dipole moment

Another unanswered question in modern physics originates from an obvious disagreement between the SM of particle physics and cosmology. According to the generally assumed Big Bang theory, that describes evolution of our Universe from the first known moments of its existence until the present time, there was an equal amount of matter and antimatter produced in the very beginning. However, the Universe now consists predominantly of matter. This holds true everywhere in the observable cosmos [32]. The subtle asymmetry in the production of matter occurred in the aftermath of the Big Bang. This problem is now known as the baryon asymmetry. In an attempt to solve this problem, Sakharov introduced a

set of conditions that have to be satisfied in order to give rise to the observable dominance of matter over antimatter [33]. One of the necessary conditions is violation of the combined $\mathcal{CP}$-symmetry, which implies the possibility for different intrinsic properties of particles and antiparticles. Moreover, it also demands violation of the $\mathcal{T}$-reversal symmetry provided $\mathcal{CPT}$ holds. According to the SM, there are few sources of $\mathcal{CP}$-symmetry breaking [34]. However, an amount of $\mathcal{CP}$-violation within the SM is not enough to account for the observed matter-antimatter asymmetry. Inevitably, only BSM models can adequately explain missing contributions to $\mathcal{CP}$-violation. Another possibility for the observed baryon asymmetry implies violation of $\mathcal{CPT}$ [35]. Interestingly, the asymmetry between matter and antimatter can also be connected to the asymmetry of the charge distribution inside the electron, which is the fundamental particle-carrier of elementary charge [36].

In a seminal work by Purcell and Ramsey [37], it was proposed that elementary particles can have a permanent electric dipole moment (EDM) along their spin. Within the SM framework, an EDM can be caused by interaction of the particle with virtual particle pairs from vacuum fluctuations. Any non-zero value of an EDM of an elementary particle would necessarily demand breaking of both parity and time-reversal symmetries. This violation is visualized in Fig. 1.1(d) for the electron. The electron electric dipole moment (eEDM) corresponds to an asymmetric charge distribution inside the electron, which is depicted by a color gradient and by a vector $\vec{d}_e$. The direction of this vector is along spin $\vec{s}$ of the electron[2]. Parity transformation changes the direction of the eEDM and the spin stays unaltered, while time inversion transforms these vectors the other way around. In both cases, there is symmetry breaking.

The SM predicts a value of the eEDM of the order 10^{-38} e·cm [39], which is far below current experimental sensitivities. Different BSM theories predict much larger values of the eEDM due to the interaction of the electron with some hypothetical heavy particles with masses in the TeV range [40]. For instance, the supersymmetric extension of the SM (SUSY) can give rise to an eEDM of up to $\sim 10^{-30}$ e·cm by introducing selectrons and photinos. This range of sensitivities can already be potentially reached in certain cases in laboratory experiments, when a set of conditions is fulfilled as will be described in the next paragraph.

Molecules offer some benefits in the search for a permanent eEDM compared to atoms due to their specific energy level structure. Thus, molecules with one heavy nucleus and one unpaired electron can possess a very strong internal electric field, sometimes of the order 100 GV/cm, that is much larger than laboratory-produced electric fields [57]. In recent years, a number of experiments

[2] From the Wigner-Eckart theorem, an electric dipole moment of an elementary particle has to be collinear with its spin [38].

have been launched to search for an eEDM in different species. So far, all of them are consistent with a null result, thereby setting new upper limits on the value of the eEDM. In 2011, the group of Hinds used a supersonic beam of YbF molecules to provide a constraint of $|d_e|<10.5\times10^{-28}$ e·cm [45]. Later, two generations of an experiment by the ACME collaboration have improved this result by almost two orders of magnitude. It yielded the most stringent upper limit on the eEDM to date, $|d_e|<1.1\times10^{-29}$ e·cm [58, 59]. They utilized a buffer-gas cooled beam of ThO molecules in their low-lying metastable states which have a very large internal electric field. There is also a possibility to use not only neutral molecules in the search for an eEDM, but also molecular ions. This has been successfully demonstrated by the group of Cornell at JILA. They have performed a high-precision experiment on HfF^+ ions captured in a radio-frequency trap. The recently-concluded measurement has placed a limit on the eEDM of $|d_e|<1.3\times10^{-28}$ e·cm [60], which is slightly higher than the result of the first experiment by the ACME collaboration. Finally, a project to experimentally search for an eEDM in BaF molecules has started in a collaboration between the University of Groningen and the Vrije Universiteit Amsterdam. The idea is to use a favorable enhancement factor of internal electric field inside the molecule and deceleration techniques to reduce the statistical uncertainty of the measurement.

Table 1.1 | Theoretically proposed molecules as candidates to search for an eEDM. Highlighted molecules either have been probed experimentally or are in preparation for a precision measurement.

Molecule	Electronic state	Effective electric field $\mathcal{E}_{\text{eff}}$ (GV/cm)	References
PbO	Metastable $^3\Sigma_1$	23-25	[41–43]
YbF	$X^2\Sigma_{1/2}$	14.5-43	[42, 44–46]
ThO	Metastable $^3\Delta_1$	84-104	[42, 47]
BaF	$X^2\Sigma_{1/2}$	4.5-8.5	[42, 48–50]
PbF	$X^2\Pi_{1/2}$	36.6-40	[44, 51, 52]
HgF	$X^2\Sigma_{1/2}$	68-115	[42, 44, 50, 53]
HgCl	$X^2\Sigma_{1/2}$	113	[53]
HgBr	$X^2\Sigma_{1/2}$	109	[53]
HgI	$X^2\Sigma_{1/2}$	109	[53]
WC	$X^3\Delta_1$	54	[54]
HfF^+	Metastable $^3\Delta_1$	18-30	[42, 44, 55]
ThF^+	$X^3\Delta_1$	37.3-90	[42, 56]
HfH^+	Metastable $^3\Delta_1$	17	[44]
PtH^+	Metastable $^3\Delta_1$	73	[44]

The projected sensitivity of this experiment is $5{\times}10^{-30}$ e·cm which is below the current upper limit [61]. In the near future, new tests of the $\mathcal{CP}$-symmetry will lead to more stringent bounds on the possible SM extensions or to the ground breaking discovery of the non-round shape of the electron.

Here we give a brief overview of the theoretical investigations regarding promising candidates for high-precision measurements to search for an eEDM. The aforementioned effective electric field ($\mathcal{E}_{\text{eff}}$) is an important figure of merit of any experiment, since it determines the statistical uncertainty of the final result. This parameter cannot be measured directly and therefore has to be estimated using various molecular structure calculations. Table 1.1 summarizes molecular species, both neutral and ionic, that have been identified as possible candidates to search for an eEDM. The relevant electronic states and calculated effective electric fields are also listed. As one can see from the table, a value of $\mathcal{E}_{\text{eff}}$ depends on the chosen theoretical calculation approach. Therefore, new methodologies have been developed to address the precision of these calculations [62].

1.2.3. Variation of fundamental constants

Fundamental constants are at the heart of any physics law, since they determine magnitudes of physical processes. They are generally defined as parameters of a theory that cannot be explained by the theory itself and can only be measured. In the approach of Ref. [63], the SM has 19 dimensionless parameters that are supplemented by the speed of light in a vacuum c, the Planck constant $\hbar$, and the gravitational constant G: together 22 independent fundamental constants. Other theories have other sets of constants, but in either case their values can be determined only through experiments. An important question is whether these constants remain unchanged in time and in space. In other words, do physical processes occur identically in different moments of time, or at different locations in the Universe. Some theories speculate about the possibility for temporal and spatial variation of dimensionless fundamental constants [64]. Examples are the fine-structure constant $\alpha{=}\frac{1}{4\pi\epsilon_0}\frac{e^2}{\hbar c}$, characterizing the strength of the electromagnetic interaction, and the proton-to-electron mass ratio $\mu{=}m_p/m_e$, that is related to the relative strength of the strong and electroweak interactions. Two major experimental directions in the search for possible variations of fundamental constants (VFC) are observational studies of astronomical light sources and laboratory high-precision measurements [65].

Molecules in this aspect offer a promising laboratory testing ground, since their energy level structure, or simply spectra, are extremely sensitive to the change of both α and μ. This enhancement is caused by an accidental degeneracy of energy levels in some species. By comparing absorption data from astronomical

observations at high redshift (and effectively at earlier moments in time) and the same data at zero redshift in the laboratory, the constraint on a variation of μ can be set. Interestingly, the best limit on the temporal variation of μ at high redshifts (z=2.0−4.2) comes from the most abundant chemical constituent of the matter, molecular hydrogen (H_2), and is equal $|\Delta\mu/\mu|<5\times10^{-6}$ [66]. The strictest constraints for lower redshifts (z=0.89) are $|\Delta\mu/\mu|<1.5\times10^{-7}$ and have been obtained from the radioastronomical studies of methanol (CH_3OH) [67–69]. Many other molecular candidates for possible VFC have been identified [27], and so far all such experiments yielded a null-effect. This means that all processes happening on Earth, and in any remote area of the cosmos, now and billions years ago can be described by the same physics laws. New results from improved astronomical instrumentation and increased laboratory precision will enable further tests of the immutability of fundamental constants.

1.3. Experimental methods

All experiments with molecules dedicated for various tests of fundamental physics demand a challenging preparation of molecular samples. Here we give a short overview of different relevant techniques that have been recently developed worldwide and particularly in our group, aiming for various experiments with cold molecules.

1.3.1. Production of cold molecules

To characterize the kinetic energy of a molecular ensemble, it is useful to introduce the phase-space density ρ of the system, which is defined as the number of quantum states per element of volume in the phase space. This value depends on the particular way of producing samples of molecules and typically is in the order of $\sim10^{-15}$, while unity corresponds to the state of quantum degeneracy. Two principally different methods to produce low-temperature samples of diatomic molecules in their low-lying electronic and rovibronic states exist: merging two cold atoms into one compound and direct cooling of molecules from high-temperature conditions. The following paragraphs briefly describe basic concepts of these experimental methods, as well as their advantages and disadvantages.

Association from cold atoms

In recent decades, enormous progress in laser cooling techniques has led to ground-breaking results in the production of low-temperature atomic samples, including

the creation of the first Bose-Einstein condensate of alkali atoms. Generally, there are two alternative approaches to combine two pre-cooled atoms forming a diatomic molecule in a sub-mK regime: magneto- and photoassociation.

The first method is creation of weakly bound molecules via magnetoassociation near Feshbach resonances, when the energy of a bound state is equal to the kinetic energy of a pair of atoms [70]. In this way, the first molecular Bose-Einstein condensate (BEC) was obtained in atomic Fermi gases of ^{40}K [71] and ^{6}Li [72]. The bosonic dimers were characterized by a prominent bimodal density distribution during a sweep across a Feshbach resonance, however they were highly vibrationally excited and extremely weakly bound. Similar methods of ramping an external magnetic field across resonance have been used to produce a number of cold heteronuclear Feshbach molecules, such as ^{6}Li^{40}K, ^{40}K^{87}Rb and ^{85}Rb^{87}Rb [73]. In order to selectively transfer Feshbach molecules to more deeply bound quantum states, the stimulated Raman adiabatic passage (STIRAP) technique has been efficiently implemented in a range of experiments for both homo- and heteronuclear cases. In Ref. [74], two-photon Raman transfer has been applied to $^{133}Cs_2$ Feshbach molecules. The heteronuclear fermionic ^{40}K^{87}Rb molecules have been successfully transferred to the ground state using the same method [75]. However, they are highly unstable since the exchange chemical reaction is exothermic. In both cases, the transfer efficiency was higher than 80% due to favorable details of the energy level structure. Ultracold bosonic ^{87}Rb^{133}Cs molecules are more stable compared to KRb and have been routinely produced in the rovibrational ground state using STIRAP transfer [76].

The second experimental method to produce ultracold molecules from ultracold atoms is photoassociation. On the fundamental level this technique can be described as a process when two atoms absorb a photon of a certain wavelength to form a molecule in an electronically excited state [77]. This is an optical analogue of Feshbach resonances, as the kinetic energy of the atoms plus the energy of the photon are equal to the energy of the bound molecular state. So far, many species have been produced in the ultracold regime via the photoassociation process. This range includes homonuclear molecules, for example Na_2 [78] or Sr_2 [79], as well as heteronuclear ones composed mostly of alkali atoms, such as RbCs [80], LiCs [81], KRb [82], NaLi [83]. There is also an increasing interest in producing alkali-alkaline earth molecules and alkali-Yb compounds due to their susceptibility to both electric and magnetic fields [84].

Joining two cold atoms has become a solid playground for ultracold molecular production and yields the highest phase-space densities compared to other techniques. However, this method has a natural constraint, since a molecular candidate must be composed only of species that can be efficiently laser-cooled. Proper laser cooling schemes have hitherto been identified or successfully imple-

mented only for a handful of neutral atoms: stable alkalis, some alkaline-earth metals, and some other species such as ytterbium, erbium and dysprosium. Molecules that consist of non-laser-coolable constituents cannot be produced with this method.

Production of supersonic molecular beams

Direct cooling methods imply that molecules are produced in a relatively high energetic state, and then this energy is dissipated via versatile cooling techniques. At the very beginning of such experiments with molecules, there is a creation of a molecular beam, which is a collimated jet of molecules with well-defined velocity and position spread. Supersonic beams have become the most common way of producing high-intensity beams of internally cold molecules with relatively high forward velocity. These beams can be used for physics experiments immediately or they can be manipulated by different means in preparation of slower or colder samples.

The phenomenology of supersonic beams can be qualitatively described by gas dynamics equations [85]. Simply, if a gas at a certain temperature and pressure is kept in a reservoir and then released into vacuum through a nozzle, a supersonic jet can emerge. The condition for this to happen depends on the characteristic dimensions: the diameter of the orifice in the reservoir D and the mean free path of the gas molecules λ. In the limit $D \gg \lambda$, a supersonic regime is attained, whilst in the opposite case, no collisions between particles occur, which corresponds to an effusive regime. In the first case, part of the thermal energy of the initial gas is transferred to the kinetic energy of the mass flow. Inelastic collisions between the molecules during this isentropic expansion cool various degrees of freedom. As a result, a gas with an initially broad Maxwell-Boltzmann velocity distribution and zero net flow becomes a beam traveling along the axis of the nozzle. The beam has a relatively large forward speed with narrow velocity distribution. The shape of this distribution depends upon the pressure of stagnating gas [86], which can typically vary in the range 1-10 bar. As gas expands into the vacuum chamber, its pressure reduces and at some point collisions between the molecules no longer occur. Then the beam reaches its terminal velocity, which is in the ideal gas law framework a function of molecular mass, specific heat ratio, and temperature of the gas in the reservoir. Obviously, reducing the temperature of the reservoir leads to a lower mean velocity of the beam.

In the simplest case, molecules of interest at high pressure are kept inside a reservoir and are rapidly expanded into a vacuum chamber through a pulsed valve. The design of this valve is based on various actuating mechanisms. It provides for keeping many orders of magnitude pressure difference between the chamber and the reservoir and for fast opening of an orifice between them. For

instance, a current through a coil can generate a strong pulsed magnetic field that can impart momentum to a magnetic alloy plunger [87]. Stable molecules, for example CO, NH_3 or NO_2, can be kept in a gas bottle that is connected to the back of the valve, and generation of a supersonic beam is achievable. However, sometimes the molecules of interest are free radicals that do not exist in gaseous phase since they would stick to the walls of a vacuum chamber. In this case, they have to be produced by other means and seeded into a supersonically expanding gas, referred to as carrier. Usually, in such an environment noble gases serve for the purpose of elastic collisions, as they do not react chemically with the molecules. The terminal velocity of a seeded supersonic molecular jet depends on the type of noble gas used for an expansion due to the mass dependence of a carrier. Theory predicts terminal velocities of 1770, 787, 559, 386 and 308 m/s for He, Ne, Ar, Kr and Xe, respectively, when a carrier expands from a reservoir at room temperature [88]. In practice, velocities close to the predicted values are achieved for light noble gases, and they slightly differ for heavy gases that are more subject to condensation and clustering processes.

The heavy molecules used in our research, namely SrF and BaF, are free radicals and have to be seeded into a monoatomic carrier gas in order to create a supersonic beam. For that we use a strontium (or barium) metal target that is located immediately downstream of the valve nozzle. Ablation of this target with the light from a pulsed laser creates a plume of Sr (Ba) atoms. Heavy carrier gas, typically Ar or Xe, with an admixture of SF_6 gas is kept behind a pulsed valve that makes short ($\sim$100 μs) jets. The chemical reaction between Sr (Ba) and SF_6 takes place, forming SrF (BaF) radicals that are entrained into the carrier gas pulse. A conical shape skimmer is located few cm downstream the beam propagation to select only the densest part of the molecular beam. At room temperature of the valve body, forward velocities of molecular beams of 550 and 345 m/s with $\sim$10% spread for Ar and Xe, respectively, are routinely achieved.

Cryogenic buffer-gas cooling sources

Compared to supersonic expansion, the buffer-gas cooling has a principally different mechanism for creating molecules in the sub-K regime. This is achieved by mixing two gases in a cold cell held at cryogenic temperature [89]. These two gases are the molecules of interest which are introduced at high temperature and cold inert buffer gas atoms cooled to 2-25 K. The buffer gas can leave the cell through an aperture in one of the walls. Hot molecules when entering the cell can be cooled by collisions with the buffer gas, thermalizing translational and internal degrees of freedom. Then the molecules form a beam by being extracted from the cell by the outward buffer gas flow.

Cryogenic buffer-gas cooling sources have proven to provide intense beams of slow molecules with forward velocities in a range 50-200 m/s, however the spread of such beams is typically larger than that of supersonic beams. A wide range of species, both light and heavy, have been cooled in buffer-gas beams, including a number of diatomic molecules that are of interest for experimental tests of fundamental physics. In most cases, the intensity of the beams is the largest among other production methods. As a quantitative example, the reported values of brightness (number of molecules per quantum state per second per unit solid angle) for SrF, ThO and CaH are 1.8×10^{12} [90], 3×10^{13} [91], and 5×10^{9} molecules/s/sr [92] in a single quantum state, respectively.

In our group, there is an ongoing project to build a cryogenic buffer-gas source of BaF molecules seeded into a cell at a temperature of 20 K filled with Ne as a buffer gas. The combination of the cryogenic molecular source and the Stark deceleration method will be a starting point for a slow-beam experiment to search for an electron EDM.

Laser cooling of diatomic and polyatomic molecules

As mentioned above, the laser cooling technique for atoms has become a workhorse in a multitude of applications. It is based on the scattering of photons off a single atom due to momentum transfer between them. Molecules, due to their complex energetic structure, have extra complications and hence appropriate candidates and cooling schemes are more difficult to identify.

The important ingredients for an efficient realization of the laser cooling process in molecules are: a favorable rotational structure with a closed optical cycle; the diagonality of a Franck-Condon matrix; the lifetime of excited states; and the availability of lasers at cooling transition wavelengths. The first one has to be met to eliminate optical pumping into rotational states which are not addressed by the laser. The second condition determines the branching ratio of different vibrational states of a molecule where it can decay to. This is the key point of the whole process as it requires many scattering events. The excited state lifetime has to be short enough such that many events can occur during a unit of time. The last ingredient arises from a practical point of view.

Looking for candidate molecules with the required properties is the topic of many theoretical studies. The first diatomic molecule proposed and shown to be laser-coolable is SrF [93]. It has highly-diagonal Franck-Condon factors, a short radiative lifetime of the excited state ($\sim$20 ns), and a wavelength of the principal cooling transition of 663.3 nm. Later, several other diatomic species have been laser-cooled, in some cases reaching fundamental limits of this process. CaF molecules were first slowed down by laser light and then cooled using various techniques to temperatures as low as 50 μK [94]. Recently, one-dimensional

laser cooling has been successfully applied to a triatomic molecule, SrOH [95]. These seminal experiments open a pathway towards creating a variety of di- and polyatomic molecules in the sub-mK regime via interaction with light.

1.3.2. Precision control over molecules

Manipulation of neutral polar molecules through external fields has been developed extensively in the last few decades [96]. This method includes deflection, focusing, guiding, and deceleration of molecular beams with the aid of inhomogeneous and time-dependent electric or magnetic fields. When a molecule in a certain quantum state is placed inside an external electric field $\boldsymbol{\mathcal{E}}$ or a magnetic field $\boldsymbol{B}$, then the energy of that state is shifted by $-\boldsymbol{d}\cdot\boldsymbol{\mathcal{E}}$ or $-\boldsymbol{\mu}\cdot\boldsymbol{B}$, where $\boldsymbol{d}$ and $\boldsymbol{\mu}$ are electric dipole moment and magnetic dipole moment, respectively. This splitting of spectral lines in an $\mathcal{E}$-field is known as the Stark effect [97]. Zeeman was the first to observe an effect related to the splitting of the energy levels in a B-field [98]. This splitting is known as the Zeeman effect. A gradient of either of the fields in space would exert a force on the effective electric or magnetic dipole moment. Therefore, there are two types of devices for precision control over molecular beams, so-called Stark and Zeeman decelerators, depending on the applied external field.

Stark deceleration

The idea of manipulating molecular beams by means of laboratory electric fields is known as long as molecular beam techniques themselves. However, in practice, it was quite difficult to find a geometry and electronics that is feasible for controlling the longitudinal velocity of a molecular beam. In 1999, the first Stark decelerator developed in the group of Meijer led to deceleration of a beam of neutral metastable CO molecules [99]. This type of decelerator, later referred to as a traditional Stark decelerator (TSD), was formed from an array of electric field stages separated by a certain distance, while each stage consisted of many pairs of parallel electrodes. High voltage was applied to the stages and it was rapidly switched between two configurations (hence this device is sometimes called a switching type decelerator). The geometry and proper switching sequence enabled the creation of an inhomogeneous time-varying $\mathcal{E}$-field with well defined minima. Molecules in quantum states whose energy increase with increasing electric field strength (later called low-field seeking states, or lfs) can gain potential energy while being placed inside the TSD and correspondingly lose kinetic energy. Molecules in other states, that lose energy with increasing electric field strength, are called high-field seeking (or hfs) and are repelled from the decelerator axis. The repetition of switching cycles many times is a way of gradually removing kinetic energy and slowing down lfs molecules that remain

trapped by $\mathcal{E}$-field minima.

Lately, a number of deceleration and collision experiments have been performed using TSD for a range of species. Moreover, the development of the TSD technique has led to the first trapping of deuterated ammonia molecules in a laboratory frame of reference [100]. Nevertheless, the performance of a TSD drops significantly when the velocity of a pulsed beam becomes small ($\sim$50 m/s), which hinders the loading of molecules into static traps and consequent high-precision spectroscopy. This is due to poor transverse confinement of moving electric traps in a velocity range below a certain velocity, which depends on the details of the energy structure of a decelerated molecule. An increased transverse velocity spread leads to a large position spread, resulting in a trapping loss process [101]. To address the problem of a limited number of molecules at low velocities, another configuration of electrodes has been designed, where genuine three-dimensional moving potential wells for lfs molecules can be created [9]. It is a traveling-wave Stark decelerator (TWSD) consisting of an array of ring-shaped electrodes. When alternating voltages are applied to the electrodes, the electric field can travel along the decelerator axis. The design of a TWSD allows for deceleration of heavy diatomic molecules and for bringing them to rest in the laboratory frame. This opens a pathway towards fundamental physics tests described above. In our laboratory, a 4.5 meter long TWSD has been built and characterized. Its performance at extreme conditions, such as those required for the strongest deceleration, is a part of the current dissertation. The details of the TWSD design and its principle of operation are given in Chapter 3.

Zeeman deceleration

The second category of devices for controlling beams of paramagnetic species using magnetic fields is a Zeeman decelerator. The first demonstration of this technique using pulsed inhomogeneous magnetic fields was performed for hydrogen atoms [102]. So far, there are two experimental realizations of Zeeman-effect-based deceleration of molecular beams. In Ref. [103], a simultaneous slowing down of metastable argon and molecular oxygen was demonstrated in moving magnetic traps. The traps were formed by constructing an array of spatially overlapping quadrupole traps that were activated by a temporally overlapping pulse sequence. There are in total 480 traps that span over a length of 2.4 m. A similar approach of a Zeeman decelerator design was developed in Oxford [104], where a series of 12 solenoid coils and an evolutionary algorithm sequence of current pulses provides for optimized deceleration of light paramagnetic species. The proper sequence has led to an increased number of decelerated hydrogen atoms and to lower final velocities. The second type of Zeeman decelerator is composed of an array of alternating hexapoles and solenoids [105]. In a proof-of-

principle experiment with metastable helium atoms, it was shown that such a device can be used for molecular scattering studies.

1.3.3. Loading molecules into static traps

In all high-precision atomic physics experiments, it is required to increase the coherent interaction time. That is the time for which a particle coherently interacts with external fields. In the simplest case of a spectroscopic experiment, a molecule in question is exposed to laser light with a certain wavelength. Compared to a transient type of measurement, where a laser beam crosses a molecular beam for a short time, trapped molecules provide for much longer interaction times. This section gives a short overview of the most widespread trap designs for cold molecules that have been demonstrated in the last two decades.

Electric trap

The first loading of molecules into an electrostatic trap occurred soon after the first demonstration of the Stark deceleration method [100]. The authors used a 63-stage TSD to slow down a supersonic beam of ND_3 in the lfs upper inversion level of the electronic ground state from 260 m/s to 13 m/s. Molecules were then adiabatically transferred into a quadrupole electrostatic trap, where they were attracted to the minimum of the electric field at the geometric center of the setup. The loading scheme requires a certain sequence and timing of high-voltage electrodes to prevent losses during the loading process. The reported density of trapped and state-selected ammonia molecules was 10^6 cm^{-3}. The trap lifetime is usually derived from an exponential decay of the number of molecules due to various loss processes. For the first ammonia trapping experiment, it was reported to be (0.24 ± 0.04) s. Later, improved loading strategies and setup geometries resulted in higher particle densities and longer trap storage times [106]. Studying the details of the loading process has led to an enhanced loading efficiency of OH radicals while transferring into a quadrupole trap [101].

Another design of electric trap with an inhomogeneous field is formed from a microstructured array of linear electrodes immersed into two parallel glass plates making a box-like trap [107]. The electrodes are alternately polarized, which acts as a repulsive barrier for lfs molecules. Fluoromethane molecules can be stored in such potential box for almost a minute with a $1/e$ storage time of 12 s, yielding the longest storage time for this type of trap.

It is worthwhile mentioning that absolute ground states of molecules are always hfs, so they are attracted to regions of high electric field strength. According to the Earnshaw theorem, it is not possible to create a local maximum of the electric field in free space. However, with the aid of time-dependent electric

fields, it is possible to confine hfs molecules around a saddle point of the electric field distribution. The idea of a rotating saddle-shape potential has led to the first trapping of ND_3 molecules in their absolute ground state [108].

Magneto-optical trap

With the possibility to laser cool certain polar molecules, it is also feasible to trap them in a magneto-optical trap (MOT), where a combination of magnetic and laser fields is applied. Three orthogonal laser beams that intersect at the center of a molecular cloud together with a magnetic field gradient produce a scattering force pushing molecules towards the trap center. This radiation pressure force relies on resonant transitions between molecular levels in a closed cycle. Unlike most atomic MOTs, a molecular MOT requires an elaborate design and more complex experimental methods. These complications originate from the energy level structure of molecules and the requirement to repeatedly scatter many photons. If one uses a single cooling laser with a fixed polarization, the scattering processes will quickly pump the system into a dark state, not coupled to laser light. Hence, extra repump lasers and fast laser light polarization switching are usually employed to achieve efficient trapping of molecular ensembles in a MOT.

As of now, there were three experimental realizations of three-dimensional molecular MOTs, all with laser coolable alkaline-earth fluorides. The first MOT was demonstrated in 2014 for the first laser-cooled molecule, SrF. Around 300 particles at a temperature of 2.5 mK were kept for 50 ms [109]. Later, substantial improvements were accomplished in the cooling methods and the trapping techniques of molecules, yielding the modified radio-frequency MOT design. In the latest report, authors claim to observe the trapping of 10^4 SrF molecules at a phase-space density of 6×10^{-14} and a temperature as low as 250 μK [110]. The other two molecular MOTs are loaded from laser-slowed buffer-gas-cooled beams of CaF molecules [111, 112]. They differ in their laser-slowing stages and their trapping strategies, resulting in traps having slightly different properties. The CaF MOT from the Doyle's group confines $1.0(3)\times10^5$ molecules at a temperature of 340(20) μK, while the most optimal loading of a MOT by the group of Tarbutt captures up to 2×10^4 molecules at 730 μK. These results are of high importance for precision control of ultra-cold molecules in the sub-mK regime.

Magnetic trap

In order to extend the range of trapped species, loading of paramagnetic molecules into a conservative magnetostatic trap has been developed. Even before significant progress in direct cooling methods, the first magnetic trapping of CaH molecules straight from a cryogenic buffer gas source was reported in Ref. [113]. The two state-of-the-art magnetic traps for molecules include sophisticated pre-cooling

Table 1.2 | An overview of state-of-the-art three-dimensional traps for neutral molecules

Type of the trap	Molecule	Number	Temperature	Lifetime	References
Electrostatic	CH_3F	10^8	120 mK	12.2(2) s	[107]
Magnetostatic	CaF	5×10^3	70(8) μK	1.8(2) s	[115]
Magneto-optical	SrF	10^4	250 μK	30(4) ms	[110]
Optical dipole	KRb	15×10^3	$\sim1\mu$K	16.3(1.5) s	[116]

methods. Recently, an efficient loading of SrF molecules from a molecular MOT into a magnetic quadrupole trap demonstrated a lifetime in excess of 1 s [114]. A similar technique was applied for laser-cooled CaF, when 5×10^3 molecules at a temperature of 70 μK were captured during almost 2 s [115].

Optical dipole trap

Contrary to the scattering laser cooling force, there is another type of optical force, described in detail in Chapter 2. Here we briefly mention that particles with an electric dipole moment can be trapped in the region of high laser light intensity due to a gradient dipole force. This method has been extensively applied for atomic species in order to conservatively capture clouds of atoms at low temperature or to manipulate nanometer-sized polarizable particles. There are many ways to produce a gradient of the light intensity, including a tight focusing of a single Gaussian laser beam, an intersection of two beams, and an optical lattice formed by a standing light wave.

Until recently, all optical trapping experiments with neutral molecules have been performed with species that consisted of two laser-coolable atoms being trapped by an optical dipole trap (ODT). It is a quite straightforward approach since atoms are already attracted towards the high laser intensity regions and weakly-bound molecules can be formed there in the ways described above. Thus, long-lived ground-state KRb molecules can be kept in a 3D lattice for almost 30 s [116]. A lifetime of 8 s has been attained in a similar fashion for homonuclear Cs_2 molecules [117]. In 2018, confinement of laser-coolable species was demonstrated for the first time via the laser cooling of optically trapped CaF molecules loaded from a radio-frequency MOT [118]. The use of advanced atomic laser-cooling techniques improved the production of optically trapped samples. The optimized approach demonstrates trapping of 1.3×10^3 molecules at a temperature of 21(3) μK [119].

Table 1.2 gives a summary of characteristics for various trapping methods in the most advanced trap designs mentioned in the previous paragraphs. The most important parameters, such as the number of trapped molecules in a cloud, the lowest temperature attained during trapping process, and the $1/e$ lifetime of

traps are listed. These experimental results represent important milestones for future explorations of cold molecules.

1.4. Thesis outline

This dissertation is organized as follows. In Chapter 2, the basic theory relevant for experimental observations and processes is introduced. The emphasis is placed on the effect of external fields on polar molecules, particularly heavy species that have been exploited by our group. Chapter 3 describes details of the experimental setup, which was used to perform the research, and demonstrates experimental results obtained with a 4 meter long traveling-wave Stark decelerator. In Chapter 4, the experimental results with a 4.5 meter long apparatus are reported, focusing on the question of a stable performance of the decelerator. Chapter 5 is devoted to three-dimensional trajectory simulations which we have performed in order to validate our models and gain insight into criteria for stable operation. In the concluding chapter, a full summary and an outlook are given.

References

[1] W. N. Cottingham and D. A. Greenwood, *An Introduction to the Standard Model of Particle Physics* (Cambridge Univ. Press, Cambridge, 2007).

[2] S. L. Glashow, *Partial-symmetries of weak interactions,* Nuclear Physics **22**, 579 (1961).

[3] S. Weinberg, *A Model of Leptons,* Phys. Rev. Lett. **19**, 1264 (1967).

[4] A. Salam, *Elementary Particle Physics. Relativistic Groups and Analyticity,* in *Eighth Nobel Symposium* (Almquvist & Wiskell, Stockholm, 1968) p. 367.

[5] A. Boveia and C. Doglioni, *Dark Matter Searches at Colliders,* Annu. Rev. Nucl. Part. Sci. **68**, 429 (2018).

[6] I. Doršner, S. Fajfer, A. Greljo, J. F. Kamenik, and N. Košnik, *Physics of leptoquarks in precision experiments and at particle colliders,* Physics Reports **641**, 1 (2016).

[7] P. Collier, *The technical challenges of the Large Hadron Collider,* Phil. Trans. R. Soc. A **373**, 20140044 (2015).

[8] I. B. Khriplovich and S. K. Lamoreaux, *CP Violation Without Strangeness. Electric Dipole Moments of Particles, Atoms, and Molecules.* (Springer-Verlag Berlin Heidelberg, Heidelberg, 1997).

[9] A. Osterwalder, S. A. Meek, G. Hammer, H. Haak, and G. Meijer, *Deceleration of neutral molecules in macroscopic traveling traps,* Phys. Rev. A **81**, 051401 (2010).

[10] H. N. Brown *et al.* (Muon (g–2) Collaboration), *Precise Measurement of the Positive Muon Anomalous Magnetic Moment,* Phys. Rev. Lett. **86**, 2227 (2001).

[11] G. Ciezarek, M. F. Sevilla, B. Hamilton, R. Kowalewski, T. Kuhr, V. Lüth, and Y. Sato, *A challenge to lepton universality in B-meson decays,* Nature **546**, 227 (2017).

[12] L. D. Carr, D. DeMille, R. V. Krems, and J. Ye, *Cold and ultracold molecules: science, technology and applications,* New J. Phys. **11**, 055049 (2009).

[13] G. Lüders, *On the Equivalence of Invariance under Time Reversal and under Particle-Antiparticle Conjugation for Relativistic Field Theories,* Dan. Mat. Fys. Medd. **28** (1954).

[14] W. Pauli, *Exclusion Principle, Lorentz Group and Reflection of Space-Time and Charge,* in *Niels Bohr and the Development of Physics* (Pergamon Press Ltd., London, 1955) pp. 30–51.

[15] V. A. Kostelecký and N. Russell, *Data tables for Lorentz and CPT violation,* Rev. Mod. Phys. **83**, 11 (2011).

[16] T. D. Lee and C. N. Yang, *Question of Parity Conservation in Weak Interactions,* Phys. Rev. **104**, 254 (1956).

[17] C. S. Wu, E. Ambler, R. W. Hayward, D. D. Hoppes, and R. P. Hudson, *Experimental Test of Parity Conservation in Beta Decay,* Phys. Rev. **105**, 1413 (1957).

[18] R. L. Garwin, L. M. Lederman, and M. Weinrich, *Observations of the Failure of Conservation of Parity and Charge Conjugation in Meson Decays: the Magnetic Moment of the Free Muon,* Phys. Rev. **105**, 1415 (1957).

[19] Y. B. Zel'dovich, *Parity Nonconservation in the First Order in the Weak-Interaction Constant in Electron Scattering and Other Effects,* JETP **9**, 682 (1959).

[20] M. A. Bouchiat and C. Bouchiat, *I. Parity violation induced by weak neutral currents in atomic physics,* J. Phys. France **35**, 899 (1974).

[21] L. M. Barkov and M. S. Zolotorev, *Observation of parity nonconservation in atomic transitions,* JETP Letters **27**, 357 (1978).

[22] R. Conti, P. Bucksbaum, S. Chu, E. Commins, and L. Hunter, *Preliminary Observation of Parity Nonconservation in Atomic Thallium,* Phys. Rev. Lett. **42**, 343 (1979).

[23] T. P. Emmons, J. M. Reeves, and E. N. Fortson, *Parity-Nonconserving Optical Rotation in Atomic Lead,* Phys. Rev. Lett. **51**, 2089 (1983).

[24] C. S. Wood, S. C. Bennett, D. Cho, B. P. Masterson, J. L. Roberts, C. E. Tanner, and C. E. Wieman, *Measurement of Parity Nonconservation and an Anapole Moment in Cesium,* Science **275**, 1759 (1997).

[25] K. Tsigutkin, D. Dounas-Frazer, A. Family, J. E. Stalnaker, V. V. Yashchuk, and D. Budker, *Observation of a Large Atomic Parity Violation Effect in Ytterbium,* Phys. Rev. Lett. **103**, 071601 (2009).

[26] D. Antypas, A. Fabricant, J. E. Stalnaker, K. Tsigutkin, V. V. Flambaum, and D. Budker, *Isotopic variation of parity violation in atomic ytterbium,* Nat. Phys. **15**, 120 (2019).

[27] M. S. Safronova, D. Budker, D. DeMille, D. F. J. Kimball, A. Derevianko, and C. W. Clark, *Search for new physics with atoms and molecules,* Rev. Mod. Phys. **90**, 025008 (2018).

[28] V. V. Flambaum and I. B. Khriplovich, *P-odd nuclear forces – a source of parity violation in atoms,* JETP **52**, 835 (1980).

[29] Y. B. Zel'dovich, *Electromagnetic interaction with parity violation,* JETP **6**, 1184 (1958).

[30] V. V. Flambaum and I. B. Khriplovich, *On the enhancement of parity nonconserving effects in diatomic molecules,* Phys. Lett. A **110**, 121 (1985).

[31] E. Altuntaş, J. Ammon, S. B. Cahn, and D. DeMille, *Demonstration of a Sensitive Method to Measure Nuclear-Spin-Dependent Parity Violation,* Phys. Rev. Lett. **120**, 142501 (2018).

[32] L. Canetti, M. Drewes, and M. Shaposhnikov, *Matter and antimatter in the universe,* New J. Phys. **14**, 095012 (2012).

[33] A. D. Sakharov, *Violation of CP invariance, C asymmetry, and baryon asymmetry of the universe,* Soviet Physics Uspekhi **34**, 392 (1991).

[34] T. Ibrahim and P. Nath, *CP violation from the standard model to strings,* Rev. Mod. Phys. **80**, 577 (2008).

[35] V. A. Kostelecký and R. Potting, *CPT and strings,* Nuclear Physics B **359**, 545 (1991).

[36] E. Cartlidge, *The electron is still round – for now,* Science **358**, 435 (2017).

[37] E. M. Purcell and N. F. Ramsey, *On the Possibility of Electric Dipole Moments for Elementary Particles and Nuclei,* Phys. Rev. **78**, 807 (1950).

[38] V. Natarajan, *Modern Atomic Physics* (CRC Press, 2015).

[39] M. Pospelov and A. Ritz, *Electric dipole moments as probes of new physics,* Annals of Physics **318**, 119 (2005).

[40] J. Engel, M. J. Ramsey-Musolf, and U. van Kolck, *Electric dipole moments of nucleons, nuclei, and atoms: The Standard Model and beyond,* Progress in Particle and Nuclear Physics **71**, 21 (2013).

[41] A. N. Petrov, A. V. Titov, T. A. Isaev, N. S. Mosyagin, and D. DeMille, *Configuration-interaction calculation of hyperfine and P,T–odd constants on* ^{207}PbO *excited states for electron electric-dipole-moment experiments,* Phys. Rev. A **72**, 022505 (2005).

[42] E. R. Meyer and J. L. Bohn, *Prospects for an electron electric-dipole moment search in metastable ThO and* ThF^+*,* Phys. Rev. A **78**, 010502 (2008).

[43] S. Eckel, P. Hamilton, E. Kirilov, H. W. Smith, and D. DeMille, *Search for the electron electric dipole moment using Ω-doublet levels in PbO,* Phys. Rev. A **87**, 052130 (2013).

[44] E. R. Meyer, J. L. Bohn, and M. P. Deskevich, *Candidate molecular ions for an electron electric dipole moment experiment,* Phys. Rev. A **73**, 062108 (2006).

[45] J. J. Hudson, D. M. Kara, I. J. Smallman, B. E. Sauer, M. R. Tarbutt, and E. A. Hinds, *Improved measurement of the shape of the electron,* Nature **473**, 493 (2011).

[46] M. Abe, G. Gopakumar, M. Hada, B. P. Das, H. Tatewaki, and D. Mukherjee, *Application of relativistic coupled-cluster theory to the effective electric field in YbF,* Phys. Rev. A **90**, 022501 (2014).

[47] L. V. Skripnikov, A. N. Petrov, and A. V. Titov, *Communication: Theoretical study of ThO for the electron electric dipole moment search,* J. Chem. Phys. **139**, 221103 (2013).

[48] M. G. Kozlov and L. N. Labzowsky, *Parity violation effects in diatomics,* J. Phys. B: At. Mol. Opt. Phys. **28**, 1933 (1995).

[49] M. Fukuda, K. Soga, M. Senami, and A. Tachibana, *Local spin dynamics with the electron electric dipole moment,* Phys. Rev. A **93**, 012518 (2016).

[50] K. Gaul and R. Berger, *Zeroth order regular approximation approach to electric dipole moment interactions of the electron,* J. Chem. Phys. **147**, 014109 (2017).

[51] L. V. Skripnikov, A. D. Kudashov, A. N. Petrov, and A. V. Titov, *Search for parity- and time-and-parity–violation effects in lead monofluoride (PbF): Ab initio molecular study,* Phys. Rev. A **90**, 064501 (2014).

[52] S. Sasmal, H. Pathak, M. K. Nayak, N. Vaval, and S. Pal, *Calculation of P,T-odd interaction constant of PbF using Z-vector method in the relativistic coupled-cluster framework,* J. Chem. Phys. **143**, 084119 (2015).

[53] V. S. Prasannaa, A. C. Vutha, M. Abe, and B. P. Das, *Mercury Monohalides: Suitability for Electron Electric Dipole Moment Searches,* Phys. Rev. Lett. **114**, 183001 (2015).

[54] J. Lee, E. R. Meyer, R. Paudel, J. L. Bohn, and A. E. Leanhardt, *An electron electric dipole moment search in the $X\ ^3\Delta_1$ ground state of tungsten carbide molecules,* Journal of Modern Optics **56**, 2005 (2009).

[55] T. Fleig and M. K. Nayak, *Electron electric-dipole-moment interaction constant for HfF^+ from relativistic correlated all-electron theory,* Phys. Rev. A **88**, 032514 (2013).

[56] L. V. Skripnikov and A. V. Titov, *Theoretical study of ThF^+ in the search for T,P-violation effects: Effective state of a Th atom in ThF^+ and ThO compounds,* Phys. Rev. A **91**, 042504 (2015).

[57] P. G. H. Sandars, *Measurability of the proton electric dipole moment,* Phys. Rev. Lett. **19**, 1396 (1967).

[58] J. Baron, W. C. Campbell, D. DeMille, J. M. Doyle, G. Gabrielse, Y. V. Gurevich, P. W. Hess, N. R. Hutzler, E. Kirilov, I. Kozyryev, B. R. O'Leary, C. D. Panda, M. F. Parsons, E. S. Petrik, B. Spaun, A. C. Vutha, and A. D. West (The ACME Collaboration), *Order of Magnitude Smaller Limit on the Electric Dipole Moment of the Electron,* Science **343**, 269 (2014).

[59] V. Andreev, D. G. Ang, D. DeMille, J. M. Doyle, G. Gabrielse, J. Haefner, N. R. Hutzler, Z. Lasner, C. Meisenhelder, B. R. O'Leary, C. D. Panda, A. D. West, E. P. West, and X. Wu (The ACME Collaboration), *Improved limit on the electric dipole moment of the electron,* Nature **562**, 355 (2018).

[60] W. B. Cairncross, D. N. Gresh, M. Grau, K. C. Cossel, T. S. Roussy, Y. Ni, Y. Zhou, J. Ye, and E. A. Cornell, *Precision Measurement of the Electron's Electric Dipole Moment Using Trapped Molecular Ions,* Phys. Rev. Lett. **119**, 153001 (2017).

[61] P. Aggarwal, H. L. Bethlem, A. Borschevsky, M. Denis, K. Esajas, P. A. B. Haase, Y. Hao, S. Hoekstra, K. Jungmann, T. B. Meijknecht, M. C. Mooij, R. G. E. Timmermans, W. Ubachs, L. Willmann, and A. Zapara (The NL-eEDM collaboration), *Measuring the electric dipole moment of the electron in BaF,* Eur. Phys. J. D **72**, 197 (2018).

[62] W. Liu, *Handbook of Relativistic Quantum Chemistry* (Springer, Berlin, Germany, 2017).

[63] J.-P. Uzan, *Varying Constants, Gravitation and Cosmology,* Living Rev. Relativity **14**, 2 (2011).

[64] P. A. M. Dirac, *A New Basis for Cosmology,* Proceedings of the Royal Society of London. Series A. Mathematical and Physical Sciences **165**, 199 (1938).

[65] W. Ubachs, *Search for Varying Constants of Nature from Astronomical Observation of Molecules,* Space Sci. Rev. **214**, 3 (2017).

[66] W. Ubachs, J. Bagdonaite, E. J. Salumbides, M. T. Murphy, and L. Kaper, *Search for a drifting proton-electron mass ratio from H_2,* Rev. Mod. Phys. **88**, 021003 (2016).

[67] J. Bagdonaite, P. Jansen, C. Henkel, H. L. Bethlem, K. M. Menten, and W. Ubachs, *A Stringent Limit on a Drifting Proton-to-Electron Mass Ratio from Alcohol in the Early Universe,* Science **339**, 46 (2013).

[68] J. Bagdonaite, M. Daprà, P. Jansen, H. L. Bethlem, W. Ubachs, S. Muller, C. Henkel, and K. M. Menten, *Robust Constraint on a Drifting Proton-to-Electron Mass Ratio at z=0.89 from Methanol Observation at Three Radio Telescopes,* Phys. Rev. Lett. **111**, 231101 (2013).

[69] N. Kanekar, H. L. Bethlem, M. Daprà, W. Ubachs, A. Brunthaler, J. Bagdonaite, K. M. Menten, C. Henkel, and S. Muller, *Constraints on changes in the proton–electron mass ratio using methanol lines,* Mon. Not. R. Astron. Soc. **448**, L104 (2015).

[70] T. Köhler, K. Góral, and P. S. Julienne, *Production of cold molecules via magnetically tunable Feshbach resonances,* Rev. Mod. Phys. **78**, 1311 (2006).

[71] M. Greiner, C. A. Regal, and D. S. Jin, *Emergence of a molecular Bose-Einstein condensate from a Fermi gas,* Nature **426**, 537 (2003).

[72] M. W. Zwierlein, C. A. Stan, C. H. Schunck, S. M. F. Raupach, S. Gupta, Z. Hadzibabic, and W. Ketterle, *Observation of Bose-Einstein Condensation of Molecules,* Phys. Rev. Lett. **91**, 250401 (2003).

[73] C. Chin, R. Grimm, P. Julienne, and E. Tiesinga, *Feshbach resonances in ultracold gases,* Rev. Mod. Phys. **82**, 1225 (2010).

[74] J. G. Danzl, E. Haller, M. Gustavsson, M. J. Mark, R. Hart, N. Bouloufa, O. Dulieu, H. Ritsch, and H.-C. Nägerl, *Quantum Gas of Deeply Bound Ground State Molecules,* Science **321**, 1062 (2008).

[75] S. Ospelkaus, A. Pe'er, K.-K. Ni, J. J. Zirbel, B. Neyenhuis, S. Kotochigova, P. S. Julienne, J. Ye, and D. S. Jin, *Efficient state transfer in an ultracold dense gas of heteronuclear molecules,* Nat. Phys. **4**, 622 (2008).

[76] P. K. Molony, P. D. Gregory, Z. Ji, B. Lu, M. P. Köppinger, C. R. Le Sueur, C. L. Blackley, J. M. Hutson, and S. L. Cornish, *Creation of Ultracold* ^{87}Rb^{133}Cs *Molecules in the Rovibrational Ground State,* Phys. Rev. Lett. **113**, 255301 (2014).

[77] K. M. Jones, E. Tiesinga, P. D. Lett, and P. S. Julienne, *Ultracold photoassociation spectroscopy: Long-range molecules and atomic scattering,* Rev. Mod. Phys. **78**, 483 (2006).

[78] P. D. Lett, P. S. Julienne, and W. D. Phillips, *Photoassociative Spectroscopy of Laser-Cooled Atoms,* Annu. Rev. Phys. Chem. **46**, 423 (1995).

[79] M. McDonald, B. H. McGuyer, F. Apfelbeck, C.-H. Lee, I. Majewska, R. Moszynski, and T. Zelevinsky, *Photodissociation of ultracold diatomic strontium molecules with quantum state control,* Nature **535**, 122 (2016).

[80] N. Bouloufa-Maafa, M. Aymar, O. Dulieu, and C. Gabbanini, *Formation of ultracold RbCs molecules by photoassociation,* Laser Physics **22**, 1502 (2012).

[81] J. Deiglmayr, A. Grochola, M. Repp, K. Mörtlbauer, C. Glück, J. Lange, O. Dulieu, R. Wester, and M. Weidemüller, *Formation of Ultracold Polar Molecules in the Rovibrational Ground State,* Phys. Rev. Lett. **101**, 133004 (2008).

[82] J. Banerjee, D. Rahmlow, R. Carollo, M. Bellos, E. E. Eyler, P. L. Gould, and W. C. Stwalley, *Direct photoassociative formation of ultracold KRb molecules in the lowest vibrational levels of the electronic ground state,* Phys. Rev. A **86**, 053428 (2012).

[83] T. M. Rvachov, H. Son, J. J. Park, P. M. Notz, T. T. Wang, M. W. Zwierlein, W. Ketterle, and A. O. Jamison, *Photoassociation of ultracold NaLi,* Phys. Chem. Chem. Phys. **20**, 4746 (2018).

[84] J. V. Pototschnig, A. W. Hauser, and W. E. Ernst, *Electric dipole moments and chemical bonding of diatomic alkali-alkaline earth molecules,* Phys. Chem. Chem. Phys. **18**, 5964 (2016).

[85] G. Sanna and G. Tomassetti, *Introduction to Molecular Beams Gas Dynamics* (Imperial College Press, 2005).

[86] H. Haberland, U. Buck, and M. Tolle, *Velocity distribution of supersonic nozzle beams,* Rev. Sci. Instrum. **56**, 1712 (1985).

[87] M. R. Adriaens, W. Allison, and B. Feuerbacher, *A pulsed molecular beam source,* J. Phys. E: Sci. Instrum. **14**, 1375 (1981).

[88] M. D. Morse, *Supersonic beam sources,* in *Atomic, Molecular, and Optical Physics: Atoms and Molecules*, Vol. 29 (Academic Press, 1996) pp. 21–47.

[89] N. R. Hutzler, H.-I. Lu, and J. M. Doyle, *The Buffer Gas Beam: An Intense, Cold, and Slow Source for Atoms and Molecules,* Chem. Rev. **112**, 4803 (2012).

[90] J. F. Barry, E. S. Shuman, and D. DeMille, *A bright, slow cryogenic molecular beam source for free radicals,* Phys. Chem. Chem. Phys. **13**, 18936 (2011).

[91] N. R. Hutzler, M. F. Parsons, Y. V. Gurevich, P. W. Hess, E. Petrik, B. Spaun, A. C. Vutha, D. DeMille, G. Gabrielse, and J. M. Doyle, *A cryogenic beam of refractory, chemically reactive molecules with expansion cooling,* Phys. Chem. Chem. Phys. **13**, 18976 (2011).

[92] H.-I. Lu, J. Rasmussen, M. J. Wright, D. Patterson, and J. M. Doyle, *A cold and slow molecular beam,* Phys. Chem. Chem. Phys. **13**, 18986 (2011).

[93] E. S. Shuman, J. F. Barry, and D. DeMille, *Laser cooling of a diatomic molecule,* Nature **467**, 820 (2010).

[94] S. Truppe, H. J. Williams, M. Hambach, L. Caldwell, N. J. Fitch, E. A. Hinds, B. E. Sauer, and M. R. Tarbutt, *Molecules cooled below the Doppler limit,* Nat. Phys. **13**, 1173 (2017).

[95] I. Kozyryev, L. Baum, K. Matsuda, B. L. Augenbraun, L. Anderegg, A. P. Sedlack, and J. M. Doyle, *Sisyphus Laser Cooling of a Polyatomic Molecule,* Phys. Rev. Lett. **118**, 173201 (2017).

[96] S. Y. T. van de Meerakker, H. L. Bethlem, N. Vanhaecke, and G. Meijer, *Manipulation and Control of Molecular Beams,* Chem. Rev. **112**, 4828 (2012).

[97] J. Stark, *Observation of the Separation of Spectral Lines by an Electric Field,* Nature **92**, 401 (1913).

[98] P. Zeeman, *On the influence of magnetism on the nature of the light emitted by a substance,* Philosophical Magazine **43**, 226 (1897).

[99] H. L. Bethlem, G. Berden, and G. Meijer, *Decelerating Neutral Dipolar Molecules,* Phys. Rev. Lett. **83**, 1558 (1999).

[100] H. L. Bethlem, G. Berden, F. M. H. Crompvoets, R. T. Jongma, A. J. A. van Roij, and G. Meijer, *Electrostatic trapping of ammonia molecules,* Nature **406**, 491 (2000).

[101] J. J. Gilijamse, S. Hoekstra, N. Vanhaecke, S. Y. T. van de Meerakker, and G. Meijer, *Loading Stark-decelerated molecules into electrostatic quadrupole traps,* Eur. Phys. J. D **57**, 33 (2010).

[102] N. Vanhaecke, U. Meier, M. Andrist, B. H. Meier, and F. Merkt, *Multistage Zeeman deceleration of hydrogen atoms,* Phys. Rev. A **75**, 031402 (2007).

[103] N. Akerman, M. Karpov, L. David, E. Lavert-Ofir, J. Narevicius, and E. Narevicius, *Simultaneous deceleration of atoms and molecules in a supersonic beam,* New J. Phys. **17**, 065015 (2015).

[104] J. Toscano, A. Tauschinsky, K. Dulitz, C. J. Rennick, B. R. Heazlewood, and T. P. Softley, *Zeeman deceleration beyond periodic phase space stability,* New J. Phys. **19**, 083016 (2017).

[105] T. Cremers, S. Chefdeville, N. Janssen, E. Sweers, S. Koot, P. Claus, and S. Y. T. van de Meerakker, *Multistage Zeeman decelerator for molecular-scattering studies,* Phys. Rev. A **95**, 043415 (2017).

[106] H. L. Bethlem, F. M. H. Crompvoets, R. T. Jongma, S. Y. T. van de Meerakker, and G. Meijer, *Deceleration and trapping of ammonia using time-varying electric fields,* Phys. Rev. A **65**, 053416 (2002).

[107] B. G. U. Englert, M. Mielenz, C. Sommer, J. Bayerl, M. Motsch, P. W. H. Pinkse, G. Rempe, and M. Zeppenfeld, *Storage and Adiabatic Cooling of Polar Molecules in a Microstructured Trap,* Phys. Rev. Lett. **107**, 263003 (2011).

[108] H. L. Bethlem, J. van Veldhoven, M. Schnell, and G. Meijer, *Trapping polar molecules in an ac trap,* Phys. Rev. A **74**, 063403 (2006).

[109] J. F. Barry, D. J. McCarron, E. B. Norrgard, M. H. Steinecker, and D. DeMille, *Magneto-optical trapping of a diatomic molecule,* Nature **512**, 286 (2014).

[110] M. H. Steinecker, D. J. McCarron, Y. Zhu, and D. DeMille, *Improved Radio-Frequency Magneto-Optical Trap of SrF Molecules,* ChemPhysChem **17**, 3664 (2016).

[111] H. J. Williams, S. Truppe, M. Hambach, L. Caldwell, N. J. Fitch, E. A. Hinds, B. E. Sauer, and M. R. Tarbutt, *Characteristics of a magneto-optical trap of molecules,* New J. Phys. **19**, 113035 (2017).

[112] L. Anderegg, B. L. Augenbraun, E. Chae, B. Hemmerling, N. R. Hutzler, A. Ravi, A. Collopy, J. Ye, W. Ketterle, and J. M. Doyle, *Radio Frequency Magneto-Optical Trapping of CaF with High Density,* Phys. Rev. Lett. **119**, 103201 (2017).

[113] J. D. Weinstein, R. deCarvalho, T. Guillet, B. Friedrich, and J. M. Doyle, *Magnetic trapping of calcium monohydride molecules at millikelvin temperatures,* Nature **395**, 148 (1998).

[114] D. J. McCarron, M. H. Steinecker, Y. Zhu, and D. DeMille, *Magnetic Trapping of an Ultracold Gas of Polar Molecules,* Phys. Rev. Lett. **121**, 013202 (2018).

[115] H. J. Williams, L. Caldwell, N. J. Fitch, S. Truppe, J. Rodewald, E. A. Hinds, B. E. Sauer, and M. R. Tarbutt, *Magnetic Trapping and Coherent Control of Laser-Cooled Molecules,* Phys. Rev. Lett. **120**, 163201 (2018).

[116] A. Chotia, B. Neyenhuis, S. A. Moses, B. Yan, J. P. Covey, M. Foss-Feig, A. M. Rey, D. S. Jin, and J. Ye, *Long-Lived Dipolar Molecules and Feshbach Molecules in a 3D Optical Lattice,* Phys. Rev. Lett. **108**, 080405 (2012).

[117] J. G. Danzl, M. J. Mark, E. Haller, M. Gustavsson, R. Hart, J. Aldegunde, J. M. Hutson, and H.-C. Nägerl, *An ultracold high-density sample of rovibronic ground-state molecules in an optical lattice,* Nat. Phys. **6**, 265 (2010).

[118] L. Anderegg, B. L. Augenbraun, Y. Bao, S. Burchesky, L. W. Cheuk, W. Ketterle, and J. M. Doyle, *Laser cooling of optically trapped molecules,* Nat. Phys. **14**, 890 (2018).

[119] L. W. Cheuk, L. Anderegg, B. L. Augenbraun, Y. Bao, S. Burchesky, W. Ketterle, and J. M. Doyle, *Λ-Enhanced Imaging of Molecules in an Optical Trap,* Phys. Rev. Lett. **121**, 083201 (2018).

2

Relevant molecular theory

Molecules as chemically stable structures consisting of two or more atoms have been extensively studied for centuries. Numerous textbooks cover subjects on molecular structure, molecular spectroscopy, intermolecular interactions, electric, magnetic and optical properties of molecules, stereochemistry and so on. Quantum mechanical treatment allows to describe molecular properties with a very high accuracy. The current chapter is devoted to the most relevant theoretical background that is needed for preparation and manipulation of heavy diatomic molecules in our experiment. The first part will describe the basic concepts of the molecular energy level structure, including internal vibrational and rotational degrees of freedom. The change of the molecular spectra in the presence of external electric and magnetic fields is shown in the second section. Finally, the interaction of molecules with light fields and arising effects are presented and discussed in the concluding part. The emphasis is on strontium monofluoride (SrF) molecule, which is a prototypical heavy one-electron radical that is well suited for fundamental physics tests and exploited experimentally in our group the most.

2.1. Energy level structure

In quantum mechanics, a description of any system starts with deriving the Hamiltonian operator. Generally, in the case of molecules, this operator consists of terms for the kinetic energy of all electrons and nuclei, and the potential energy due to Coulomb attraction or repulsion between them (depending on

their charges). For a molecule composed of K atoms and n electrons, the total non-relativistic Hamiltonian is given by [1]:

$$\hat{H} = \hat{T}_{el} + \hat{T}_{nuc} + \hat{V} = -\frac{\hbar^2}{2m}\sum_{i=1}^{n}\nabla_i^2 - \frac{\hbar^2}{2}\sum_{k=1}^{K}\frac{1}{M_k}\nabla_k^2 + V(\boldsymbol{r},\boldsymbol{R}), \tag{2.1}$$

where m and M_k are masses of the electron and nucleus K, respectively, $\boldsymbol{r}$ denotes electronic coordinates, and $\boldsymbol{R}$ denotes nuclear coordinates. The total potential energy has three contributions:

$$\begin{aligned} V(\boldsymbol{r},\boldsymbol{R}) &= V_{nuc,nuc} + V_{nuc,el} + V_{el,el} = \\ &= \frac{e^2}{4\pi\epsilon_0}\left[\sum_{k>k'}\sum_{k=1}^{K}\frac{Z_k Z_{k'}}{R_{k,k'}} - \sum_{k=1}^{K}\sum_{i=1}^{n}\frac{Z_k}{r_{i,k}} + \sum_{i>i'}\sum_{i'=1}^{n}\frac{1}{r_{i,i'}}\right]. \end{aligned} \tag{2.2}$$

The total charge of nucleus K is $Z_k e$, where e is the charge of the electron; and the interparticle distances in denominators are defined as follows: $R_{k,k'}=|\boldsymbol{R}_k-\boldsymbol{R}_{k'}|$, $r_{i,k}=|\boldsymbol{r}_i-\boldsymbol{R}_k|$, and $r_{i,i'}=|\boldsymbol{r}_i-\boldsymbol{r}_{i'}|$. If the Hamiltonian operator is known, the total energy of the system can be found by solving the time-independent Schrödinger equation:

$$\hat{H}\Psi(\boldsymbol{r},\boldsymbol{R}) = E\Psi(\boldsymbol{r},\boldsymbol{R}), \tag{2.3}$$

where $\Psi(\boldsymbol{r},\boldsymbol{R})$ is the total wavefunction of the molecule. In equation (2.2), the electronic and nuclear spins are not taken into account. The corrections due to these effects can be found by adding perturbation terms to the Hamiltonian. However, even in the case of simplest molecules (for example H_2 or H_2^+), the Schrödinger equation cannot be solved analytically. To address this challenge, one can either solve numerically this differential equation or use some valid approximations based on physical models.

Multiple numerical approaches have been introduced so far in order to calculate molecular energies and other (non-)observable properties. The accuracy of such methods strongly depends upon the level of complexity of a molecule, while the available computational resources dictate the choice of the method. The numerical errors that can arise during these procedures are difficult to estimate, and usually each molecule in question requires an individual treatment which is not suited for other ones. The state-of-the-art high-accuracy quantum chemistry calculations for many-electron molecular systems use the relativistic Dirac-Coulomb Hamiltonian and include electron correlations via the coupled-cluster method [2].

2.1.1. Born-Oppenheimer approximation

The first analytical approximation for the molecular potentials stems from the mass differences between electrons and nuclei. Even the lightest nucleus, the proton is 1836 times heavier than the electron, not to mention heavy molecules. Then the speed of nuclei is much smaller with respect to the speed of electrons. As a result, slow and heavy nuclei create an electrostatic field in which the light electron moves very fast and can almost instantaneously respond to any change of the nuclear position. In the first order approximation, the nuclei can be treated as standing still with a cloud of electrons moving around. This is the key idea of the Born-Oppenheimer (BO) approximation, which has become the basis of modern molecular structure theory [3]. The molecular Hamiltonian can be expanded in a series of a dimensionless parameter $\kappa=(m_e/\bar{M})^{1/4}$, where $\bar{M}$ is the reduced mass of the nuclei. In terms of quantum mechanics, it means that the total wavefunction of the system can be separated at leading order into electronic and nuclear parts:

$$\Psi(\boldsymbol{r},\boldsymbol{R}) = \Psi_{el}(\boldsymbol{r},\boldsymbol{R})\Psi_{nuc}(\boldsymbol{R}). \tag{2.4}$$

In the BO approximation, the total energy of the molecule is equal to the sum of the electronic energy for fixed nuclear coordinates and the energy of nuclear motion, which consists of vibrations and rotations. For the special case of a diatomic molecule, the total energy of an electronic state $|n\rangle$ in the molecule-fixed frame of reference is:

$$E_n = E_n^{el}(R) + E_{vib}(R) + E_{rot}(R), \tag{2.5}$$

where $R=|\boldsymbol{R}_1-\boldsymbol{R}_2|$ is the internuclear distance. Thus, for every electronic state there are sets of vibrational and rotational states, characterized by the vibrational quantum number v and the rotational quantum number N, respectively. This is schematically shown in Fig. 2.1 for the ground and electronically exited states of a diatomic molecule. The shape of the potential energy curve is analytically approximated by the Morse potential as $V_M(R)=D_e(1-e^{-\alpha(R-R_e)})^2$, where D_e is the bond energy, R_e is the equilibrium distance, and α plays a role of a stiffness of the potential. In many cases, the three-parameter Morse potential reproduces experimental potential wells quite correctly. However, in modern spectroscopy, the Morse-Long range potential is used as a modified version of the former [4].

A typical binding energy of electrons in a molecule can be roughly estimated as a time-averaged kinetic energy of electrons $W_e=-\langle\hat{T}_e\rangle=-\hbar^2/(2m_e\langle r\rangle^2)$ [5]. If one takes $\langle r\rangle$ to be equal to the equilibrium distance R_0, which is for most diatomic molecules $\simeq$0.1 nm, then W_e is in the order of several eV. This means that most of the electronic transitions lie in the ultraviolet and visible range of

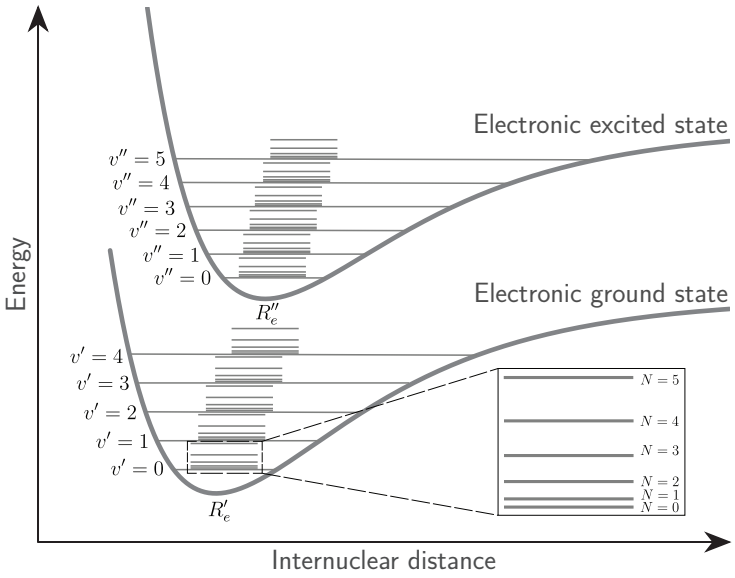

Figure 2.1 | Potential energy curves of a diatomic molecule as a function of internuclear distance (not to scale). The sets of vibrational and rotational levels are shown together with the corresponding quantum numbers. The equilibrium distances R_e are also depicted for each state.

the electromagnetic spectrum. Nuclear motion, as expected, gives rise to lower energies. In Ref. [3], Born and Oppenheimer also showed that the ratio of the vibrational nuclear energy and the electronic energy scales as κ^2. This gives an order of the vibrational energy $E_{vib} \simeq W_e \sqrt{m_e/\bar{M}} \lesssim 0.1$ eV, and corresponding transitions should be found in the infrared part of the spectrum. Lastly, a separation of nuclear motion into vibrations and rotations leads to even smaller energies for a purely rotational energy. It scales as κ^2 with respect to E_{vib}. Thus, the estimated value of the rotational energy is $E_{rot} \simeq W_e m_e/\bar{M} \lesssim 10$ meV. And transitions associated with rotational motion of nuclei usually lie in the far infrared and microwave spectral range.

2.1.2. Rotational and vibrational levels

Here the treatment of nuclear motion is given in more detail, and the previously introduced rotational and vibrational energies are derived explicitly via the corresponding quantum numbers. The Schrödinger equation for the nuclear wavefunction in the molecule's center-of-mass frame is reduced to:

$$\left(-\frac{\hbar^2}{2\bar{M}}\nabla^2 + E_n^{el}(R)\right)\Psi_{nuc}(\boldsymbol{R}) = E_n\Psi_{nuc}(\boldsymbol{R}) \tag{2.6}$$

and can be separated into the radial and angular parts if one does a conversion to a spherical coordinate system. Hence, the kinetic energy term containing the Laplacian can be rewritten in spherical coordinates; and the nuclear wavefunction is equal to $\frac{1}{R}\mathcal{R}(R)Y(\theta,\phi)$, giving rise to two differential equations. The equation for the angular part has the angular momentum operator $\hat{N}$ that commutes with the Hamiltonian. Spherical harmonics $Y(\theta,\phi)$ are always eigenfunctions of the $\hat{N}^2$ operator:

$$\hat{N}^2Y(\theta,\phi) = \hbar^2N(N+1)Y(\theta,\phi). \tag{2.7}$$

Substitution of these eigenvalues into the radial part of the Schrödinger equation gives an effective potential for nuclei in this frame:

$$\left(-\frac{\hbar^2}{2\bar{M}}\frac{d^2}{dR^2} + \frac{\hbar^2N(N+1)}{2\bar{M}R^2} + E_n^{el}(R)\right)\mathcal{R}(R) = E_n\mathcal{R}(R). \tag{2.8}$$

In the simplest rigid rotor model of a diatomic molecule, when the internuclear distance remains constant, the rotational energy (the second term in the previous equation) can be simply written as

$$E_{rot}(N) = B_ehcN(N+1), \tag{2.9}$$

where $B_e{=}\hbar^2/(2\bar{M}R_0^2hc)$ is the rotational constant, and R_0 is the fixed distance between the two nuclei. The factor $1/hc$ is introduced to convert units of B_e in wavenumbers. As can be seen from equation (2.9), the rotational energy depends on the masses of the nuclei and increases rapidly with the rotational number N. Moreover, since the energy separation between adjacent rotational numbers is $E_{rot}(N{+}1){-}E_{rot}(N){=}2B_ehc(N{+}1)$ (as shown in Fig. 2.1), a purely rotational spectrum in the rigid-rotor approximation consists of a series of equidistant lines.

The total energy from equation (2.8) is the sum of the electronic potential $E_n^{el}(R_0){=}T_ehc$ and the rovibrational energy $E_{rv}{=}E_{rot}{+}E_{vib}$. The purely vibrational energy close to the equilibrium distance of a typical molecular potential can be simply considered as the energy of the harmonic oscillator:

$$E_{vib} = \hbar\omega_0(v+\frac{1}{2}) = \omega_ehc(v+\frac{1}{2}), \tag{2.10}$$

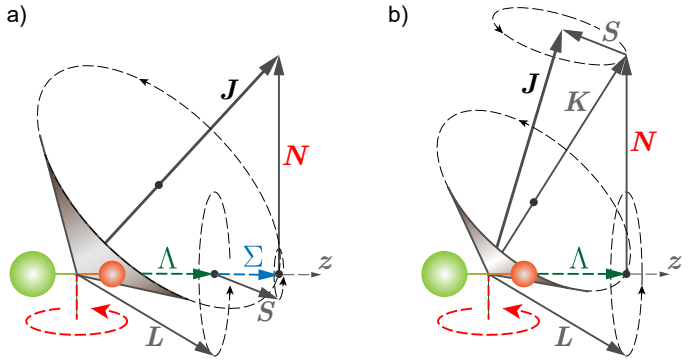

Figure 2.2 | Momentum coupling schemes for Hund's cases (a) and (b). Vector labeling is described in the text.

where $\omega_e{=}\hbar\omega_0/hc$ is the vibrational constant. In Fig. 2.1, some vibrational states are schematically depicted as energetically equidistant levels and denoted with the vibrational quantum number v.

The aforementioned discussion is valid only in a number of approximations, but gives a good qualitative picture. However, in a real molecule, more effects have to be also taken into account. These corrections usually include the potential anharmonicity, stretching correction and vibration-rotation coupling. Therefore, usually the following semiempirical formula is used for a generalized molecular potential [6]:

$$E_{pot}(v,N)/hc = \sum_i \sum_k Y_{ik}(v+\frac{1}{2})^i(N(N+1))^k, \tag{2.11}$$

where Y_{ik} are so-called Dunham coefficients that have a relation with spectroscopically important molecular constants. For instance, the low-order terms are $Y_{10}{\simeq}\omega_e$ (vibrational constant), $Y_{01}{\simeq}B_e$ (rotational constant), $Y_{11}{\simeq}{-}\alpha_e$ (vibrational-rotational coupling constant), $Y_{20}{\simeq}{-}\omega_e\chi_e$ (anharmonicity correction), and $Y_{02}{\simeq}{-}D_e$ (stretching correction). The Dunham coefficients can be calculated by a least-square fitting of energy levels with quantum numbers.

2.1.3. Angular momentum coupling and Hund's cases

In order to fully describe a molecule in different energy states, one has to find a set of good quantum numbers associated with conserved quantities. Besides the rotational quantum number N and the corresponding nuclear rotational momentum $\boldsymbol{N}$, other angular momenta exist in a molecule: electronic angular momentum $\boldsymbol{L}$, electronic spin $\boldsymbol{S}$, nuclear spin $\boldsymbol{I}$, total angular momentum without

spins $\boldsymbol{K}$, total angular momentum excluding nuclear spin $\boldsymbol{J}$, and total angular momentum $\boldsymbol{F}$. Coupling of angular momenta is usually done in a simple vector model. Then, molecular states can be represented by a molecular term symbol $^{2S+1}\Lambda_{\Omega}$, where S is the total electron spin quantum number, Λ and Ω are projections of $\boldsymbol{L}$ and $\boldsymbol{J}$ along an internuclear axis $\boldsymbol{z}$, respectively.

In diatomic molecules, depending on the relative coupling strengths of angular momenta, there are five idealized cases, later referred to as Hund's cases. They play an important role in the interpretation of molecular spectra. Here we examine only two of them, that describe the electronic ground and excited states of SrF as well as most of the electronic states of diatomic molecules.

The electronic ground state of SrF is described by the Hund's case (b). The corresponding term symbol is $X^2\Sigma^+$, which means that the total spin 1/2 comes from a single valence electron and the total electronic angular momentum is 0. Letter X simply denotes a ground state. Fig. 2.2(b) shows the momentum coupling scheme for this state. The Hund's case (b) is applied when coupling of $\boldsymbol{L}$ with $\boldsymbol{S}$ is weak, or when $\boldsymbol{L}$ is 0. Then the projection of $\boldsymbol{L}$ and rotational angular momentum $\boldsymbol{N}$ combine to form $\boldsymbol{K}$. Finally, $\boldsymbol{K}$ couples with $\boldsymbol{S}$ to yield $\boldsymbol{J}$. For the $X^2\Sigma^+$ state, $\boldsymbol{J}=\boldsymbol{K}+\boldsymbol{S}=\Lambda\boldsymbol{z}+\boldsymbol{N}+\boldsymbol{S}=\boldsymbol{N}+\boldsymbol{S}$. Moreover, the interaction of the electron spin with the magnetic field originating from the nuclear rotation

Table 2.1 | Main spectroscopic constants (in cm^{-1}) for the X and A states of $^{88}\mathrm{Sr}^{19}\mathrm{F}$

Molecular parameter	Label	$X^2\Sigma^+$	$A^2\Pi$
Electronic energy	T_e	0	15216.34287*
Rotational constant	B_e	0.24975935*	0.2528335*
Vibrational constant	ω_e	501.96496†	-
Anharmonicity constant	$\omega_e\chi_e$	2.204617†	-
Stretching correction	D_e	2.4967×10^{-7}*	2.546×10^{-7}*
Vibration-rotation	α_e	1.5511^{-3}†	-
Spin-rotation	γ_0	2.4974×10^{-3}*	-
Fine structure constant	A	-	281.46138*
Nuclear spin-rotation	C_{I00}	7.671974×10^{-8}**	-
Nuclear spin-electron spin	b_{00}	3.432437×10^{-3}**	-
Nuclear spin-electron spin (dipole-dipole)	c_{00}	1.104097×10^{-3}**	-
Λ-doubling	p_0	-	0.133002*

* Reference [7]
† Reference [8]
** Reference [9]

leads to a small splitting of every rotational level but N=0. This splitting is determined by the spin-rotation coupling constant γ_v and is different for every vibrational state.

The first electronically excited state of SrF is labeled $A^2\Pi$ and can be characterized by the Hund's case (a), as shown in Fig. 2.2(a). In this state, the electronic angular momentum $\boldsymbol{L}$ is electrostatically coupled to the internuclear axis $\boldsymbol{z}$, and spin $\boldsymbol{S}$ is coupled to $\boldsymbol{L}$ via the spin-orbit interaction. They also precess independently around $\boldsymbol{z}$, and their projections add up to give Ω. The vector $\Omega\boldsymbol{z}$ together with $\boldsymbol{N}$ forms the total angular momentum: $\boldsymbol{J}=(\Lambda+\Sigma)\boldsymbol{z}+\boldsymbol{N}=\Omega\boldsymbol{z}+\boldsymbol{N}$. Since $A^2\Pi$ implies that the projection of electronic angular momentum is 1 and the total spin is 1/2, the excited state is a doublet with two values of Ω: 1/2 and 3/2. The energy splitting between two Ω manifolds is given by the spin-orbit coupling constant A in a similar way as in atoms: $\Delta E=A\Lambda\Sigma$. Besides spin-orbit interaction, this state has another level of degeneracy, called Λ-doubling. This doubling of energy levels is observable for any rotating molecule when $\Lambda\neq0$, including obviously the relevant excited state. Because the projection of electronic angular momentum has two possible values (±1) with different parity, every energy state is two-fold degenerate. The splitting of Λ-doublets is defined by the leading order constant p_v.

Previously, we have not considered the total nuclear spin $\boldsymbol{I}$. It can also be coupled to $\boldsymbol{J}$, giving rise to the hyperfine structure splitting. The most abundant isotope of strontium is ^{88}Sr, which has 38 protons and 50 neutrons yielding the nuclear spin 0. Fluorine has only one stable isotope ^{19}F (9 protons and 10 neutrons) with the nuclear spin I=1/2. Inclusion of this spin leads to the splitting of every J-level into two hyperfine components, however the magnitude of this splitting depends on the particular quantum state. In the most general form, the following terms contribute to the corresponding Hamiltonian [9]: nuclear spin-rotation coupling $C_{IvN}\boldsymbol{I}\cdot\boldsymbol{N}$, nuclear spin-electron spin interaction $b_{vN}\boldsymbol{I}\cdot\boldsymbol{S}$, nuclear spin-electron spin dipole-dipole interaction $c_{vN}(\boldsymbol{I}\cdot\boldsymbol{z})(\boldsymbol{S}\cdot\boldsymbol{z})$, and direct nuclear spin-spin coupling $d_{vN}\boldsymbol{I}_A\cdot\boldsymbol{I}_B$ (which is zero in our case). It is stated that the hyperfine splitting in the $A^2\Pi$ state is less than 3 MHz (or $\simeq 0.0001$ cm^{-1}) and is therefore unresolved [10]. Table 2.1 summarizes experimentally extracted values of the main spectroscopic constants of SrF in the ground and the lowest excited states. In Fig. 2.3, one can see the schematic structure of low-lying rotational energy levels of ^{88}Sr^{19}F in the v=0 level of the $X^2\Sigma^+$ and $A^2\Pi_{1/2,3/2}$ states, with an indication of the main molecular parameters. The total parity eigenvalues of quantum states are also shown on the schematics. The separation between energy levels is not plotted to scale.

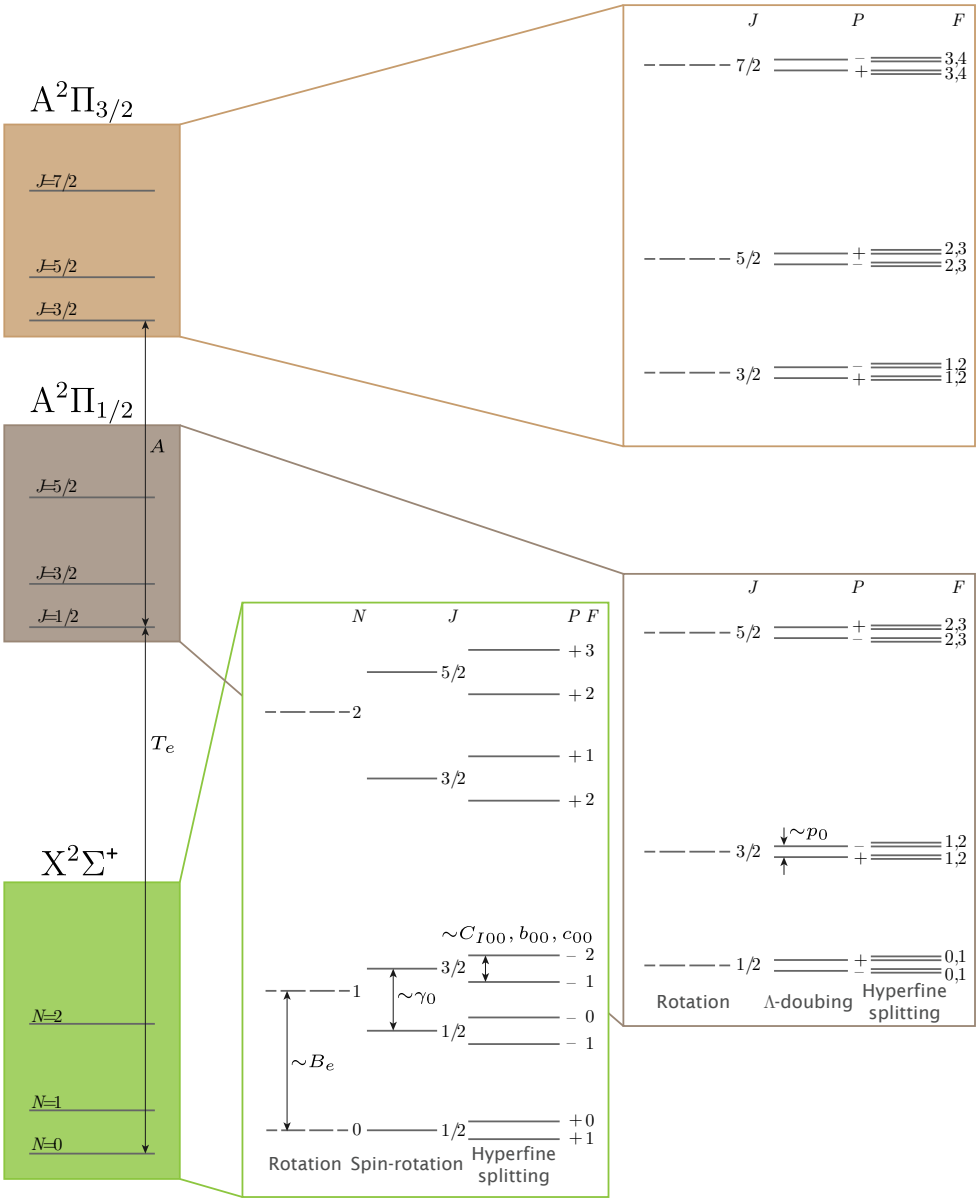

Figure 2.3 | A schematic overview of the energy level structure for the X and A states of $^{88}Sr^{19}F$. The figure is not drawn to energy scale. Only three lowest rotational states are shown for the first vibrational level (v=0). Good quantum numbers and parity are indicated for every state. Values of the labeled spectroscopic constants can be found in Table 2.1.

2.2. Interaction with external fields

Molecules as well as atoms change their energy level structure in the presence of an electric and (or) a magnetic field. Generally, it can lead to additional splitting and shifting of non-perturbed levels depending on the magnitude and the direction of the external field. Here we give a basic theoretical description of these effects in polar molecules with a focus on heavy diatomic ones. These essentials are of great importance for the experimental state-sensitive control of molecules by laboratory-produced fields, especially in the Stark deceleration technique. This technique is based on the state-dependent force that diatomic molecules experience in a spatially inhomogeneous electric field.

2.2.1. Stark effect

The Stark effect, as was already briefly mentioned in the Introduction, is a splitting of energy levels in an external electric field. The effect of small electric field $\mathcal{E}$ can be introduced perturbatively by adding a term to the Hamiltonian. Interaction of the electric dipole moment of the molecule $\boldsymbol{d}$ with an external field $\boldsymbol{\mathcal{E}}$ is then described by $\hat{H}_{\text{Stark}}=-\boldsymbol{d}\cdot\boldsymbol{\mathcal{E}}$. The space-fixed direction of the electric field requires the introduction of the azimuthal quantum number M_N (projection of rotational momentum $\boldsymbol{N}$ along the electric field axis) that runs from $-N$ to N. The second-order perturbation calculations yield that each rotational level is mixed by the electric field with the adjacent rotational levels. The energy shift due to the Stark effect in an open-shell $^2\Sigma$ electronic state is described by the following formula [5]:

$$\Delta E(N, M_N) = \frac{d^2\mathcal{E}^2}{B_e hc} f(N, M_N), \tag{2.12}$$

where we introduced $f(M, M_N)=\frac{1}{2}\frac{N(N+1)-3M_N^2}{N(N+1)(2N-1)(2N+3)}$ for $N>0$, and for the special case $f(0,0)=-1/6$. This equation shows two important features of the second-order Stark shift: it scales quadratically with electric field strength, and every N-level is split into $(N+1)$ Stark components (since M_N also comes in quadratically). Here we list a number of Stark shifts for the lowest rotational levels simply by substituting quantum numbers in equation (2.12): $\Delta E(0,0)=-\frac{1}{6}\frac{d^2\mathcal{E}^2}{B_e hc}$, $\Delta E(1,0)=\frac{1}{10}\frac{d^2\mathcal{E}^2}{B_e hc}$, $\Delta E(1,1)=-\frac{1}{20}\frac{d^2\mathcal{E}^2}{B_e hc}$.

Perturbation theory breaks down once the perturbation becomes large, i.e. when the corresponding matrix element is of the same order as energy splitting between unperturbed states. In the context of molecular Stark shift, this breakdown happens due to the mixing of close-lying rotational levels. The effect is more prominent in heavier molecules where the rotational constant B_e is small,

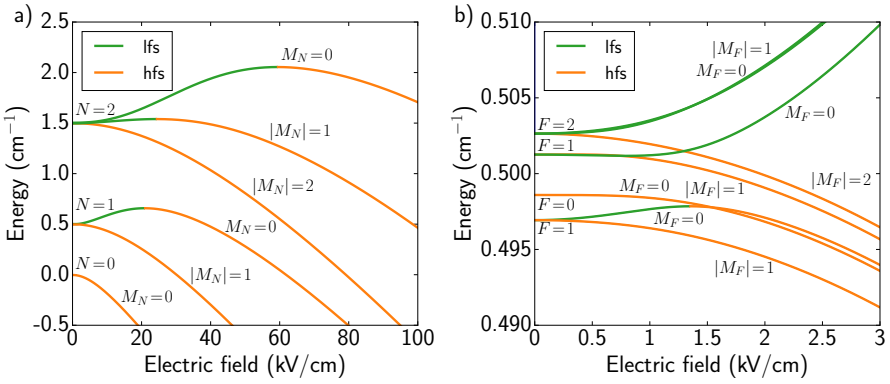

Figure 2.4 | The Stark shift of three lowest rotational levels of $^{88}Sr^{19}F$ (a) and magnification of the same structure around zero-field for $N = 1$ rotational level with the resolved hyperfine structure (b). Levels are labeled with corresponding quantum numbers and colored according their character.

which translates into a small separation between energy levels. In this case, the energy levels at low and high electric field strengths can be calculated by numerical diagonalization of the full Hamiltonian matrix. This procedure is shown in detail in Ref. [11]. Fig. 2.4(a) illustrates the Stark shift of three lowest rotational levels of $X^2\Sigma^+$ (v=0) of SrF in the range of 100 kV/cm obtained with the open source molecular spectra simulator `PGOPHER` [12]. The value of the permanent electric dipole moment d in the ground state is experimentally determined to be 3.4676(10) D [13] and is used throughout these numerical calculations. Other spectroscopic constants taken are summarized in Table 2.1. In Fig. 2.4(b), the hyperfine structure of the same Stark curves for the N=1 rotational level in the range of 0−3 kV/cm is shown.

Molecules in an inhomogeneous external field $\boldsymbol{\mathcal{E}}$ experience a force which is directed opposite to the gradient of the Stark energy: $\boldsymbol{F}=-\boldsymbol{\nabla}E(\mathcal{E})$. Thus, molecules in quantum states that gain energy with an increased electric field strength are attracted towards the local electric field minima. They are conventionally called low-field seeking (lfs) and colored green in Fig.2.4. Other levels, that lose their energy with increasing magnitude of $\boldsymbol{\mathcal{E}}$-field, are attracted towards the field maxima. These levels are called high-field seeking (hfs) and colored orange in Fig.2.4. A transition between lfs and hfs characters occurs for some quantum states. The energy at which this transition occurs depends on the quantum state and increases with the rotational number N. The closely separated hyperfine levels in Fig 2.4(b) are mixed already at low electric field strengths and can give rise to unwanted state transitions, as described in detail in Section 4.2.2.

2.2.2. Zeeman effect

The energy levels of a molecule can also be split into components in the presence of an external magnetic field. The field $\boldsymbol{B}$ exerts a torque on a magnetic moment $\boldsymbol{\mu}$ leading to the Zeeman energy shift, which is described by $\hat{H}_{\text{Zeeman}}=-\boldsymbol{\mu}\cdot\boldsymbol{B}$. The magnitude of a molecular magnetic moment may depend on the electronic state, since generally it consists of the following contributions: magnetic moment due to the valence electron spin $g_S\mu_{\text{B}}\boldsymbol{S}$, magnetic moment due to the orbital motion $g_L\mu_{\text{B}}\boldsymbol{L}$, and the nuclear spin term $g_I\mu_{\text{N}}\boldsymbol{I}$. Here g denotes corresponding dimensionless g-factor, $\mu_{\text{B}}=e\hbar/2m_e$ is the Bohr magneton, and $\mu_{\text{N}}=e\hbar/2m_p$ is the nuclear magneton. Since $\mu_{\text{B}}/\mu_{\text{N}}\simeq 1836$, we can ignore the nuclear spin contribution for simplicity. In this approximation, the change of energy due to the Zeeman effect is expressed by:

$$\Delta E = \mu_{\text{eff}} B, \tag{2.13}$$

where μ_{eff} is an effective magnetic moment, which plays a role of the state-dependent function f from the Stark effect theory. This moment can be rewritten via the time-averaged magnetic moment along $\boldsymbol{J}$ axis as:

$$\mu_{\text{eff}} = \langle\mu_J\rangle\cos(\boldsymbol{J},\boldsymbol{B}) = \langle\mu_J\rangle\frac{M_J}{\sqrt{J(J+1)}} \tag{2.14}$$

with M_J defined as a projection of $\boldsymbol{J}$ along the external field axis. Simple vector considerations lead to the following expressions for $\langle\mu_J\rangle$ [1]:

$$\begin{aligned} \langle\mu_J\rangle &= \frac{(\Lambda+2\Sigma)(\Lambda+\Sigma)}{\sqrt{J(J+1)}}\mu_{\text{B}} && \text{Hund's case (a)},\\ \langle\mu_J\rangle &= \left(\frac{\Lambda^2\cos(\boldsymbol{K},\boldsymbol{J})}{\sqrt{K(K+1)}} + 2\sqrt{S(S+1)}\cos(\boldsymbol{S},\boldsymbol{J})\right)\mu_{\text{B}} && \text{Hund's case (b)}. \end{aligned} \tag{2.15}$$

These formulae are valid only in the case of relatively small magnetic field strengths, i.e. when the field perturbation is smaller compared to the separation between individual terms. The splitting of Zeeman levels in larger range of fields can be calculated by solving the full Hamiltonian, taking into account the hyperfine structure of the energy levels.

The exact treatment of the Zeeman effect in the $X^2\Sigma$ and $A^2\Pi$ states of $^{88}\text{Sr}^{19}\text{F}$ can be found elsewhere [14]. A peculiar situation is observed in the lower $A^2\Pi_{1/2}$ electronic state, where the electron spin and orbital motion contributions to the effective magnetic moment effectively cancel each other. This can be already seen from expression (2.15 a), if one substitutes $\Lambda=1$ and $\Sigma=-1/2$. In reality, there is also a mixing with a higher lying $B^2\Sigma_{1/2}$ electronic state and the

nuclear spin contribution. The resulting splitting in the $A^2\Pi_{1/2}$ state is 10 times smaller than in the ground state [15], which renders a creation of the type-II MOT possible [16].

2.3. Theory of light forces

The manipulation of molecular position and momentum by means of laser light is based on the action of light forces. Everything written in this section is applicable to the case of a molecule, but for simplicity we consider the atom-light interaction. In the presence of a laser beam, an atom couples, on the one hand, to the laser field and, on the other hand, to the quantum vacuum field [17]. The laser field can be treated to be monochromatic with a frequency ω_L and an amplitude $\boldsymbol{\mathcal{E}}_L$. Then the interaction of the atom and the laser beam is described by coupling between the induced atomic dipole moment and the laser electric field. The atom-vacuum field coupling is responsible for the spontaneous emission of photons. It is characterized by the natural width Γ of the excited state, which is also related to the spontaneous emission rate from this state.

The expression for the mean total force exerted by the laser light onto the atom in a two-level model is given by [18]:

$$\mathbf{F}(\mathbf{r}) = -\frac{s\,(\mathbf{r})}{1+s(\mathbf{r})}\left(\hbar\delta\frac{\nabla\Omega(\mathbf{r})}{\Omega(\mathbf{r})}+\frac{\hbar\Gamma}{2}\nabla\phi(\mathbf{r})\right), \tag{2.16}$$

where $s(\mathbf{r})=\frac{\Omega^2(\mathbf{r})/2}{\delta^2+\frac{\Gamma^2}{4}}$ is the saturation parameter, $\delta=\omega_L-\omega_0$ is the detuning from a particular transition frequency ω_0, $\Omega=\frac{1}{\hbar}\boldsymbol{d}\cdot\boldsymbol{\mathcal{E}}_L$ is the Rabi frequency, and $\phi(\mathbf{r})$ is the phase of the laser field. This force is the sum of two contributions that correspond to conservative and dissipative forces.

The first term in equation (2.16), which is proportional to $\nabla\Omega(\mathbf{r})$ is the so-called dipole force:

$$\mathbf{F}_{dip}(\mathbf{r}) = -\hbar\delta\frac{s(\mathbf{r})}{1+s(\mathbf{r})}\frac{\nabla\Omega(\mathbf{r})}{\Omega(\mathbf{r})} \tag{2.17}$$

and its physical meaning will be explained in Section 2.3.2.

2.3.1. Scattering force

The second term in equation (2.16) is proportional to the gradient of the phase:

$$\mathbf{F}_{sc}(\mathbf{r}) = -\frac{\hbar\Gamma}{2}\frac{s(\mathbf{r})}{1+s(\mathbf{r})}\nabla\phi(\mathbf{r}), \tag{2.18}$$

and is called scattering force (or radiation pressure). It plays the main role in the laser cooling mechanism in a Zeeman slower and a magneto-optical trap. To understand the origin of this force, one can consider the case of a plane wave, for which Ω does not depend on the radius vector. Then the phase $\phi(\mathbf{r})$ is equal to $-\mathbf{k}\cdot\mathbf{r}$, where $\mathbf{k}$ is the wave vector, and the phase gradient is simply $-\mathbf{k}$. After substitution in equation (2.18) it gives:

$$\mathbf{F}_{sc} = \frac{\Gamma}{2}\frac{s}{1+s}\hbar\mathbf{k}. \tag{2.19}$$

The first part of this expression is the spontaneous scattering rate and is labeled as $\Gamma_{sp}=\frac{\Gamma}{2}\frac{s}{1+s}$. Thus, the mean dissipative force is given by:

$$\mathbf{F}_{sc} = \Gamma_{sp}\hbar\mathbf{k}. \tag{2.20}$$

In other words, this force implies the momentum transfer of one recoil $\hbar\mathbf{k}$, that happens every time a photon is absorbed from the laser light, whereas this absorption occurs at a rate Γ_{sp}. It is important to notice that not all of the spontaneously emitted photons contribute to the mean force, but only those that push the atom in the direction of the light wave vector, that is why this force is also called radiation pressure. On the other hand, the spontaneously emitted photons can be used for molecule detection in the laser-induced fluorescence method, as described in Section 3.1.3.

One can show that the saturation parameter s can be written in terms of the saturation intensity I_{sat}, defined as $I_{sat}=\frac{\pi hc\Gamma}{3\lambda^3}$:

$$s = \frac{1}{1+\frac{4\delta^2}{\Gamma^2}}\frac{I}{I_{sat}}. \tag{2.21}$$

From this expression it follows that the saturation parameter is equal to I/I_{sat} in the case of the resonance condition (δ=0). And the scattering force saturates to its maximum value $\mathbf{F}_{sc}=\frac{\Gamma}{2}\hbar\mathbf{k}$ when $I\gg I_{sat}$.

The Doppler cooling mechanism is based on the Doppler shift $-\mathbf{kv}$ of the laser frequency when the atom moves with velocity $\mathbf{v}$. In this case, the scattering force is velocity dependent because the detuning, entering in its expression, is shifted: $\delta'=\delta-\mathbf{kv}$. In the linear approximation, one can obtain the following expression for the radiation pressure:

$$\mathbf{F}_{sc}(\mathbf{v}) \simeq \mathbf{F}_{sc}(\mathbf{v}=0) - \frac{\alpha}{2}v_z\mathbf{e}_z, \tag{2.22}$$

where the first term is the force for zero velocity, and the second one is proportional to the component of velocity in the direction of the laser, the expression for α is $-\frac{2s_0}{1+s_0}\frac{\delta\Gamma}{\delta^2+\Gamma^2/4}\hbar k^2$, s_0 is the saturation parameter taking into account the

Doppler shift $s_0{=}\frac{\Omega^2/2}{\delta'^2+\Gamma^2/4}$, $\mathbf{e}_z$ is the direction of wave vector, such that $\mathbf{k}{=}k\mathbf{e}_z$, and v_z is z-component of $\mathbf{v}$. The second term in equation (2.22) describes the force that is opposite to the direction of velocity when $\alpha{>}0$, that occurs for $\delta{<}0$ (red detuning).

The laser cooling technique requires many repetitive momentum kicks from the absorption of red-detuned photons counter-propagating to the atomic motion. In order to cool down an atom with mass of around 20 amu from the room temperature to ultracold temperatures using light in the visible spectrum, one needs around 10^4 photons to be scattered [19]. The atom must also have a closed cycling transition in which every photon absorption event is always followed by the spontaneous decay back to the initial state. However, there is practically always a non-zero probability to spontaneously decay to another energy level [20], limiting the overall efficiency of the laser cooling process. To combat this, additional repump lasers are used to depopulate unwanted (dark) states and return the population in the main laser cooling cycle. A thorough analysis of laser cooling methods in application to SrF molecules and similar polar molecules can be found in Ref. [21].

2.3.2. Dipole force

In this subsection, the origin of dipole force is briefly explained. The expression (2.17) can be easily simplified, taking into account that $\frac{\nabla\Omega(\mathbf{r})}{\Omega(\mathbf{r})}{=}\frac{1}{2}\frac{\nabla s(\mathbf{r})}{s(\mathbf{r})}$. Then the expression for the dipole force is given by:

$$\mathbf{F}_{dip}(\mathbf{r}) = -\frac{\hbar\delta}{2}\frac{\nabla s(\mathbf{r})}{1+s(\mathbf{r})}. \tag{2.23}$$

As one can see, this force is equal to zero in two cases: if the detuning δ is 0 (on-resonance condition) and if the saturation parameter does not depend on radius vector (plane wave). After integration of equation (2.23), one can obtain the following expression for the dipole potential:

$$U_{dip}(\mathbf{r}) = \frac{\hbar\delta}{2}\ln\left(1+s(\mathbf{r})\right), \tag{2.24}$$

which means that the dipole force is a conservative force, and the corresponding potential can be used for optical trapping of atoms and molecules. If $|\delta| \ll \Gamma,\ \Omega$ (far-off resonant), then the saturation parameter is much smaller than 1, and one can expand the logarithm. In this case, the dipole potential is simply $U_{dip}(\mathbf{r}){=}\frac{\hbar\delta}{2}s(\mathbf{r})$ and, after substitution of expression (2.21), it is given by:

$$U_{dip}(\mathbf{r}) = \frac{\hbar\Gamma^2}{8\delta}\frac{I(\mathbf{r})}{I_{sat}}. \tag{2.25}$$

If δ is positive ("blue" detuning), this potential has a maximum at the location where the intensity of the laser field is highest, and the atom (or molecule) is expelled from regions of high intensity. If δ is negative ("red" detuning), the dipole force acts in the direction of higher intensity, and U_{dip} is an attractive potential. The dipole force then directs atoms towards the region of maximum intensity, so in order to create a conservative optical dipole trap, one has to make an inhomogeneous distribution of the laser intensity. This can be achieved e.g. in the focus of the laser beam, or in the standing optical wave inside a cavity.

The interaction potential of the dipole moment and the driving laser field can also be expressed in terms of the complex polarizability α, which depends on the driving frequency ω_L, as [22]:

$$U_{dip}(\mathbf{r}) = -\frac{1}{2\epsilon_0 c}\mathrm{Re}(\alpha)I(\mathbf{r}). \tag{2.26}$$

Thus, the potential energy of the atom in the field is proportional to the real part of polarizability, which describes the in-phase component of the dipole oscillation. On can obtain the general expressions for the dipole potential and the scattering rate in the rotating-wave approximation:

$$U_{dip}(\mathbf{r}) = \frac{3\pi c^2}{2\omega_0^3}\frac{\Gamma}{\delta}I(\mathbf{r}), \tag{2.27}$$

$$\Gamma_{sc}(\mathbf{r}) = \frac{3\pi c^2}{2\hbar\omega_0^3}\left(\frac{\Gamma}{\delta}\right)^2 I(\mathbf{r}), \tag{2.28}$$

where ω_0 is the optical transition frequency. This result shows an essential point for optical trapping, namely the different scaling behavior of two relevant values. The dipole potential scales as I/δ, whereas the scattering rate scales as I/δ^2. Therefore, optical dipole traps usually use large detunings and high intensities to keep the scattering rate as low as possible at a certain potential depth.

References

[1] W. Demtröder, *Molecular Physics: Theoretical Principles and Experimental Methods* (Wiley-Blackwell, Weinheim, Germany, 2007).

[2] R. J. Bartlett and M. Musiał, *Coupled-cluster theory in quantum chemistry,* Rev. Mod. Phys. **79**, 291 (2007).

[3] M. Born and R. Oppenheimer, *Zur quantentheorie der molekeln,* Annalen der Physik **389**, 457 (1927).

[4] R. J. Le Roy and R. D. E. Henderson, *A new potential function form incorporating extended long-range behaviour: application to ground-state* Ca_2*,* Mol. Phys. **105**, 663 (2007).

[5] I. V. Hertel and C.-P. Schulz, *Atoms, Molecules and Optical Physics 2* (Springer, Berlin, Germany, 2015).

[6] J. L. Dunham, *The Energy Levels of a Rotating Vibrator,* Phys. Rev. **41**, 721 (1932).

[7] P. M. Sheridan, J.-G. Wang, M. J. Dick, and P. F. Bernath, *Optical-Optical Double Resonance Spectroscopy of the* $C^2\Pi-A^2\Pi$ *and* $D^2\Sigma-A^2\Pi$ *Transitions of SrF,* J. Phys. Chem. A **113**, 13383 (2009).

[8] P. Colarusso, B. Guo, K.-Q. Zhang, and P. F. Bernath, *High-Resolution Infrared Emission Spectrum of Strontium Monofluoride,* J. Mol. Spectrosc. **175**, 158 (1996).

[9] W. J. Childs, L. S. Goodman, and I. Renhorn, *Radio-frequency optical double-resonance spectrum of SrF: The* $X^2\Sigma^+$ *state,* J. Mol. Spectrosc. **87**, 522 (1981).

[10] J. Kändler, T. Martell, and W. E. Ernst, *Electric dipole moments and hyperfine structure of SrF* $A^2\Pi$ *and* $B^2\Sigma^+$*,* Chem. Phys. Lett. **155**, 470 (1989).

[11] J. E. van den Berg, *Traveling-wave Stark deceleration of SrF molecules*, Ph.D. thesis, University of Groningen (2015).

[12] C. M. Western, *PGOPHER: A program for simulating rotational, vibrational and electronic spectra,* J. Quant. Spectr. Rad. Transfer **186**, 221 (2017).

[13] W. E. Ernst, J. Kändler, S. Kindt, and T. Törring, *Electric dipole moment of SrF* $X^2\Sigma^+$ *from high-precision stark effect measurements,* Chem. Phys. Lett. **113**, 351 (1985).

[14] J. F. Barry, *Laser cooling and slowing of a diatomic molecule*, Ph.D. thesis, Yale University (2013).

[15] M. R. Tarbutt, *Magneto-optical trapping forces for atoms and molecules with complex level structures,* New J. Phys. **17**, 015007 (2015).

[16] M. H. Steinecker, D. J. McCarron, Y. Zhu, and D. DeMille, *Improved Radio-Frequency Magneto-Optical Trap of SrF Molecules,* ChemPhysChem **17**, 3664 (2016).

[17] C. Cohen-Tannoudji, ed., *Atomic motion in laser light (Les Houches session LIII, July 1990),* in *Fundamental systems in quantum optics* (Elsevier, 1992) pp. 12–22.

[18] H. Perrin, *Les Houches lectures on laser cooling and trapping* (2014).

[19] E. S. Shuman, J. F. Barry, and D. DeMille, *Laser cooling of a diatomic molecule,* Nature **467**, 820 (2010).

[20] P. W. Atkins and R. S. Friedman, *Molecular Quantum Mechanics* (Oxford University Press, 2010).

[21] C. Meinema, *Obtaining ultracold molecules through Stark deceleration and laser cooling*, Ph.D. thesis, University of Groningen (2016).

[22] R. Grimm, M. Weidemüller, and Y. B. Ovchinnikov, *Advances in atomic, molecular, and optical physics,* (Academic Press, 2000) Chap. Optical Dipole Traps for Neutral Atoms, pp. 95–170.

3

Stable performance of a traveling-wave Stark decelerator

A number of experimental techniques have hitherto been developed for decelerating relatively fast molecular packets (300−1000 m/s) down to a low forward velocity (50−150 m/s) [1]. The velocity range after deceleration vastly depends upon the type of molecular species, their method of production, and the experimental approach which is chosen to state-selectively control the molecular beams. The current chapter covers the description of our experimental methods and results on guiding and deceleration of a supersonic beam of SrF molecules in a 4 meter long Stark decelerator. Stark deceleration has proven to be a reliable way of preparing cold neutral molecules, including heavy ones with an initially large kinetic energy. The production of heavy molecules at sufficiently low temperatures makes a variety of new fundamental physics tests possible.

3.1. Experimental setup

Our experimental setup has been designed and built for producing, slowing down and detecting heavy diatomic molecules. Therefore, it can be structurally separated into three parts: a molecular beam source, modular traveling-wave Stark decelerator (TWSD) and detection system. Their descriptions are given below.

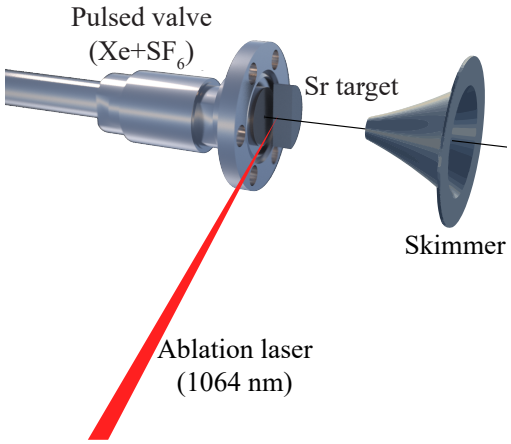

Figure 3.1 | A schematic drawing of the source chamber for producing supersonic beam of SrF molecules.

3.1.1. Molecular beam source

The main components of the molecular source are illustrated in Fig. 3.1. The beam of neutral SrF molecules is produced in a high-vacuum chamber, where a home-made Sr metal target is hit by a high-energy ablation laser beam in the presence of xenon (Xe) and sulfur hexafluoride (SF_6). The target has a thickness of ∼10 mm and is placed at the opening of a supersonic valve (Series 9 General Valve). For ablation process, we use an Nd:YAG pulsed laser which makes ∼60 mJ pulses with a duration of ∼5 ns at its fundamental wavelength of 1064 nm. In order to reduce degradation of the target, it is mounted on a linear positioner that makes a stepwise motion with respect to a static position of the laser beam. The ablation laser as well as other pulsed components of the apparatus have a repetition rate of 10 Hz. During the ablation process, material is removed from the target forming plasma, and then a chemical reaction takes place between the ablation products and the SF_6 gas. There is a lack in understanding the exact dynamics of chemical processes in the highly-ionized environment which is relevant for our situation. However, the room-temperature studies of gas-phase reactions have shown that the most probable reaction channel is the following [2]:

$$Sr^+ + SF_6 \rightarrow SrF^+ + SF_5 \rightarrow SrF + SF_5^+. \tag{3.1}$$

The SrF radicals are cooled by a supersonically expanding carrier gas. Therefore, a gas mixture containing 3% of SF_6 and 97% of Xe is kept at a pressure of 4 bar behind the valve and is injected prior to ablation laser pulses. The duration and

timing of the valve opening are regulated by a magnetically actuated plunger. At a 60 mm distance from the laser ablation spot, there is a conical skimmer with a diameter of 2 mm which filters out the densest part of the molecular beam and prevents formation of shockwaves. At the exit of the skimmer, the resulting molecular beam has a Gaussian velocity distribution centered at 350 m/s with a spread of 10% in the forward direction, and with a FWHM of ∼5 m/s in the transverse direction. The supersonic valve is also designed in such a way that a cold nitrogen gas can flow through its housing leading to reduction of the carrier gas temperature. The temperature of the valve housing can be read out using a J-type thermocouple. In order to control the valve temperature, one can change the mass flow rate of the cold nitrogen with a gas flow controller or the temperature of the transport tube using a heater element. A manual feedback system is used to stabilize the valve temperature. However, this stabilization remains difficult due to a slow response of the system to the changes of the flow rate and transport tube temperature. Attaching the heater element to the valve housing would facilitate the carrier gas temperature control. In practice, the temperature of the valve can be stabilized to ∼1 K within 10 minutes, which is typical for one experimental run, and can drift up to 10 K during the course of the day. When the valve cooling is implemented, the mean forward velocity of the molecular beam can be reduced to 290 m/s and is limited by the condensation temperature of Xe gas.

3.1.2. Modular Stark decelerator

In this section, a brief description of the modular TWSD is given. The detailed overview of its design and principle of operation can be found in the PhD thesis of J. van den Berg [3]. The original idea and proof-of-principle experimental results in a chip-based microstructured array of electrodes are shown in Refs. [4, 5]. The design of the macroscopic TWSD and first deceleration results can be found in the paper by Osterwalder *et al.* [6].

Principle of operation

The key concept of the Stark deceleration is based on generation of a movable and controllable inhomogeneous distribution of an electric field, that serves as a traveling potential well for low-field seeking (lfs) molecular states. Initially, molecules within the phase-space acceptance of the decelerator fill up the local electric field minima, while gradual reduction of their speed along the forward speed axis of the molecular beam will be translated in reduction of the kinetic energy of the molecules. In a traditional Stark decelerator, the operational principle is based on the rapid electric field switching between two configurations. It results in a quasi-continuous motion of electric field minima and corresponding

electric traps for lfs molecules [7]. In a TWSD, true three-dimensional potential wells are created inside an array of equally-separated ring-shaped electrodes to which a high voltage is applied. The applied oscillating voltage of each individual electrode is phase-shifted between adjacent rings and can have a time-dependent frequency. If the frequency of the waveform is constant, it corresponds to a constant speed of the traveling potential, whilst for deceleration of the potential, a gradual chirp of the frequency is required. Moreover, the ring electrodes are connected together in a periodic manner such that every 8-th electrode has the same potential. The voltage applied to the n-th electrode is given by:

$$V_n(t) = V_a \sin(-\frac{2\pi}{l}\int_0^t v(\tau)d\tau + \frac{2\pi n}{8}), \tag{3.2}$$

where V_a is the voltage amplitude, l is the period of applied voltage, and $v(t)$ is the instantaneous velocity of the waveform. Two modes of operation exist: guiding mode and actual deceleration. For guiding with a constant velocity v_0, and for constant deceleration from v_i to v_f in a L_0-long decelerator, the expression (3.2) can be reduced to:

$$\begin{aligned} V_n(t) &= V_a \sin(-\frac{2\pi v_0 t}{l} + \frac{2\pi n}{8}) && \text{constant velocity (a)},\\ V_n(t) &= V_a \sin(-\frac{2\pi}{l}(v_i t - \frac{at^2}{2}) + \frac{2\pi n}{8}) && \text{constant deceleration (b)}, \end{aligned} \tag{3.3}$$

where a constant deceleration is introduced as $a{=}\frac{v_i^2-v_f^2}{2L_0}$. In Fig. 3.2(a), the instantaneous voltage for each of 8 electrodes is shown for two moments in time. Two most extreme cases occur when the overall phase of the sine is equal to an integer and a half-integer number multiplied by $\pi/4$. The two phases shown here are therefore $\phi{=}0$ and $\phi{=}\pi/8$. A voltage amplitude V_a of 5 kV is applied to the electrodes. The phase shift of $\pi/4$ between any adjacent electrodes is also visible on the graph. The cross-section view of the corresponding electric field distributions at the plane through the center of the rings as well as the field vector lines are illustrated in Fig. 3.2(b,c). Electric field minima and saddle points, which are alternately located along the longitudinal axis, create three-dimensional potential wells for lfs molecules. The potential depth for a molecule in a certain quantum state depends on the shape of the corresponding Stark curves (see Fig. 2.4). The 1D projection of the electric field through the trap center is shown in Fig. 3.2(d). The potential depth in the longitudinal direction for SrF molecules in the lfs $X^2\Sigma^+$ $(N, M_N){=}(1, 0)$ rotational state is 0.16 cm^{-1}, which can be seen in Fig. 3.2(e). The confinement in the radial direction depends significantly on the trap position inside the array of electrodes. It is larger when

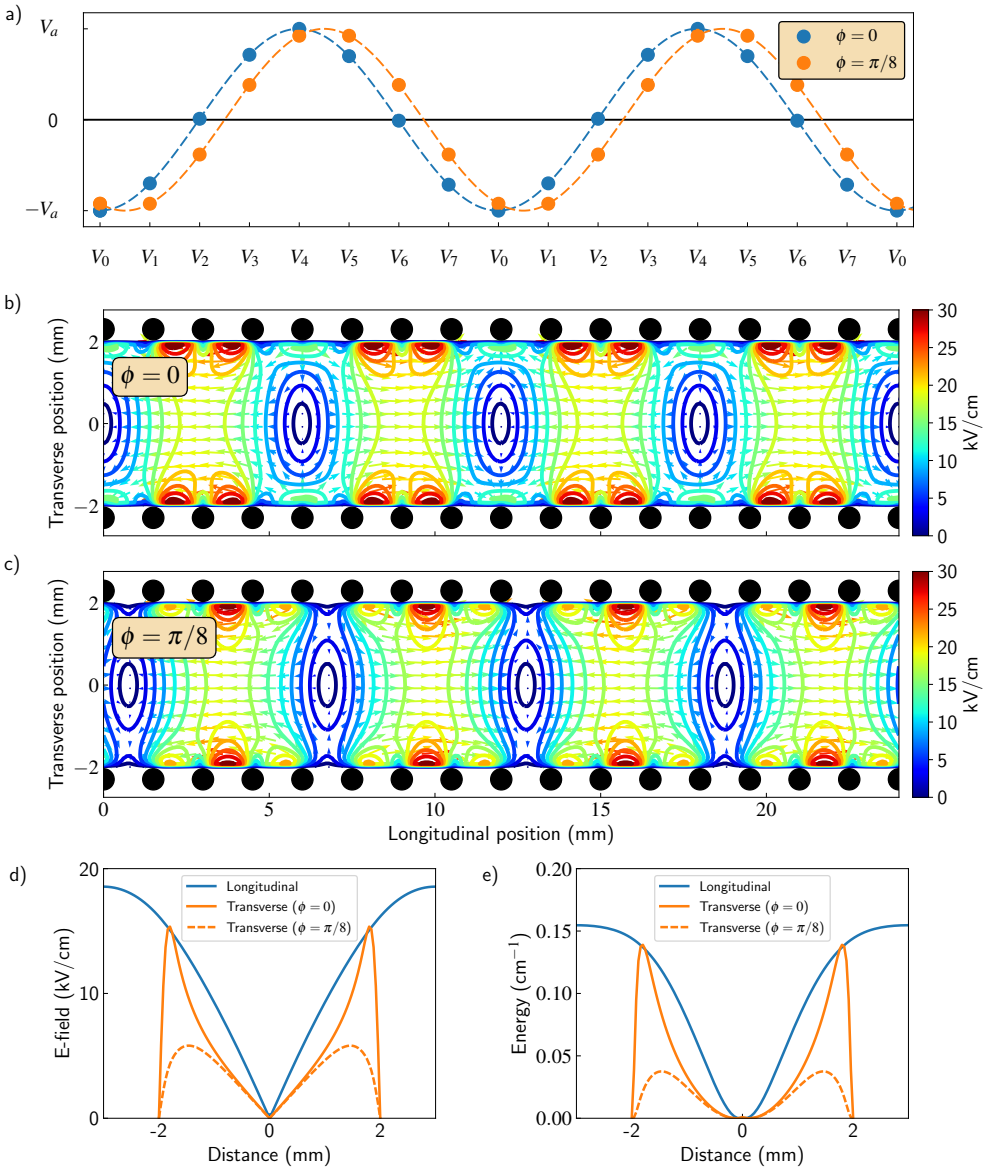

Figure 3.2 | (a) Applied voltage V_n of n-th electrode for two phases of the sine with dashed curves as the guide for eyes. Corresponding contour lines of a constant electric field inside the array of electrodes (black circles) for ϕ=0 (b) and ϕ=$\pi/8$ (c). Contours are spaced by 2.5 kV/cm. The direction of the field is shown by vector lines. The dimensions are taken from the design specifications. Electric field (d) and potential well (e) for SrF in the (N, M_N)=$(1, 0)$ quantum state demonstrate a confinement in all directions at two extreme configurations of the voltage.

the potential well minimum is centered in plane of the rings (ϕ=0) compared to the case when the minimum is exactly in between two rings (ϕ=π/8). It is also worth mentioning that there are two electric traps, separated by 6 mm, with an opposite orientation of the electric field vectors for one spatial period of the applied voltage.

Design

Our TWSD setup consists of several identical modules that are connected together mechanically and electrically. This modular design allows for flexibility in the construction phase and planning of the experiment. In Fig. 3.3(a), one of the modules is depicted. It has a total length of 504 mm and consists of 8 rods supported by an alignment mechanism. Each rod holds 42 ring electrodes made of tantalum and equally spaced by 12 mm. The inner diameter of the electrode is 4 mm, and its thickness is 0.6 mm. In Fig. 3.3(b), one can see an enlarged image of the end of the module where the array of rings is visible. The thickness of the rings and their periodicity leads to an inter-electrode distance of 0.9 mm, which is also shown in Fig 3.2(b).

Deceleration of heavy molecules to a standstill results in a substantial stopping distance. In order to make a long decelerator, a number of modules are connected together. Then the modules are placed inside a vacuum chamber on top of special aluminum rails that allow for the alignment of modules with respect to each other. In the first generation of our decelerator, 4 modules were connected together forming a 2016 mm long TWSD. More information about this apparatus and obtained experimental results can be found in Ref. [8]. The next generation of the decelerator was built from 8 modules, resulting in an approximately 4 m long decelerator. Operation of this TWSD and the deceleration results are shown in the next section. Finally, the current version of the apparatus consists of 9 modules and is 4536 mm long. Since I have spent most of my PhD period working with this 4.5 m long TWSD, the related findings and results are shown in a separate chapter (Chapter 4).

High-voltage electronics

In order to guide and decelerate molecules, high-voltage (HV) electronics has to deliver required voltage as a function of time. The amplitude of the applied voltage determines the depth of the potential well, taking into account a convolution of the Stark shift with the electric field distribution. For SrF molecules in the $X^2\Sigma$ (v=0, N=1, M_N=0) state to be most efficiently trapped by local field minima, the voltage amplitude has to be high enough to reach a turning point on the Stark curve. For our decelerator geometry, this amplitude is equal to 5 kV, which corresponds to an electric field of 21 kV/cm at the turnover point (see Fig. 2.4). From equations (3.3) one can estimate a radial frequency

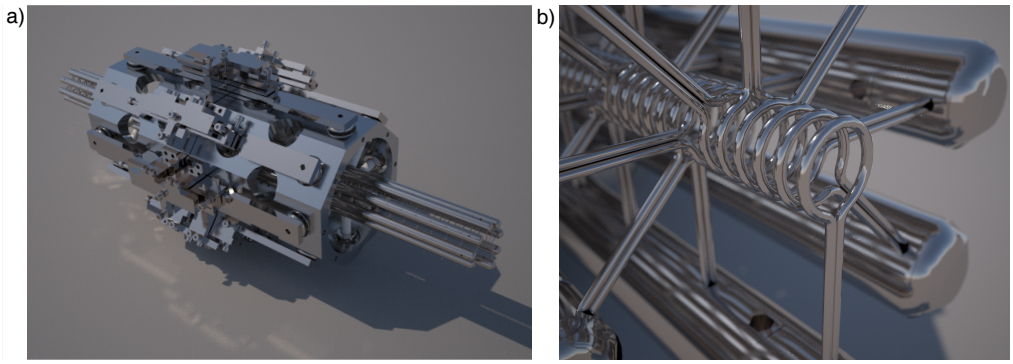

Figure 3.3 | (a) A 3D computer rendered image of one TWSD module with the alignment mechanism. (b) The magnification of the ring electrodes at the end of the module.

of the sinusoidal waveform at which a supersonic beam from the source can be captured (ω=$2\pi v/l$). Thus, for a starting speed of 350 m/s it is equal to $2\pi\times$29.2 kHz. Therefore, we conclude that HV supplies for the TWSD should be able to maintain a voltage amplitude of 5 kV and have a bandwidth of at least 30 kHz during the deceleration period at a repetition rate of 10 Hz. The operational time of the HV suppliers during one experimental run can be simply estimated as the stopping distance divided by the average velocity of the traps, and depends on the length of the decelerator. As an example, for a complete slowing a beam from v_i=350 m/s in the 4.5 meter long TWSD, one needs to gradually chirp the frequency from 29.2 kHz to DC in 25.9 ms.

The amplifiers developed and manufactured for us by Trek Inc. (model PD10039) have met all aforementioned requirements. According to the specifications, they have a fixed voltage gain of 1000 V/V, and are capable of delivering a sine wave with an amplitude of up to 10 kV_{pp} and have a bandwidth of 30 kHz. Heating of the electronics limits the duration of the frequency sweep to 30 ms, which is followed by a 70 ms cooling period. In addition, the amplifiers must be able to supply a current to charge the effective capacitive load of the decelerator. This load is inevitable for our apparatus and can cause instabilities of the HV amplifiers. There are two sources of the capacitive load in our circuitry: the effective capacitance between all neighboring rods and the capacitance between electrodes and ground. The total capacitance between rods is an additive value as it is equivalent to a number of capacitances between individual electrodes connected in parallel. Therefore, an increase of the decelerator length leads to an increased effective capacitive load per amplifier. The measurements in the 4.5 m long TWSD indicated that the capacitance between any adjacent rods is $\sim$160 pF, and between the rods and ground is $\sim$57 pF [9]. For deter-

mining the capacitance between neighboring electrodes, we have measured low impedance using Keysight E4990A impedance analyzer via the auto-balancing bridge method [10]. To measure the capacitance between individual rods and ground, the total capacitance between electrically connected rods and ground was divided by 8. In Fig. 3.4, the equivalent circuit of the TWSD is illustrated.

The original waveform signal is produced by an 8-channel arbitrary waveform generator (AWG Acquitek DA8150) at a sampling frequency of 5 MHz. The parameters of the waveform such as a frequency, voltage amplitude, phase components, or higher order harmonics can be controlled separately in a programmable manner. First, the waveform signal from the AWG passes a linear pre-amplifier and then is sent to the fast HV amplifiers. The amplified signal is delivered to the electrodes via vacuum electrical feedthroughs. Each HV amplifier is also equipped with the voltage and current monitor outputs, so these parameters can be measured and analyzed instantaneously. The fast negative feedback system of the HV amplifiers ensures that the difference between input and output signals is minimized. In order to avoid amplifiers being driven into oscillation due to capacitive coupling between them, we reduced the bandwidth of the feedback system. The side effect of this measure is a significant distortion of the waveforms in the output signal of the amplifiers, which is described in detail in Section 4.2.4.

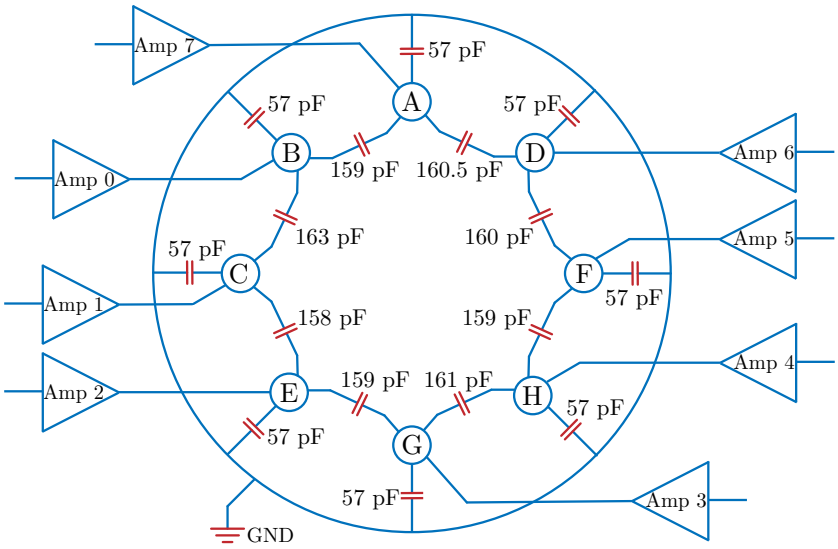

Figure 3.4 | The electronic equivalent circuit of the decelerator. The values of the capacitance were measured for a 4.5 m long decelerator. The rods with electrodes (labeled A through G) have each a capacitance of 57 pF to ground and ∼160 pF to each nearest neighbor Each rod is connected to a high-voltage amplifier labeled by its sequence number.

3.1.3. Detection system

In order to detect SrF molecules at the exit of the decelerator, we use a resonant laser-induced fluorescence (LIF) scheme. Availability of lasers at the $X-A$ transition wavelength in the red part of the visible spectrum makes this detection approach possible. Furthermore, due to a favorable structure of these molecules, the detection laser system can also be easily adapted to direct laser cooling of molecules to reduce their temperature after the Stark deceleration process.

The main components of the optical setup for detecting SrF molecules are shown in Fig. 3.5. A home-built external cavity diode laser (ECDL) is used to drive the strong $A^2\Pi_{1/2}(v'{=}0, J{=}1/2) \leftarrow X^2\Sigma^+(v{=}0, N{=}1)$ transition at a wavelength of 663 nm. The radiative lifetime of the excited state is 24.1±2.0 ns [11], which implies a fast scattering rate of photons. Relevant rovibrational energy levels and transitions are depicted in Fig. 3.6. Here Franck-Condon factors (FCF) f_{nm} indicate branching ratios of spontaneous decay from $v'{=}n$ to $v{=}m$ vibrational state and are of great importance for laser cooling. Highly diagonal values of the FCFs for the same vibrational numbers in SrF [12] render the laser cooling possible. At the same time they lead to more efficient resonance detection, since one molecule can scatter multiple photons. The typical output

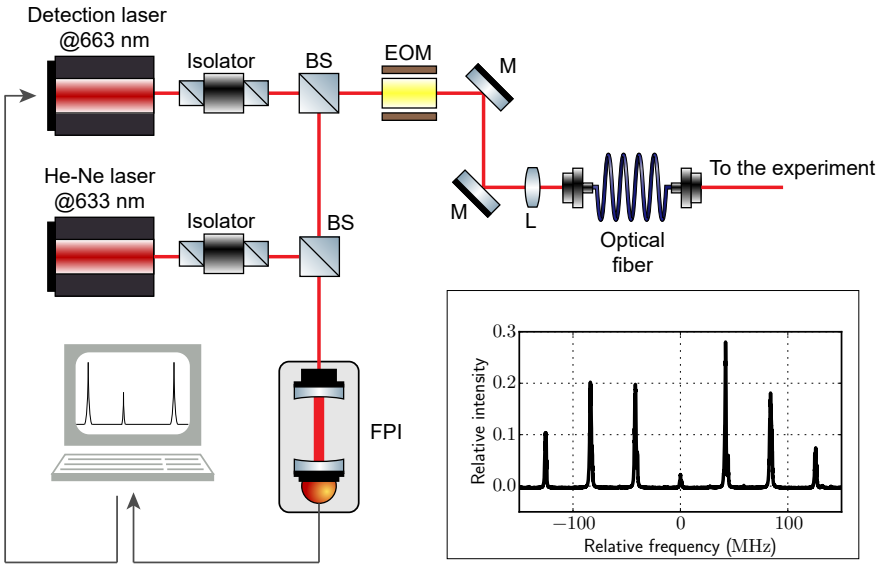

Figure 3.5 | The main components of the laser setup with the transfer cavity locking implementation. The inset shows the laser spectrum for addressing all hyperfine ground-state sublevels.

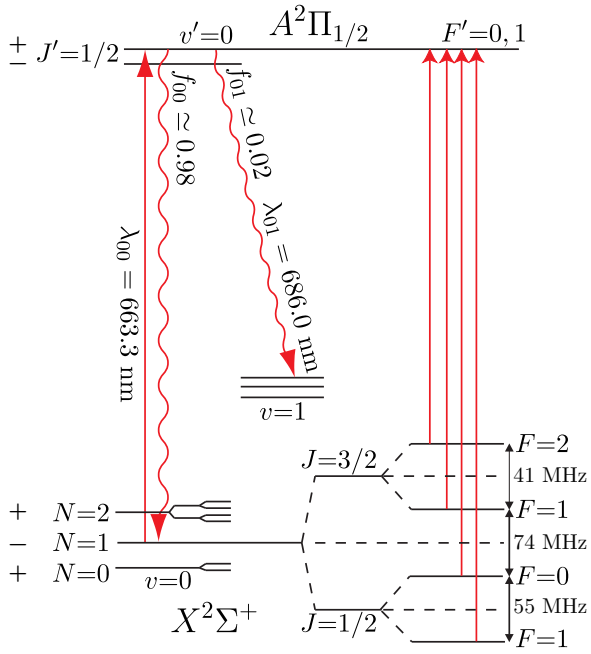

Figure 3.6 | The energy level structure of SrF molecules that are relevant for the detection. The figure is reprinted from Ref. [3].

optical power of the ECDL is 50 mW. A part of the laser light is sent to a scanning Fabri-Perot cavity, where the laser frequency is locked relatively to a stabilized He-Ne laser. The locking principle is based on a feedback loop for the frequency difference between the ECDL and the reference laser, making use of an optical analyzer and a computer microcontroller [13]. A linewidth of 1 MHz of the detection laser is routinely achieved. Another part of the light passes a semiconductor optical amplifier (BoosTA from Toptica Photonics) and is directly coupled into an optical fiber. In order to address all hyperfine components of the ground state (see Section 2.1.3), the light passes through an electro-optical modulator (EOM) which is driven by a sinusoidal signal with a frequency of 42 MHz and a modulation index of 2.6. The spectral characterization of the laser light is shown in the inset of Fig. 3.5. Finally, the amplified light is sent to the experimental chamber through an optical fiber.

In the detection vacuum chamber connected to the exit of the decelerator, the light from the optical fiber is transformed into a free-space collimated beam with a $1/e^2$ diameter of 3 mm and a power of 5 mW. This laser beam crosses the molecular beam under 90° and is retro-reflected by a mirror. The fluorescence light is collected by a plano-convex lens and a mirror, and passes through a

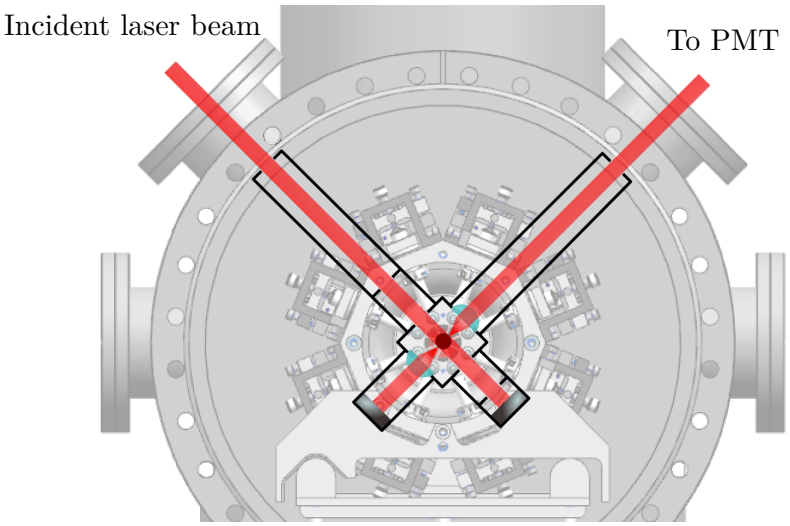

Figure 3.7 | A schematic drawing of the detection unit at the exit of the TWSD. The incoming detection laser beam enters the vacuum chamber via a viewport and is reflected back from a dielectric mirror. The two lenses and the mirror collect the fluorescence light as a parallel beam which is then sent to a PMT. The figure is reprinted from Ref. [3].

single-band bandpass interference filter (Semrock FF01-661/20-25), centered on 661 nm with a bandwidth of 20 nm. To determine the total collection solid angle, we use the following formula:

$$\Omega = 2{\times}2\pi \left(1 - \frac{d}{\sqrt{r^2 + d^2}}\right), \tag{3.4}$$

where d is the distance from the collection lens to the molecular beam axis, r is the radius of the lens, and factor 2 takes into account fluorescence collection from the second hemisphere. For our geometry and lens system, the solid angle is 1.33 sr, which covers almost 10% of the total area. After the filter, a lens focuses this light through an adjustable iris onto the cathode of a photomultiplier tube (PMT). The front view of the detection unit components inside the vacuum chamber as well as light propagation (in red) are shown in Fig. 3.7. The data-acquisition system records the arrival times of the photons and results in binned time-of-flight (TOF) profiles. More details on how we obtain and process the time-of-flight data can be found in Section 4.1.1.

3.2. Operation of a 4 meter long decelerator[1]

In this section, we present and discuss the experimental results obtained with a 4 meter long TWSD on guiding and deceleration of a supersonic beam of SrF molecules. First, the simplest alternating current (AC) guiding mode of operation is shown, and then the deceleration results are presented. Finally, the experimental results are compared with trajectory simulations and with other experiments on Stark deceleration of various species.

3.2.1. Guiding mode

The AC guiding mode of operation is achieved when the voltage oscillations obey equation (3.3 a). The electric field distribution and potential wells for lfs molecules propagate with a constant speed, which is selected to coincide with some velocity class of the initial molecular beam. Fig. 3.8 shows both guiding and deceleration TOF profiles of SrF molecules in the (N, M_N)=$(1, 0)$ rotational states with a bin size of 10 μs. The laser ablation of the target corresponds to t=0. Each plot represents a measurement of 10 min. The uppermost histogram in Fig. 3.8(a) shows the arrival time of molecules with a constant velocity of 300 m/s, which is achieved by cooling the supersonic valve down to ∼210 K. The central peak around 14.3 ms is formed by the molecules that are within the longitudinal phase-space acceptance of the decelerator. The two adjacent wings correspond to the molecules that are outside the longitudinal but inside the transverse acceptance. The guiding velocity is slightly lower than the mean velocity of the initial molecular beam, which can be seen from the shape asymmetry of the TOF.

3.2.2. Deceleration mode

Deceleration of molecules can be implemented by chirping the frequency of oscillating voltages following equation (3.3 b). The 2nd, 3rd, 4th and 5th histograms in Fig. 3.8(a) demonstrate deceleration results from 300 m/s with increasing deceleration strengths, for which the final velocity is indicated. The delayed arrival of the decelerated molecules is accompanied by a decrease of the number of molecules, due to the corresponding reduction of the the phase-space acceptance volume. The bottom curve shows the deceleration from 290 m/s to 120 m/s, which was done with the coldest valve (∼200 K). Due to clogging of the valve we did not obtain a full range of deceleration strengths for this initial velocity. The last result demonstrates the operation of the 4 meter long

[1] Based on S. C. Mathavan, A. Zapara, Q. Esajas, and S. Hoekstra, *Deceleration of a Supersonic Beam of SrF Molecules to 120 m/s*, ChemPhysChem 2016, 17, 3709-3713.

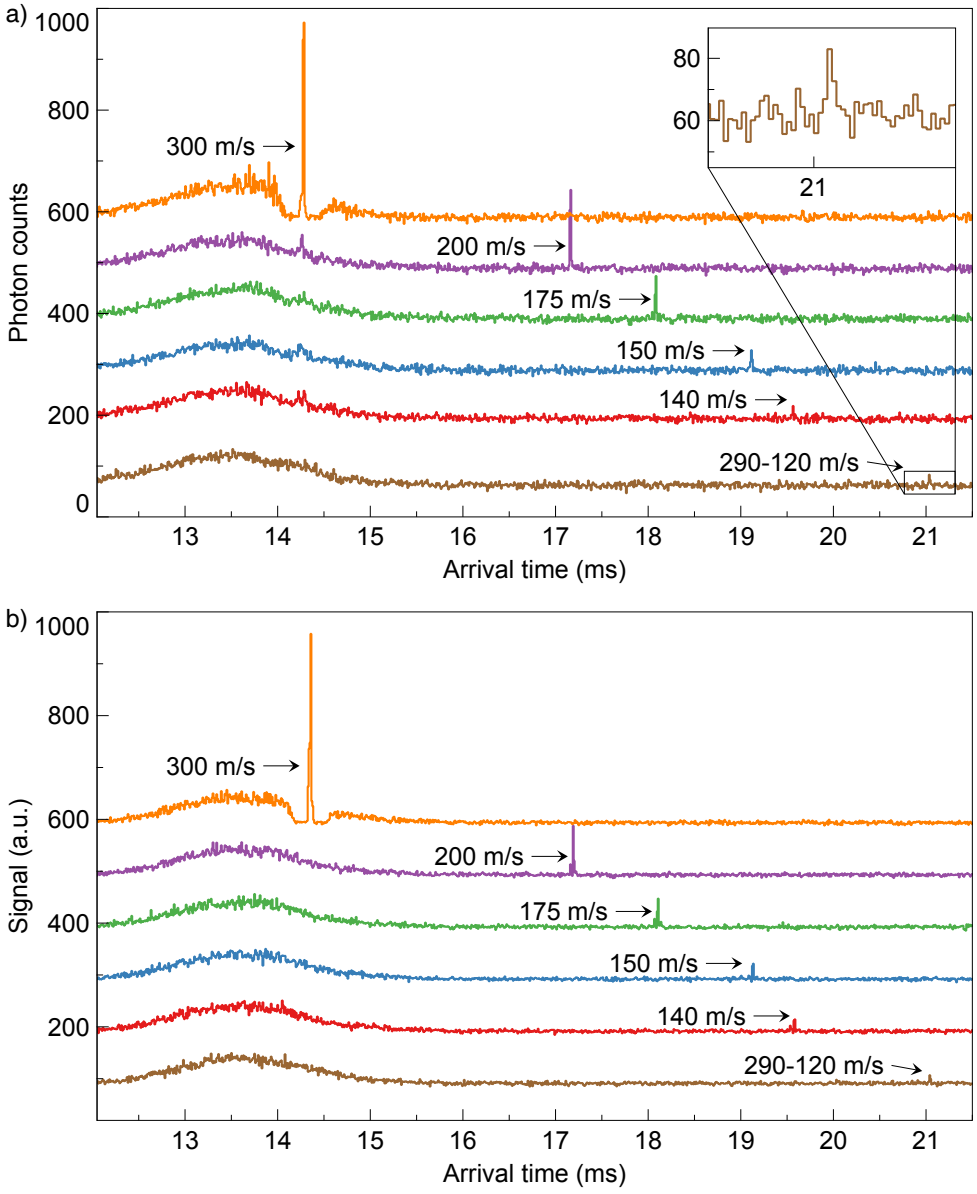

Figure 3.8 | Experimental (a) and simulated (b) time-of-flight profiles (bin size: 10 μs) showing deceleration of SrF molecules in the 4 meter long decelerator from a starting velocity of 300 m/s (top five curves) and 290 m/s (bottom curve). The final velocities are indicated. A vertical offset is added for clarity. The figure is reprinted from Ref. [14].

decelerator with a constant deceleration of 9.6 km/s^2, which for these initial conditions corresponds to the removal of 85% of the initial kinetic energy.

The overall performance of the decelerator can be quantitatively described by the deceleration efficiency, which we define as the fraction of molecules that can be decelerated at a given deceleration strength compared to the total amount of molecules that can be guided at the initial velocity. This number can be found from the experimental results as well as from the trajectory simulations. Since the longitudinal acceptance of the decelerator decreases with increasing deceleration strength [3], the fraction of trapped molecules also decreases. In case of deceleration of SrF molecules from 290 m/s to 120 m/s, the aforementioned efficiency determined from the experimental results is about 6-7%, which under these experimental conditions is in good agreement with the simulations. The demonstrated deceleration efficiency is also consistent with the previous results [8] for the 2 meter long decelerator. We have however identified loss mechanisms under other circumstances, mainly at higher initial velocities, which are in the main scope of the next chapter.

To obtain the number of decelerated molecules from the number of detected photons, we have determined the detection efficiency. We estimate this value to be $(0.25 \pm 0.05)\%$ taking into consideration the following factors: collection solid angle of the fluorescence light, quantum efficiency of the PMT, longitudinal and transverse velocity spread of the beam, average number of scattered photons/molecule (estimated at 3.5) and the transmission of the optics. With this efficiency the total number of molecules per shot reaching the end of the decelerator in the SrF(1,0) state is $(5.6 \pm 1) \times 10^3$. These arrive within a time window of 10 ms around the guided peak. For the measurements with an initial velocity of 300 m/s, the detected signal in a time window of 100 μs around the guided peak corresponds to 440 ± 90 molecules/shot, which decreases to 28 ± 6 molecules/shot in the measurement with the maximum deceleration strength (300−140 m/s). When selecting 290 m/s as the initial velocity, we obtain 230 ± 50 molecules/shot in the guided peak (data not shown) and 16 ± 3 molecules/shot in the decelerated peak with final velocity of 120 m/s.

We would like to point out that the low number of molecules per shot in the deceleration experiments is not caused by the performance of the decelerator but by the performance of the SrF supersonic source. Compared to our source, a previously reported beam of similarly produced YbF molecules [15] is about 1 order of magnitude more intense.

3.2.3. Trajectory simulations

In order to analyze the experimental results, we have performed Monte-Carlo trajectory simulations of the deceleration process, resulting in the simulated time-of-flight profiles that are displayed in Fig. 3.8(b). Care has been taken to ensure that the simulations are numerically stable. The beam conditions of the simulations have been matched to those of the experiment. The trajectory simulations reproduce all essential features of the measured time-of-flight profiles, including the decrease of the guided peaks and the relative intensity of the non-decelerated part. In this case, it is possible to reconstruct the kinematic properties of the molecular beam at any stage of the deceleration. We can derive that the mean longitudinal velocity of the SrF beam after the source chamber is 315 m/s with a FWHM of 40 m/s. We also deduce from the simulations that the final transverse velocity distribution of the decelerated packets of SrF molecules is well described by a Gaussian with a FWHM of 3.3 m/s. The longitudinal velocity spread depends on the deceleration strength and ranges from a FWHM of

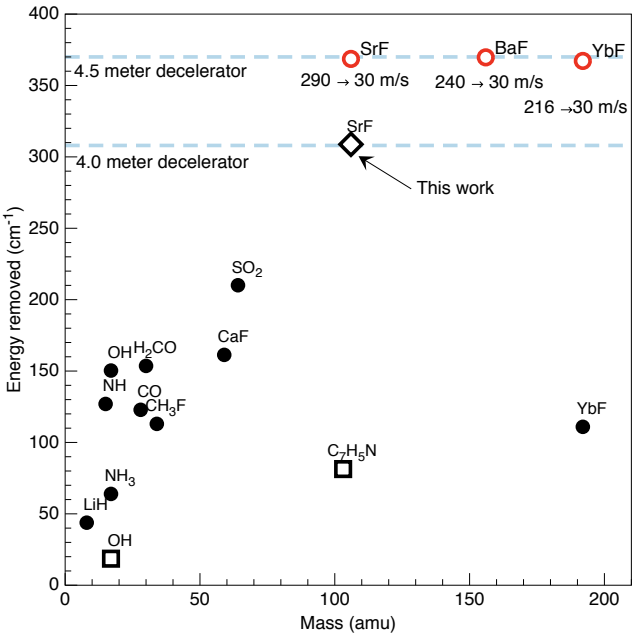

Figure 3.9 | The total kinetic energy removed in the deceleration reported in this work (diamond) compared to previous Stark deceleration experiments with low-field seeking molecules (full circles) and high-field seeking molecules (empty squares). The possible deceleration with a 4.5 m long decelerator is also indicated (red empty circles). The figure is reprinted from Ref. [14].

6 m/s at 300 m/s down to only 1.7 m/s at a forward velocity of 140 m/s. There are some slight but noticeable differences between simulations and experimental results that can be attributed to the systematic effects and mechanisms that are not included in the simulation code, which are: valve temperature stability during the measurements, imperfections of the waveforms, possible nonadiabatic losses or parametric heating mechanisms. However, under given conditions all of them play a minor role for the deceleration efficiency.

3.3. Conclusions

To put the reported results on the 4 meter long deceleration of SrF into perspective, we have plotted in Fig. 3.9 the total amount of kinetic energy removed, together with an analysis of previous Stark deceleration experiments [7, 16–25]. For the vertical energy axis we have chosen units of wavenumber, on the horizontal axis the molecular mass is indicated. As can be expected from the length of our decelerator, the amount of energy removed is larger than any previously reported values, by about a factor 1.5. The longest Stark decelerator operated previously was 2.6 meters long [26].

References

[1] S. Y. T. van de Meerakker, H. L. Bethlem, N. Vanhaecke, and G. Meijer, *Manipulation and Control of Molecular Beams,* Chem. Rev. **112**, 4828 (2012).

[2] P. Cheng, A. Shayesteh, and D. K. Bohme, *Gas-Phase Reactions of Sulfur Hexafluoride with Transition Metal and Main Group Atomic Cations: Room-Temperature Kinetics and Periodicities in Reactivity,* Inorg. Chem. **48**, 1018 (2009).

[3] J. E. van den Berg, *Traveling-wave Stark deceleration of SrF molecules*, Ph.D. thesis, University of Groningen (2015).

[4] S. A. Meek, H. L. Bethlem, H. Conrad, and G. Meijer, *Trapping Molecules on a Chip in Traveling Potential Wells,* Phys. Rev. Lett. **100**, 153003 (2008).

[5] S. A. Meek, H. Conrad, and G. Meijer, *A Stark decelerator on a chip,* New J. Phys. **11**, 055024 (2009).

[6] A. Osterwalder, S. A. Meek, G. Hammer, H. Haak, and G. Meijer, *Deceleration of neutral molecules in macroscopic traveling traps,* Phys. Rev. A **81**, 051401 (2010).

[7] H. L. Bethlem, G. Berden, and G. Meijer, *Decelerating Neutral Dipolar Molecules,* Phys. Rev. Lett. **83**, 1558 (1999).

[8] J. E. van den Berg, S. C. Mathavan, C. Meinema, J. Nauta, T. H. Nijbroek, K. Jungmann, H. L. Bethlem, and S. Hoekstra, *Traveling-wave deceleration of SrF molecules,* J. Mol. Spectrosc. **300**, 22 (2014).

[9] R. Buijs, *Capaciteit bepalen tussen naastliggende electrode,* Internal report (2017).

[10] Keysight, *Impedance Measurement Handbook, 6th edition* (2016).

[11] P. J. Dagdigian, H. W. Cruse, and R. N. Zare, *Radiative lifetimes of the alkaline earth monohalides,* J. Chem. Phys. **60**, 2330 (1974).

[12] J. F. Barry, D. J. McCarron, E. B. Norrgard, M. H. Steinecker, and D. DeMille, *Magneto-optical trapping of a diatomic molecule,* Nature **512**, 286 (2014).

[13] J. H. T. Burke, O. Garcia, K. J. Hughes, B. Livedalen, and C. A. Sackett, *Compact implementation of a scanning transfer cavity lock,* Rev. Sci. Instrum. **76**, 116105 (2005).

[14] S. C. Mathavan, A. Zapara, Q. Esajas, and S. Hoekstra, *Deceleration of a Supersonic Beam of SrF Molecules to 120 m/s,* ChemPhysChem **17**, 3709 (2016).

[15] M. R. Tarbutt, J. J. Hudson, B. E. Sauer, E. A. Hinds, V. A. Ryzhov, V. L. Ryabov, and V. F. Ezhov, *A jet beam source of cold YbF radicals,* J. Phys. B: At. Mol. Opt. Phys. **35**, 5013 (2002).

[16] K. Wohlfart, F. Grätz, F. Filsinger, H. Haak, G. Meijer, and J. Küpper, *Alternating-gradient focusing and deceleration of large molecules,* Phys. Rev. A **77**, 031404 (2008).

[17] K. Wohlfart, F. Filsinger, F. Grätz, J. Küpper, and G. Meijer, *Stark deceleration of OH radicals in low-field-seeking and high-field-seeking quantum states,* Phys. Rev. A **78**, 033421 (2008).

[18] C. Meng, A. P. P. van der Poel, C. Cheng, and H. L. Bethlem, *Femtosecond laser detection of Stark-decelerated and trapped methylfluoride molecules,* Phys. Rev. A **92**, 023404 (2015).

[19] N. E. Bulleid, R. J. Hendricks, E. A. Hinds, S. A. Meek, G. Meijer, A. Osterwalder, and M. R. Tarbutt, *Traveling-wave deceleration of heavy polar molecules in low-field-seeking states,* Phys. Rev. A **86**, 021404 (2012).

[20] O. Bucicov, M. Nowak, S. Jung, G. Meijer, E. Tiemann, and C. Lisdat, *Cold* SO_2 *molecules by Stark deceleration,* Eur. Phys. J. D **46**, 463 (2008).

[21] S. Hoekstra, M. Metsälä, P. C. Zieger, L. Scharfenberg, J. J. Gilijamse, G. Meijer, and S. Y. T. van de Meerakker, *Electrostatic trapping of metastable NH molecules,* Phys. Rev. A **76**, 063408 (2007).

[22] J. J. Gilijamse, S. Hoekstra, S. A. Meek, M. Metsälä, S. Y. T. van de Meerakker, G. Meijer, and G. C. Groenenboom, *The radiative lifetime of metastable CO (*$a^3\Pi$*,* v*=0),* J. Chem. Phys. **127**, 221102 (2007).

[23] T. E. Wall, J. F. Kanem, J. M. Dyne, J. J. Hudson, B. E. Sauer, E. A. Hinds, and M. R. Tarbutt, *Stark deceleration of CaF molecules in strong- and weak-field seeking states,* Phys. Chem. Chem. Phys. **13**, 18991 (2011).

[24] S. Y. T. van de Meerakker, P. H. M. Smeets, N. Vanhaecke, R. T. Jongma, and G. Meijer, *Deceleration and Electrostatic Trapping of OH Radicals,* Phys. Rev. Lett. **94**, 023004 (2005).

[25] E. R. Hudson, C. Ticknor, B. C. Sawyer, C. A. Taatjes, H. J. Lewandowski, J. R. Bochinski, J. L. Bohn, and J. Ye, *Production of cold formaldehyde molecules for study and control of chemical reaction dynamics with hydroxyl radicals,* Phys. Rev. A **73**, 063404 (2006).

[26] L. Scharfenberg, H. Haak, G. Meijer, and S. Y. T. van de Meerakker, *Operation of a Stark decelerator with optimum acceptance,* Phys. Rev. A **79**, 023410 (2009).

4

Operation of a 4.5 meter long decelerator

In this chapter, we show and discuss the experimental results obtained with a 4.5 meter long traveling-wave Stark decelerator. It has always been argued that macroscopic TWSDs are inherently stable [1, 2], i.e. the number of electrically trapped molecules remain constant during the deceleration process. Here, for the first time, we show signatures of molecular number losses inside the decelerator due to nonadiabatic transitions from trappable to non-trappable quantum states. They can be manifested by a noticeable change in the shape of experimental time-of-flight profiles, namely as a dip on top of the signal peaks. Moreover, there is a clear discrepancy between experimental results and simulations with no loss mechanisms included. The losses are most prominent in guiding mode of operation at high frequencies and voltage amplitudes of the waveform. They can be effectively suppressed in deceleration mode, however still remain observable and deteriorate the overall deceleration efficiency. To describe the loss mechanism, we have applied the Landau-Zener model for transitions between low-field seeking (lfs) and high-field seeking (hfs) energy levels in a rotating electric field. In order to quantify loss rates, we have implemented this model in previously developed numerical trajectory simulations, which is shown in the next chapter.

4.1. Experimental results

The apparatus used to collect the following experimental datasets is identical to the one described in the previous chapter, with one difference: the number of

decelerator modules is 9 (the total number of ring electrodes is 3024), making the TWSD 4.536 m long. This seemingly small length addition inevitably leads to an increased capacitive load that has to be driven by the high-voltage electronics. In other words, the HV amplifiers must supply higher currents to maintain the required oscillating voltage. To summarize the experimental protocol, the SrF radicals produced in a supersonic source chamber, enter the TWSD with time-dependent inhomogeneous electric fields, and are detected after leaving the decelerator by collecting the spontaneous emission following excitation by the resonant laser light. The resonance detection method probes SrF molecules in their ground electronic state $X^2\Sigma^+(v{=}0, N{=}1)$.

The first part of this section gives a description of the data collection method and analysis with a focus on the statistics of the registered photons. Then the results in AC guiding mode of operation are shown at a velocity of 345 m/s for different voltage amplitudes. For high voltage amplitudes, the number of molecules leaving the decelerator is found to be smaller than predicted from the trajectory simulations. Finally, we show deceleration results starting from different initial speeds, demonstrating a suppression of molecular number losses depending on the initial guiding speed.

4.1.1. Data analysis summary

We start with a complete overview of the data acquisition (DAQ) system and data analysis toolbox. As was already mentioned, the information about molecular beams at the end of the decelerator can be reconstructed from the LIF signal recorded by a photomultiplier tube (PMT). An 8-channel delay/pulse generator (BNC Model 575) drives the timing sequence for creating the supersonic molecular beam and the HV waveforms. A PMT (Hamamatsu H7422P-40) continuously converts photons falling into its effective area into electrical signals, with a certain efficiency. This quantum efficiency is typically a function of the wavelength, and for this model it is equal to 0.35 at 663 nm. A fluorescence filter (Semrock FF01-661/20-25) in front of the PMT is placed to suppress transmission of photons with different wavelengths. Electrical signals from the PMT pass through a single-pulse discriminator and a logic level converter, and then goes as a TTL pulse to a time-to-digital converter (TDC) Signadyne TDC-H3344. This TDC module records individual time stamps of the input voltage signal with 320 ps temporal resolution. The clocks of the BNC and TDC are synchronized using 10 MHz reference output of the BNC. Thus, two channels of the TDC are used to acquire the time stamps from the pulse generator and from the PMT, which allows to perform on-line signal processing or to save data to the PC using the PCI eXtensions for Instrumentation (PXI) standard. The components of the

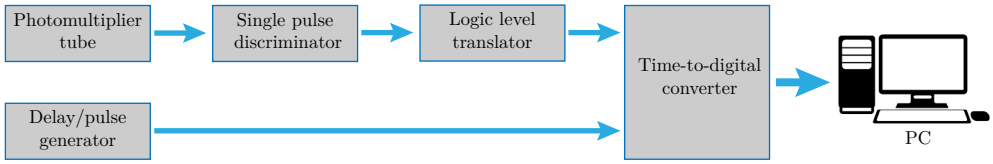

Figure 4.1 | Data flow diagram for generating and saving experimental data as explained in the text.

DAQ system are schematically depicted in Fig. 4.1.

For monitoring the data stream on-line and for saving data into log files, we use a homemade `LabView` software program. For off-line analysis, a `Python`-based analysis toolbox has been developed. The most common way of representing the experimental data is in binned one-dimensional histograms, i.e. when the distribution of photon arrival times is plotted with a certain quantization. The arrival time of every photon is calculated as a time difference between the corresponding time stamp and the preceding trigger time stamp. Comparison of the time stamps is performed by the software.

In Fig. 4.2(a), a typical experimental time-of-flight (TOF) histogram is plotted, showing data obtained with the 4.5 m long decelerator. The histogram is shown over the 13−16 ms time frame with a bin size of 2 μs. The background level is calculated as the average level over the 60−90 ms time window and plotted as the horizontal dashed line. Everything above the background level is considered as a molecular beam signal. At t=13.75 ms, the sharp 20 μs-wide peak corresponds to the molecules falling inside the phase-space acceptance of the decelerator. Broad wings on either sides of the central peak come from the molecules outside the longitudinal but within the transverse phase-space acceptance. The amplitude modulation in the wings is the consequence of the periodic perturbations that molecules experience when they move too fast or too slow compared to the traveling wave. The 60 μs-wide region of interest around the central peak is highlighted by vertical dashed lines, and the signal within this region is used for determining the performance of the apparatus. The annotation for the histogram contains the processed information about the molecular beam signal. Some of the items require an explanation. The total measurement time is given in a regular form and in terms of laser ablation shots. The total number of counts is calculated as the amount of photon counts above the background level in the signal region, while the next two values give the average amount of counts per bin in the signal and background region, respectively. The signal-to-background ratio is defined as the ratio between the two previous values. The peak-to-background is simply the ratio between the maximum of the central peak

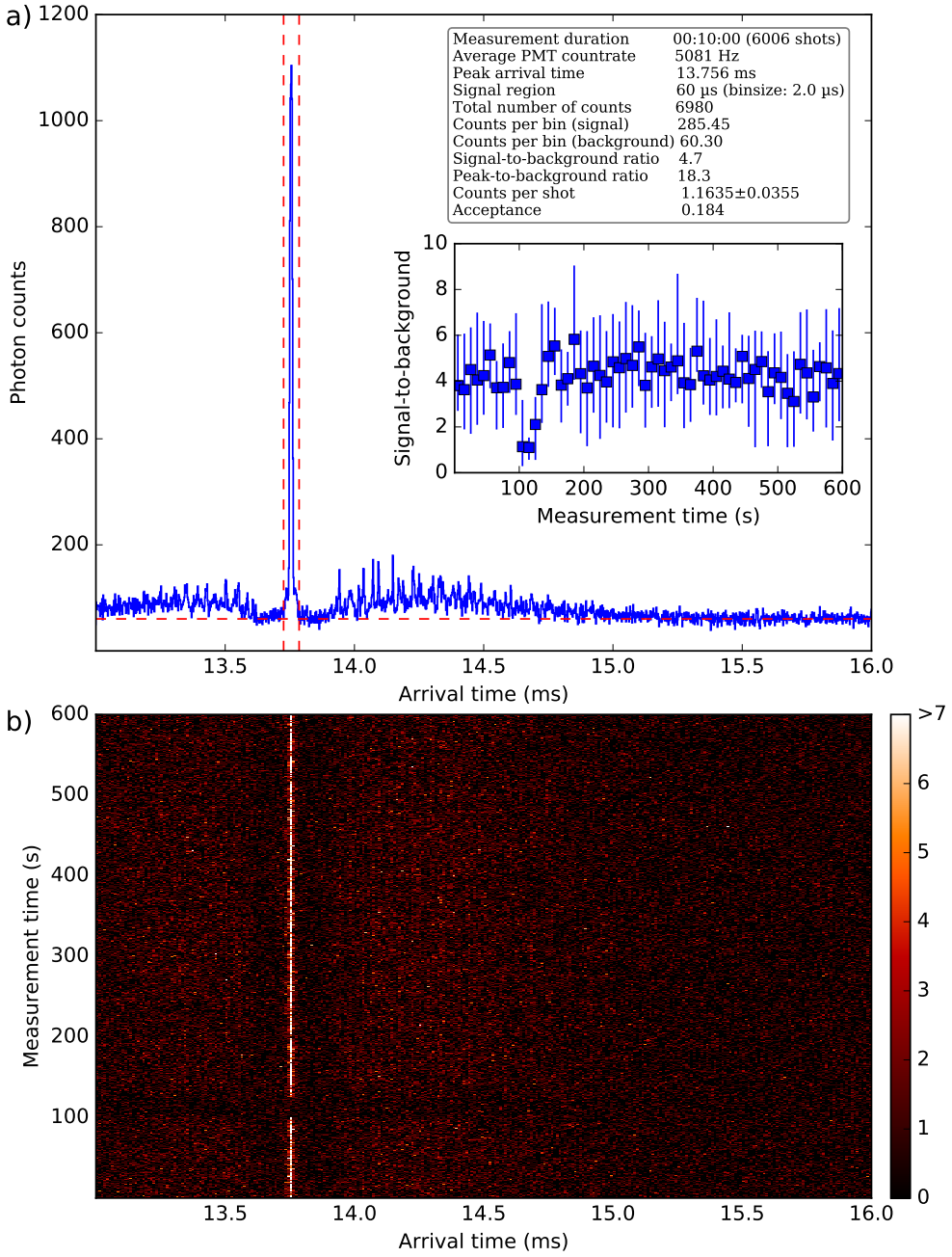

Figure 4.2 | (a) An example of the experimental time-of-flight spectrum with the data analysis outcome in the annotation. The time evolution of the molecular signal is shown in the inset and in the bi-dimensional histogram with a corresponding color coding (b).

and the background level. The penultimate value in the annotation, number of counts per shot, is the most important one since it characterizes the average intensity of the molecular beam. It shows how many extra photons are detected in the region of interest for every ablation laser shot. Finally, the acceptance parameter determines the fraction of molecules in the signal region relative to the total number in the beam. It is noteworthy that some of the parameters, like the peak-to-background ratio, naturally depend on the bin size.

The TOF histogram encompasses information about the properties of the molecular beam averaged over the total measurement time. However, it does not reveal the dynamics of the process. For this purpose, the signal-to-background ratio is plotted versus the measurement time in the inset of Fig. 4.2(a). Every data point on this graph is a 10 s averaged value, and the error bars are used to indicate the minimum and maximum signal-to-background ratios over the corresponding time range. A drop in the signal-to-background ratio down to unity is visible at around 100 s and is attributed to a short failure of the Nd:YAG laser. In a complementary manner, the evolution of molecular beam signal can be visualized as a bi-dimensional histogram with a color mapping. This plot for the aforementioned measurement example is shown in Fig. 4.2(b). The longitudinal axis is conveniently chosen to be the same as in the one-dimensional histogram. The two-dimensional bin size is 10 μs $\times$ 1 s. Therefore, the colormap determines how many photons are detected by the PMT within a 10 μs time window during 1 s (or 10 ablation shots). The sharp stripe of high intensity at t=13.75 ms originates from the detection of molecules in a single potential well and shows a variation of the signal strength as a function of time. To conclude, these evolution graphs are useful in determining the temporal stability of the molecular signal, signal optimization and for systematic error analysis.

Here a more detailed analysis of the photon statistics is given. The number of photon occurrences out of a total of n photons for an ideal source of light (constant amplitude, angular frequency, and phase) exhibits a Poisson distribution, described by the following probability distribution:

$$P_k = \frac{\langle k \rangle^n}{n!} e^{-\langle k \rangle}, \tag{4.1}$$

where $\langle k \rangle$ is the mean photon value over the photon counting time window. In our example case, we can split the photon arrival times into arrays based on the repetition rate (10 Hz). Then every dataset corresponds to an individual ablation laser shot. In Fig. 4.3, the actual distribution of registered photons is shown in the 60 μs-wide signal region (13.72−13.78 ms) and an analogous time window in the background region (60.00−60.06 ms). The time-averaged values μ_{S+B} and μ_B in both regions are shown in the annotation. The dashed lines

are the Poisson fits for the extracted mean values μ_{S+B} and μ_B and the shaded areas show the 95% confidence limits that are equal to $1.96\sigma/\sqrt{n}$, where n is the sample size, or the total number of the ablation shots. The standard deviation σ is defined in a usual way as $\sigma=\sqrt{\sum_{i=1}^{n}(k_i - \langle k\rangle)^2/(n-1)}$. The variance, or the square of the standard deviation, for an ideal Poisson distribution should be equal to its mean value. However, the real photon statistics can deviate from the ideal Poisson law [3]. This deviation can be quantified by Mandel's Q-parameter ($Q=(\sigma^2-\langle k\rangle)/\langle k\rangle$) and corresponds to sub- and super-Poissoninan behavior for $Q<0$ and $Q>0$, respectively. Typically, the detected photons are governed by the super-Poissonian statistics in both regions of interest (see annotation). However, the LIF photons in the signal region exhibit this model more prominently. There are multiple reasons for a departure of the actual photon statistics from the Poisson distribution in our experiment. For example, the temporal variation in the detection laser power can induce the statistics deviation in both regions of interest, while the detection laser frequency fluctuations and the shot-to-shot ablation laser stability leads to the widening of the photon distribution in the signal region only, which is also consistent with our findings. The number of extra photons per shot from the molecular beam can be found as

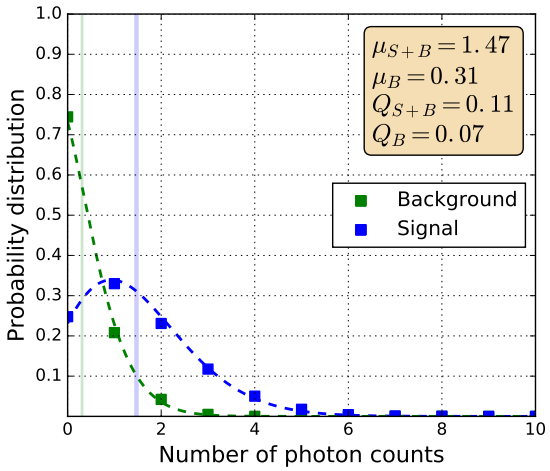

Figure 4.3 | Photon statistics within the signal and background regions demonstrate an almost Poisson distribution (the dashed curves are the Poisson fits with the corresponding mean values). The width of the vertical lines shows 95% confidence intervals around the average number of photons per shot in two regions.

$$\mu_{extra} = (\mu_{S+B} - \mu_B) \pm \sqrt{\frac{\sigma^2_{S+B} + \sigma^2_B}{n}} = \mu_0 \pm \delta\mu, \tag{4.2}$$

and is placed in the annotation for Fig. 4.2. For calculating the statistical error, we assume no correlation between photon statistics in two time windows.

Knowing the total detection efficiency, one can find the actual number of molecules in the moving trap, or in the whole beam. As was already mentioned, the overall detection efficiency η is found to be $(0.25 \pm 0.05)\%$ (see Section 3.2.2). To convert the amount of registered photons into number of molecules, we use the following equation:

$$N = \frac{\mu_0}{\eta_0} \pm \sqrt{(\frac{\mu_0}{\eta_0^2}\delta\eta)^2 + (\frac{1}{\eta_0}\delta\mu)^2}, \tag{4.3}$$

where $\delta\eta$ is the estimated spread in the detection efficiency. As an example, the total number of guided molecules in a time window of 60 μs around the central peak for experiment in Fig. 4.2 is $(4.7 \pm 0.9)\times 10^2$ molecules/shot. It is worth noting that the relative error of this value is larger than the relative error of the number of photons/shot due to the high systematic uncertainty in the detection efficiency.

4.1.2. Observation of losses in guiding mode

We have performed a series of measurements in AC guiding mode of operation scanning various parameters, mainly the applied voltage amplitude and the guiding frequency. Starting with the SrF supersonic beam seeded in Xe at room temperature, molecules enter the 9-module decelerator with a forward velocity centered at around 350 m/s. This velocity can slightly change during the measurement time since the temperature of the supersonic valve is not actively stabilized. An oscillating voltage is applied to the decelerator electrodes in the form of equation (3.3 a), where the voltage amplitude V_0 is scanned in the range of 1.5−4.5 kV with a step of 500 V, and the guiding velocity v_0 is set to 345 m/s. This value turned out to be slightly smaller than the mean velocity of the supersonic beam, which results in a subtle asymmetry of the signal shape at the end of the TWSD, mostly in the wings or transversely accepted part of the beam. Every measurement is 10 minutes long, or 6000 ablation shots. The corresponding experimental TOF histograms are plotted in Fig. 4.4 with a bin size of 1 μs. Only a 60 μs-wide time window around the guided peak arrival time is shown. This time interval corresponds to three electric field minima, since the transit time of one electric trap at the exit of the decelerator is (6 mm)/(345 m/s)$\simeq$17 μs and molecular packets naturally spread in space after

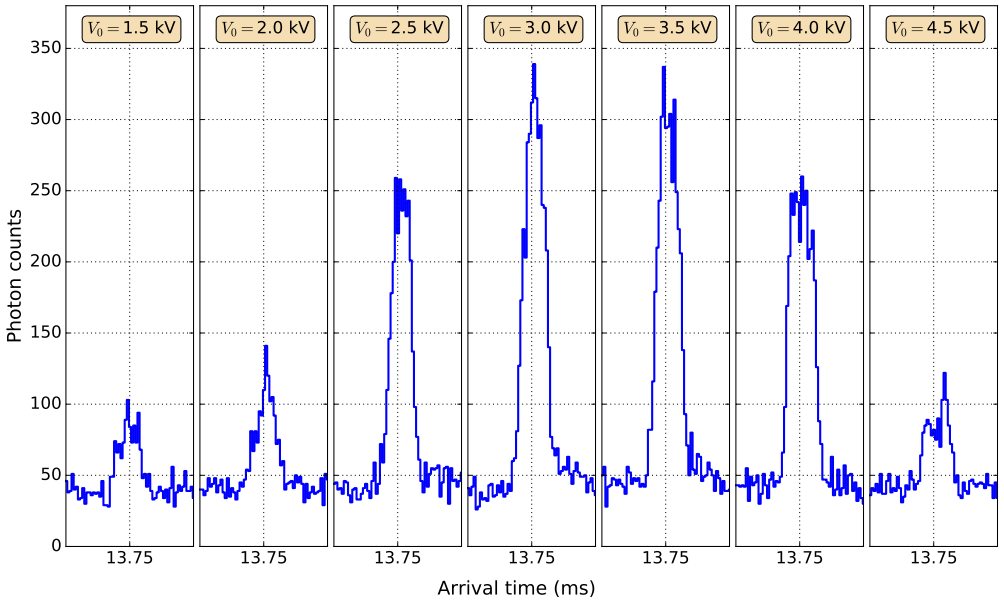

Figure 4.4 | Experimental TOF histograms for guiding in the 4.5 m long decelerator at various voltage amplitudes. The time window for every plot is 13.72−13.78 ms and the bin size is 1 μs. Besides the change in intensity of the signal at a voltage amplitude higher than 3.0 kV, there is also a visible change in the shape of the guided peak.

leaving the decelerator in a field free zone. In practice, for our source conditions, only the central trap is filled with molecules. The applied voltage amplitudes for every measurement are shown at the top of each subplot.

As the voltage amplitude increases, the potential well depth in the longitudinal direction inside the TWSD becomes higher as long as the gradient of the Stark shift for a given quantum state of the molecule is positive. For the detected molecules and the setup geometry, this happens until the applied voltage amplitude is 5.0 kV. However, the experimental results demonstrate an unusual shape of the TOF profile and a reduction of the total number of guided molecules at the highest voltage amplitude applied. This is, for instance, clearly visible when comparing the V_0=3.0 kV and V_0=4.5 kV runs. The lower amount of registered photons in the latter case implies that the number of molecules is reduced during the guiding inside the decelerator due to higher electric field strengths, while the bimodal distribution of the molecules in the TOF histogram (that we have seen repeatedly) indicates that the molecular number loss occurs primarily at the electric trap center location. Moreover, the shape of the histogram in the 4.5 kV run is asymmetric, showing that amount of molecules faster than the synchronous molecule (to the left from the center) is less than amount molecules

slower with respect to the synchronous molecules (to the fight from the center). This voltage- and position-dependent loss mechanism has never been observed in a macroscopic TWSD and its origin is discussed later in this chapter. There we take into account the possibility of a coupling between lfs and hfs quantum states in a rotating external electric field.

4.1.3. Suppression of losses in deceleration mode

In this section, we present the experimental results on the deceleration of SrF supersonic beams in the 4.5 meter long decelerator. The voltage amplitude applied to the electrodes now follows the equation (3.3 b). The initial velocity v_i should be within the forward velocity range of molecules in the supersonic beam, and the deceleration strength a can be set separately. First, we perform deceleration with a room temperature supersonic valve, when the mean forward velocity of the beam is close to 350 m/s. The applied voltage amplitude is 4.5 kV. The corresponding TOF histograms are shown in Fig. 4.5 with a bin size of 2.6 μs. A vertical offset of 100 counts is added between individual histograms for

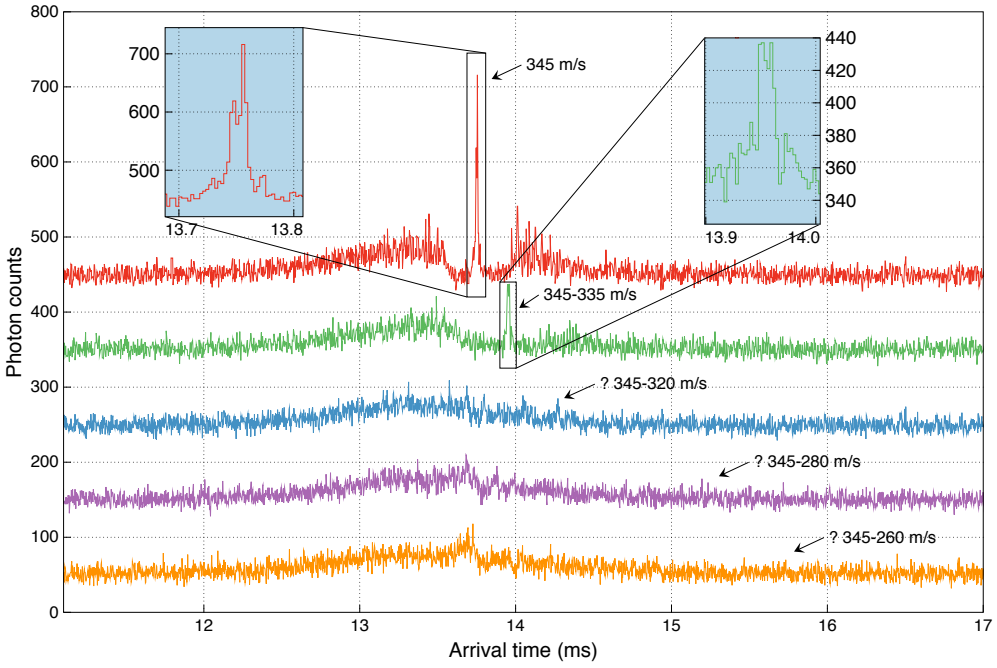

Figure 4.5 | Experimental time-of-flight profiles (bin size: 2.6 μs) of deceleration of SrF molecules in the 4.5 meter long decelerator from a starting velocity of 345 m/s. There is a rapid reduction of signal visible when the deceleration strength increases beyond 1 km/s^2.

clarity. The top curve shows the aforementioned bimodal and asymmetric guided peak, as described in the previous section. The next four curves represent actual deceleration, with the final velocities indicated at expected arrival times of the molecules. These times can be calculated from the simple classical treatment. Since the total length of the flight L_{total} and distances of different sections are known, one can split the total time of flight into three parts:

$$t_{\text{total}} = \frac{L_1}{v_i} + \frac{2L_0}{v_i + v_f} + \frac{L_2}{v_f}. \tag{4.4}$$

Here the first term corresponds to the free flight of molecules from the ablation spot to the entrance of the decelerator (L_1=125 mm), the second one is the L_0-long linear deceleration from velocity v_i to v_f, and the last one is the free flight from the exit of the decelerator to the detection position (L_2=83 mm). Magnified images of the first two histograms show the arrival peaks at the expected times. As one can see, the minimal final velocity of 335 m/s is possible in this setup configuration (the corresponding deceleration strength is 760 m/s^2). No peaks are found in the experiments when the final speed of the traveling wave is below this value.

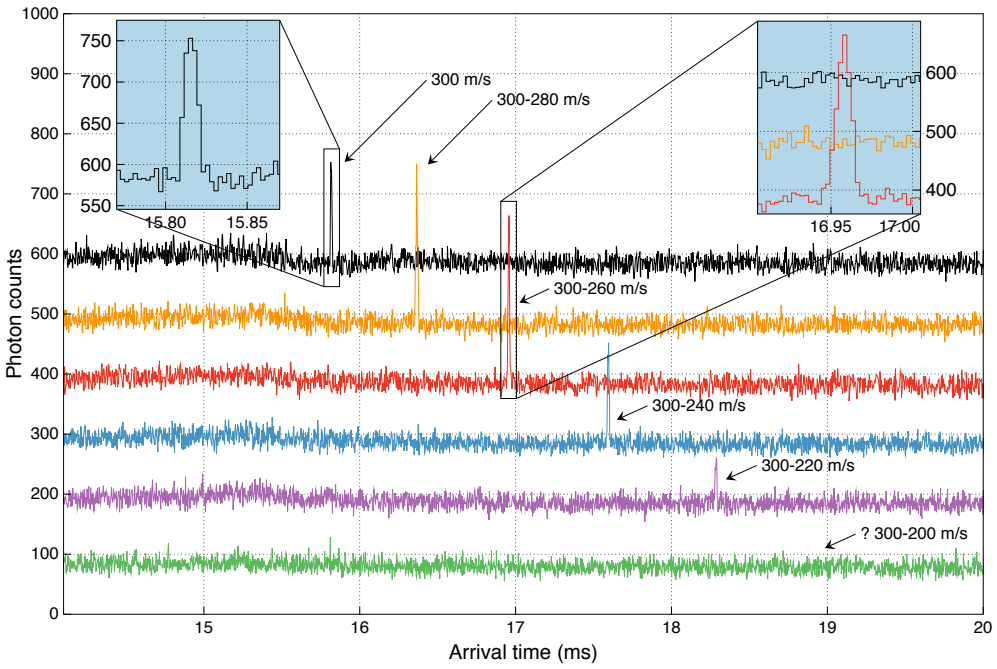

Figure 4.6 | Experimental time-of-flight profiles (bin size: 2.6 μs) of deceleration of SrF molecules in the 4.5 meter long decelerator from a starting velocity of 300 m/s.

Another series of deceleration runs have been performed with lower v_i (310 and 300 m/s) and mean velocities of the molecular beam. The terminal velocity of the molecules from the supersonic source can be shifted towards lower values by reducing the temperature of the carrier gas. In our system it is achieved by cold nitrogen cooling of the General valve (see Section 3.1.1). In Fig. 4.6, one can see the experimental TOF histograms for deceleration of SrF supersonic beam from an initial speed of 300 m/s. In this case, the initial velocity distribution of molecules is centered around 315 m/s with a FWHM value of 40 m/s (temperature of the valve body is reduced to around 200 K). As one can see from the graphs, the lowest final velocity achieved is 220 m/s (the corresponding deceleration strength is 4.6 km/s^2). However, an interesting situation happens at intermediate deceleration strengths, when the molecular signal is higher than in the case of AC guiding. This effect can be more clearly seen in the insets of Fig. 4.6, where magnified images at the location of the peaks are shown for guiding at 300 m/s and for the deceleration to 260 m/s. Another important observation is the shape of the guided peak at 300 m/s, which is not bimodal as in the case of guiding at 345 m/s but rather symmetric, indicating a suppression of the molecule number losses at these experimental conditions.

In order to summarize the experimental findings in the 4.5 meter long TWSD, an overview plot is shown in Fig. 4.7, where the molecular number is plotted

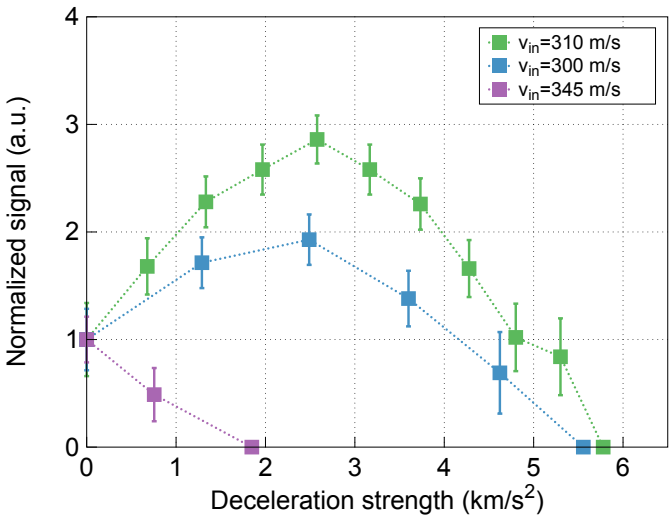

Figure 4.7 | Molecular signal intensity as a function of the deceleration strength for different initial velocities. The signal for every set of measurements is normalized to the corresponding AC guiding signal intensity. Error bars indicate normalized uncertainties on molecular numbers.

versus the deceleration strength $a=(v_i^2-v_f^2)/2L_0$ in units of km/s^2. Here the data is shown for three different initial velocities of the supersonic beam. The purple and the blue traces correspond to the TOF histograms shown in Fig. 4.5 and 4.6, respectively, while the TOF spectra for green data points are not shown. The data for each trace is normalized to the signal intensity in the corresponding AC guiding mode in order to see the relative difference. The dotted lines connect adjacent data points as a rough guide to the eye. The purple dataset shows the aforementioned rapid decrease of the molecular beam signal obtained at a room temperature supersonic source. The other two datasets are obtained when the temperature of the supersonic source is lowered down to 190−200 K. They summarize an unusual outcome, namely that the relative amount of molecules decelerated in the TWSD for certain deceleration strengths is higher than that of the corresponding AC guiding. The maximum gain occurs at a deceleration strength of 2.5 km/s^2, for both cases.

4.2. Discussion

A stable performance of a decelerator of any kind means that the amount of molecules remain constant during the deceleration process. There are, however, different possible loss mechanisms. To the best of our knowledge, four fundamental loss mechanisms relevant for an electric trap exist: collisions between molecules and the background gas, collisions between molecules inside the trap, blackbody radiation, and nonadiabatic transitions to non-trappable quantum states. The first mechanism can be suppressed to negligible levels by evacuating the background gas to an ultra-high vacuum. In our case, the typical pressure in the decelerator vacuum chamber is $\sim 10^{-8}$ mbar. Assuming typical cross sections of few hundreds of Å^2 [4], this could be expected to lead to a negligible loss rate of 10 s^{-1}. Collisions between trapped molecules will only be significant at much higher phase-space densities, while the blackbody radiation effects become important on a ∼1 s time scale [5]. The last mechanism, nonadiabatic transitions between different states, is a pure quantum mechanical effect that depends on the molecular structure and the rate of change of the external field. If the field changes too rapidly, molecules cannot maintain their orientation with respect to the field. Moreover, this rapid change occurs at relatively small field strengths, where rotational sublevels approach degeneracy, and it is more likely that transitions between states can be driven. The description of this mechanism in the context of Stark deceleration is given in the next section.

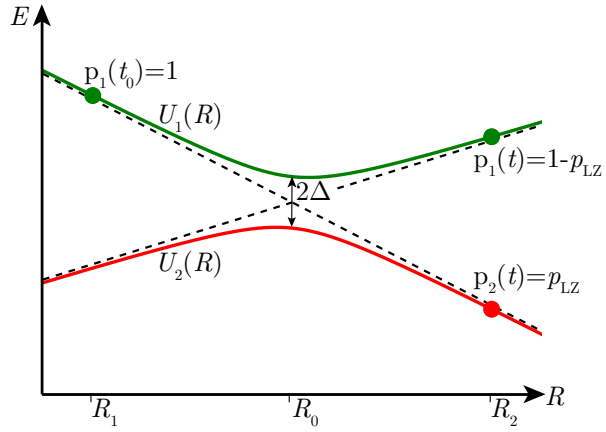

Figure 4.8 | A schematic representation of the nonadiabatic transition in the case of avoided crossing of potential energy curves. The system that starts evolving from the upper adiabatic state (green) during a single sweep of the adiabatic parameter R jumps to the lower state (red) with the Landau-Zener probability p_{LZ} (see text).

4.2.1. Landau-Zener model for nonadiabatic transitions

The concept of adiabaticity plays an important role in many phenomena in natural sciences: physics, chemistry and biology [6]. Generally, if we consider a system characterized by two sets of parameters (adiabatic parameters) and has two eigenstates defined at a fixed value of one set of parameters (adiabatic states), then the dynamics of these parameters determines the evolution of the system as a whole. When they change in time slowly enough so that the system stays in one adiabatic state, then the so-called adiabaticity criterion is met. However, sometimes a rapid change of parameters can lead to a transition between adiabatic states, meaning that adiabaticity breaks down. In other words, the system cannot adapt to a quick change of variables and its state changes accordingly. These transitions between adiabatic states are called nonadiabatic transitions.

The theoretical description of nonadiabatic transitions between potential energy curves is discussed in the pioneering works of Landau [7] and Zener [8] and dates back to 1932. They calculated the transition probability during atomic collisions in the case of quasi-crossing of energy levels using contour integrals and special Weber functions, respectively. In principle, their solution can be applied to a more general class of phenomena, including the dynamics of electric or magnetic dipole moments in the electromagnetic field, and that is why we go through this in some detail.

The idealized one-dimensional problem is schematically depicted in Fig. 4.8.

Here two eigenstates $U_{10}(R)$ and $U_{20}(R)$ cross at a certain distance R_0 and are coupled by operator Δ. The adiabatic parameter R is an internuclear distance during the atomic collision. Then two adiabatic states $U_1(R)$ and $U_2(R)$ are defined as:

$$U_{1,2}(R) = \frac{1}{2}\left(U_{10}(R) + U_{20}(R) \pm \sqrt{(U_{10}(R) - U_{20}(R))^2 + 4\Delta^2}\right) \tag{4.5}$$

and represent hyperbolae having $U_{10}(R)$ and $U_{20}(R)$ as asymptotes. The potential energy curves $U_1(R)$ and $U_2(R)$ come close together (the minimal energy separation is 2Δ at $R{=}R_0$) but never cross, therefore this type of interaction is called an avoided crossing. If the system starts in the state $U_1(R)$ and the parameter R changes in time from R_1 to R_2, then there is a non-zero probability that after crossing the closest approach point the system transition to the state $U_2(R)$. This probability in a single sweep of the adiabatic parameter R is governed by the Landau-Zener formula:

$$p_{\mathrm{LZ}} = \exp\left(-\frac{2\pi}{\hbar}\frac{\Delta^2}{v|F_1 - F_2|}\right), \tag{4.6}$$

where $v{=}\left.\frac{dR}{dt}\right|_{R=R_0}$ and $F_1{-}F_2{=}\left.(\frac{dU_{10}}{dR}{-}\frac{dU_{20}}{dR})\right|_{R=R_0}$ are the relative velocity and the difference of the slopes of the eigenstates at the crossing point, respectively. Thus, the nonadiabatic transition probability in the general case depends on the details of the potential energy curves (energy gap and slope) and the rate of change of adiabatic parameter. Obviously, the faster the adiabatic parameter changes in time, the higher probability that the system jumps to another state. Moreover, the probability that the system remains in the same state is equal to $1{-}p_{\mathrm{LZ}}$.

4.2.2. Majorana effect in a time-dependent electric field

In 1932, Majorana published a paper on the dynamics of the spin-1/2 particle in an external time-dependent magnetic field [9]. It turned out that the state of the particle is defined by the relative orientation of its magnetic moment to the magnetic field, which serves as a quantization axis. Thus, if the field changes rapidly then a nonadiabatic transition between states is possible. These transitions are often called Majorana transitions. This situation is analogous to the problem of orientation of an electric dipole moment in an external electric field. The spin-flip Majorana transitions are therefore akin to the possible transitions between rotational sublevels of the molecules induced by a rapid change of the external electric field.

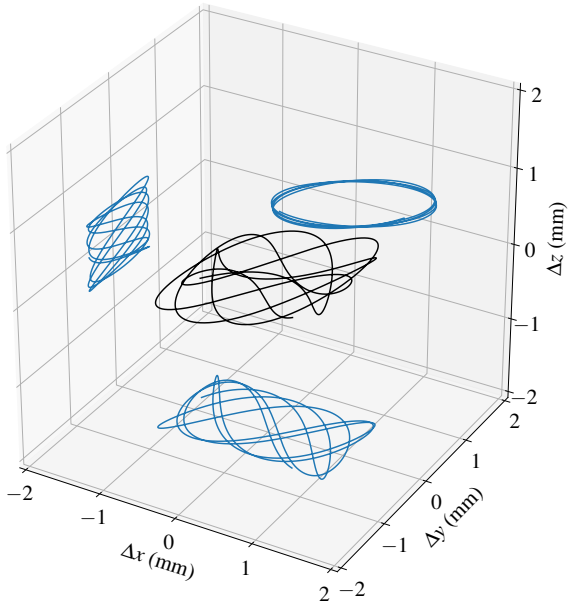

Figure 4.9 | Typical 3-dimensional trajectory (black) and corresponding plane projections (blue) of a molecule inside the TWSD in a moving frame of reference. The origin coincides with the local minimum of electric field. The trajectory is obtained from Monte-Carlo simulations by integrating an equation of motion during 12 ms in AC mode.

For a molecule in a lfs state inside the decelerator, the motion is defined by a force acting due to the gradient of the potential and typically corresponds to oscillations around the electric field minimum, as shown in Fig. 4.9. In a molecule-fixed reference frame, this translates into a time-dependent electric field. Obviously, the rate of change of this field can be important for driving nonadiabatic transitions to other quantum states of the molecule. Moreover, since the molecules oscillate around the local field minima, then the energy spacing Δ between lfs and hfs states becomes small at a location of the closest approach and the probability for jumping to another state increases. Finally, if a molecule in a lfs state transitions to a hfs state, which is not captured by the electric traps of the TWSD, it gets defocused from the molecular beam axis and can be treated as lost. In the remainder of this section, we discuss the physics of this loss mechanism and give an overview of literature on this topic.

Here we give an analysis of nonadiabatic transition probabilities between molecular states due to time-varying electric field of the Stark decelerator. Using

the Hamiltonian of a rigid rotor (see Section 2.1.2) in a rotated coordinate system coupled to the electric field quantization axis one can obtain the following expression for the time-dependent Schrödinger equation:

$$(\hat{H}'+\frac{d\phi}{dt}\hat{N})\,|\alpha'\rangle = i\hbar\frac{d}{dt}\,|\alpha'\rangle\,, \tag{4.7}$$

which describes the time evolution of the state $|\alpha'\rangle$. Here the Hamiltonian of the system in a laboratory frame $\hat{H}$ is related to the Hamiltonian in the rotated frame by $\hat{H}=\hat{D}^{-1}\hat{H}'\hat{D}$, where $\hat{D}=\exp(-\frac{i}{\hbar}\phi\hat{N}_y)$ is the rotation operator. This operator rotates the quantum state by an angle ϕ about y axis to get the state in the new basis: $|\alpha'\rangle=\hat{D}\,|\alpha\rangle$. Since the instantaneous eigenstates of $\hat{H}'$ are rotational levels $|N,M_N\rangle\equiv|m\rangle$, one can obtain the following expression for the Schrödinger equation in a new basis [10]:

$$\sum_m \langle m'|\left(-\frac{i}{\omega_{\rm sep}(t)}\frac{\partial\hat{H}'}{\partial t}+\omega_{\rm rot}(t)\hat{N}_y\right)|m\rangle\, a_m e^{-i\omega_{\rm sep}(t)t} = i\hbar\frac{da_{m'}}{dt}, \tag{4.8}$$

where $\omega_{\rm sep}(t)=\frac{1}{\hbar}(E_m(t)-E_{m'}(t))$ is the angular frequency separation between molecular states, and $\omega_{\rm rot}(t)=\frac{d\phi(t)}{dt}$ is the angular frequency of the electric field rotation. The coefficients a_m are defined as $\langle m|\alpha'\rangle\, e^{\frac{i}{\hbar}E_m t}$ and represent the probability amplitude to find the system in the quantum state $|m\rangle$. Thus, by solving the system of differential equations (4.8) one can find the evolution of the rotational sublevels of the molecule. As one can see, this system consists of two perturbing terms, and we treat them separately in the next paragraphs. Finally, the first-order perturbation theory gives the probability of finding the system in the state $|m'\rangle$ due to the perturbing operator $\hat{V}$ starting in the state $|m\rangle$ to be at most [11]:

$$p^{(1)}=4\frac{|\,\langle m'|\,\hat{V}\,|m\rangle\,|^2}{(\hbar\omega_{mm'})^2}. \tag{4.9}$$

By substituting the terms from equation (4.8), one can get the analogue of the Landau-Zener probability in the context of a time-varying electric field.

The first operator in (4.8) is associated with the changing amplitude of the electric field, since the time dependence of $\hat{H}'$ comes in through the Stark shift term $\hat{H}_{\rm Stark}=-\boldsymbol{d}\cdot\boldsymbol{\mathcal{E}}(t)$ (see Section 2.2.1). The corresponding expectation value can be expressed via spherical harmonics as $(-\frac{id}{\omega_{\rm sep}})\frac{d\mathcal{E}(t)}{dt}\,\langle N',M'_N|\,\sqrt{\frac{4\pi}{3}}\hat{Y}^1_0\,|N,M_N\rangle$, which couple rotational states with the same M_N and different N. And the transition probability between the allowed states has an upper bound:

$$p_{\text{amp}}^{(1)} \leq \left(\frac{4\pi d \mathcal{E}_{max}}{\hbar \omega_{\text{sep}}^2 T} \right)^2, \tag{4.10}$$

where the matrix element is set to unity. We used an approximation for the maximum gradient of electric field strength as $\frac{d\mathcal{E}(t)}{dt}\Big|_{max} \simeq \omega \mathcal{E}_{max} = \frac{2\pi \mathcal{E}_{max}}{T}$. In this case, the electric field changes from 0 to its maximum value $\mathcal{E}_{max}$ during the time $T/2\pi$, where T is the period of sinusoidal oscillations. Using equation (4.10) we can estimate the transition probability for a SrF molecule in its (1,0) rotational state to jump to the (0,0) state inside the decelerator due to the variable electric field strength. We use the maximum electric field amplitude of $\mathcal{E}_{max}$=19 kV/cm (see Section 3.1.2), which is achievable at the voltage amplitude of 5 kV, and the oscillation frequency f=1/T=30 kHz. The smallest angular frequency separation between these levels occurs at zero field and is equal to ω_{sep}=1/$\hbar$($E_{N=1}$−$E_{N=0}$)=2π×15 GHz. Putting all this together, we conclude that the transition probability due to amplitude changes of the electric field $p_{\text{amp}}^{(1)}$ is not larger than about 10^{-12} and can be practically neglected.

The second perturbation term in (4.8) originates from the electric field rotation, leading to reorientation of the electric dipole moment of the molecule with respect to a changing quantization axis. Moreover, the operator $\hat{N}_y$ couples different rotational states M_N within the same N-manifold. This situation is in a marked contrast from transitions induced by time-dependent amplitude $\mathcal{E}(t)$, as now the energy separation between rotational sublevels ω_{sep}=1/$\hbar$(E_{M_N}−$E_{M'_N}$) can become significantly smaller, especially in the region of small electric field strength. As the rotational coupling occurs only between levels with ΔM_N=±1, the corresponding matrix element reduces to $\langle N, M_N \pm 1 |\, \omega_{\text{rot}}(t) \hat{N}_y \,| N, M_N \rangle$, which results in $(\mp \frac{i\hbar\omega_{\text{rot}}(t)}{2}) \sqrt{(N \pm M_N)(N \mp M_N + 1)}$ according to the angular momentum theory [11]. Hence, the upper limit for the transition probability between rotational states M_N and M'_N=M_N±1 induced by the external field rotation is:

$$p_{\text{rot}}^{(1)} \leq \left(\frac{\omega_{\text{rot}}}{\omega_{\text{sep}}} \right)^2 (N \pm M_N)(N \mp M_N + 1). \tag{4.11}$$

It is worth mentioning here that the rotation rate ω_{rot} and the angular frequency separation ω_{sep} are both time-dependent. Finally, we can estimate the probability for a SrF molecule in the trappable lfs (1,0) state to transition to the closest non-trappable hfs (1,1) state as $p_{\text{rot}}^{(1)} \leq 2\omega_{\text{rot}}^2/\omega_{\text{sep}}^2$. The general result also sets an important adiabaticity criterion for the evolution of the molecule in the external rotating electric field as $\omega_{\text{rot}} \ll \omega_{\text{sep}}$. In other words, the molecule remains in the same quantum state if the electric field rotation rate is always much smaller than the energy splitting between the adjacent quantum states.

Having neglected the first perturbation term in equation (4.8), one can also consider the system of differential equations in order to obtain an explicit form for the evolution of population amplitudes $a_{m'}(t)$, and therefore for population probabilities $|a_{m'}(t)|^2$. We can narrow this problem to an effectively two-level system with a time-dependent perturbation. Thus, for molecules in the N=1 rotational manifold, that is used in our experiment, the Schrödinger equation reduces to

$$\begin{cases} \dfrac{da_{M_N=0}}{dt} = i\dfrac{\sqrt{2}\omega_{\text{rot}}}{2}\exp\left(-i\omega_{\text{sep}}t\right)a_{|M_N|=1} \\ \dfrac{da_{|M_N|=1}}{dt} = i\dfrac{\sqrt{2}\omega_{\text{rot}}}{2}\exp\left(i\omega_{\text{sep}}t\right)a_{M_N=0}, \end{cases} \tag{4.12}$$

which can be solved numerically with certain initial conditions, provided ω_{rot} and ω_{sep} are known as functions of time. The form of these equations also provides some insight into the contributions of the physical parameters involved. Hence, there is no significant coupling between the rotational sublevels M_N if the rotation rate is too small, or if the energy separation is too large, confirming the aforementioned adiabaticity criterion.

The behavior of transition probabilities can differ qualitatively depending on the dynamics of coupling parameters [12, 13]. In Fig. 4.10, the time evolution of rotational level populations are shown for various shapes of nonadiabatic perturbation. It is obtained by numerical integration of equations (4.12) in a time window of 200 μs with a step of 0.1 μs. We assume that initially all population is in the (1,0) state ($|a_{M_N=0}(t{=}0)|^2{=}1$). The particular shapes of ω_{sep} and ω_{rot} are modeled by a Gaussian with various parameters, that is $f(t){=}a + b/(\sqrt{2\pi\sigma^2})\exp\left[-(t-t_0)^2/(2\sigma^2)\right]$ with $t_0{=}100$ μs. The actual range of values for ω_{sep} is expected to be in the order of $10^6{-}10^9$ rad/s, while for ω_{rot} it should be around $10^4{-}10^5$ rad/s (see Section 5.2). Three qualitatively different scenarios are visible in Fig. 4.10. If the angular separation frequency and the rotation frequency approach each other (Fig. 4.10(a)) then the population can be redistributed between levels followed by Rabi-type oscillations (Fig. 4.10(d)). The survival probability at the end of the cycle depends on the level of approach between angular frequencies, which agrees with the adiabaticity criterion. If the energy separation between rotational levels is relatively large (Fig. 4.10(b)) but the electric field rotation changes significantly in time, then nonadiabatic jumps can occur between levels, which is seen in (Fig. 4.10(e)). Finally, when the energy spacing between levels is almost constant in time (Fig. 4.10(c)), then the rotational coupling can lead to a pulse-shape transition probability even for relatively large temporal changes of the rotation rate of electric field (Fig. 4.10(f)). In this case, the system is expected to be immune to the nonadiabatic transitions. We have

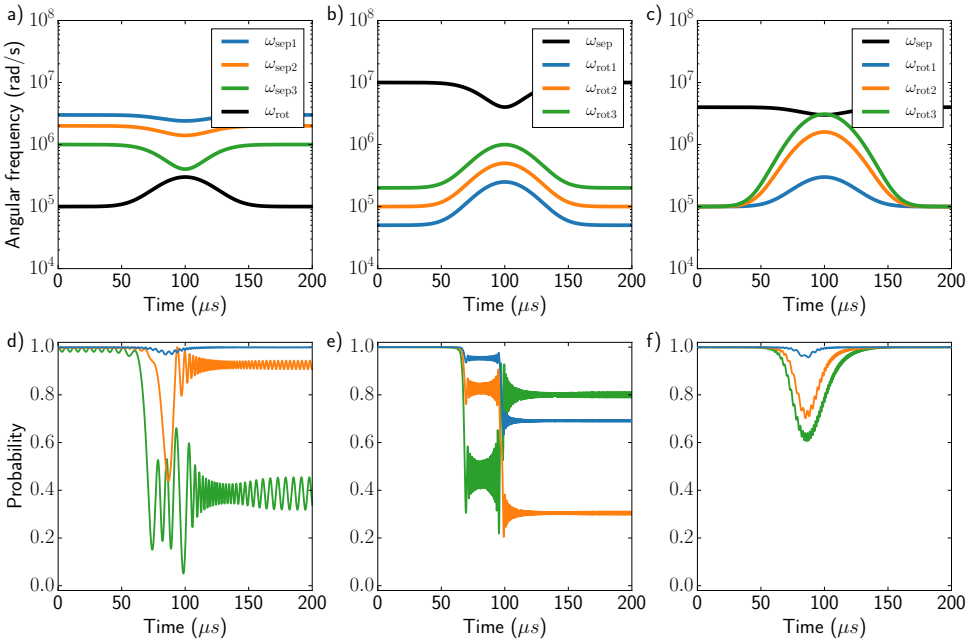

Figure 4.10 | Examples of the time evolution of the angular separation frequency ω_{sep}, the electric field rotation rate ω_{rot} (a,b,c), and the corresponding evolution of rotational level populations (d,e,f). Three various shapes of ω_{sep} are coupled to the same ω_{rot} (black) result in three numerical solutions (d). The same holds for other two cases (b,c) where ω_{sep} (black) is kept the same.

not covered all possible combinations of coupling schemes, but this brief analysis illustrates how sensitive the survival probability is to the particular complex trajectory of a molecule in an alternating external electric field. Examples with realistic values of ω_{sep} and ω_{rot} from the trajectory simulations are provided in Section 5.2.

4.2.3. Observation of Majorana losses in other systems

The stability of the molecular states in relation to the Majorana effect crucially depends on the energy structure of the molecule and the temporal evolution of the external electric field. Here we give a brief overview of the observed nonadiabatic transitions in molecules leading to losses during deceleration processes or to reduced lifetimes in static traps.

In the paper by Kirste *et al.* [14], three isotopologues of ammonia ($^{14}NH_3$, $^{14}ND_3$, and $^{15}ND_3$) have been characterized in an Ioffe-Pritchard electrostatic trap. It was shown that the Majorana-type nonadiabatic transitions can be

a dominant loss channel at temperatures of tens of millikelvins, limiting the trapping lifetime to few seconds. Moreover, molecules in exclusively lfs quantum states (not coupled to hfs states at zero field strength) are rather immune to nonadiabatic transitions. In order to suppress the losses, they used an offset electric field (∼15 kV/cm) at the center of the trap, resulting in lifting the energy spacing between rotational sublevels. The authors also suggest another option to prevent unwanted transitions, namely by orbiting molecules off center in a storage ring.

At certain conditions, nonadiabatic transitions can be observed in a traditional Stark decelerator as shown in Refs. [15, 16]. In these papers, lithium hydride (LiH) and calcium fluoride (CaF) molecules subjected to a rapidly changing electric field of the decelerator experienced switching from lfs to hfs states which depended on the position in the decelerator. In order to reconcile the experimental results with trajectory simulations, they included the possibility that molecules change state as the field switches, following the formalism described in Section 4.2.2. The conclusion from these studies is that decelerated molecules are rather unaffected by the electric-field-dependent losses since they spend more time in a relatively large field region compared to nondecelerated molecules. This is in a natural agreement with the simple adiabaticity condition that relates the rotation speed of the electric field and the energy separation between molecular states.

The guiding stability against nonadiabatic transitions in a chip-based Stark decelerator has been reported in Meek *et al.* [17]. There, two isotopologues of carbon monoxide (^{12}CO and ^{13}CO) in the metastable $a^3\Pi_1$ (v=0) state were guided on top of an array of microstructured electrodes, forming a traveling-wave decelerator for lfs states. It was shown that ^{12}CO is more affected by the losses due to the Majorana-type transitions compared to ^{13}CO since they have different structures of energy levels. Interestingly, applying a constant magnetic field during the guiding suppresses the nonadiabatic transition for the most abundant CO isotopologue, while for ^{13}CO it is enhanced. The harmonic distortion of the applied sinusoidal waveforms can also induce the nonadiabatic transitions, since the large jittering of the position of the trap effectively increases the region of a small electric field strength, where the losses are most prominent.

Finally, the control of the Majorana-type transitions in a dual magnetic and electric quadrupole trap is shown for doubly dipolar hydroxyl radicals (OH) [18]. The unwanted losses can occur in a quantum state exhibiting competition between electric and magnetic fields for alignment of the molecule. The spin-flip losses can be effectively suppressed by a factor of 100 by applying an external bias field (∼200 G). It can be achieved because the offset field reduces the region in space where transitions can exist, which is also confirmed by incorporating the Landau-Zener formula in the simulations.

All these examples of system-specific losses show the fundamental nature of the nonadiabatic mechanism of switching between trappable and non-trappable quantum states. Is it believed that such losses are ubiquitous in all ongoing experiments with cold molecules. As the matter of fact, they can be practically neglected under certain experimental conditions, but sometimes play an important role in observable dynamics of molecular beams or trapped clouds. Control of the loss rates (suppression or enhancement) can also be achieved, but it strongly depends on the molecule in question and properties of the apparatus.

4.2.4. Harmonic analysis of the high-voltage waveforms

As was mentioned in Section 3.1.2, the HV amplifiers cannot always deliver the required alternating voltage, especially when they are connected to the complex equivalent circuitry of the TWSD. Motivated by the effect of waveform fidelity observed in Ref. [17], we quantify the rate of this deterioration, which can be manifested by a total harmonic distortion of amplified waveforms. We also

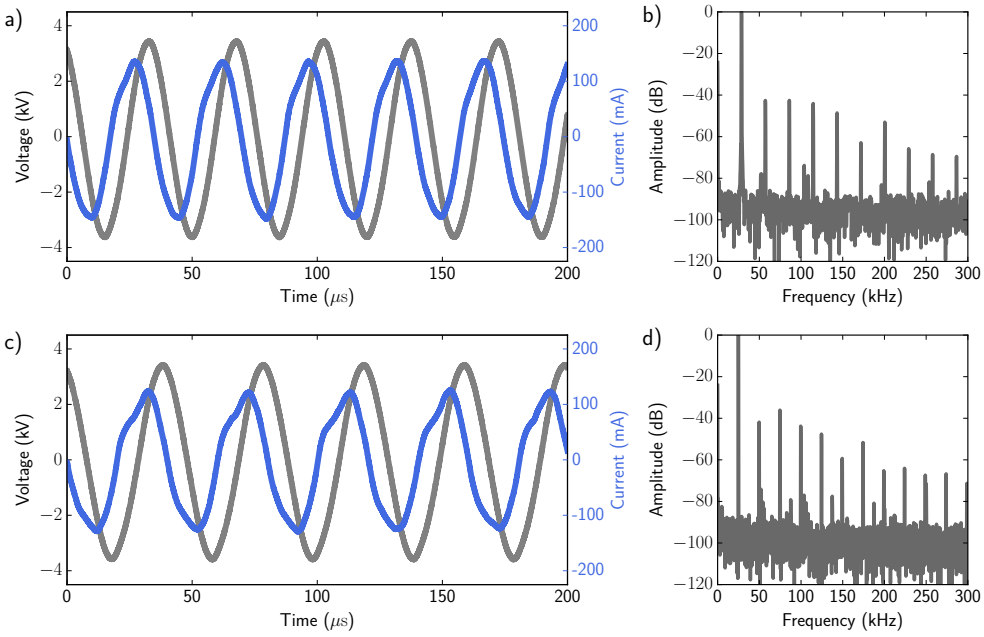

Figure 4.11 | Voltage and current monitor outputs obtained for the AC guiding sinusoidal waveform at the guiding speed of 345 m/s (a) and 300 m/s (c). The voltage amplitude is 3.25 kV. Corresponding power spectra from the fast Fourier transforms show the fundamental frequencies at 28.75 kHz and 25.0 kHz in (b) and (d), respectively.

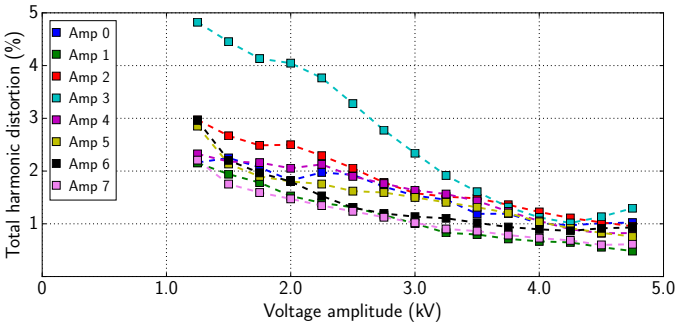

Figure 4.12 | Total harmonic distortion (THD) of the waveforms as a function of voltage amplitude obtained at the guiding velocity of 345 m/s. The input waveforms have been predistorted to minimize the THD values at high voltage amplitudes.

performed an analysis of the waveforms after the amplifiers in both time and frequency domains.

In order to analyze the amplified waveforms, we can record the actual applied signal with the aid of a high-voltage probe which has a certain voltage attenuation or directly from the voltage monitor output. Two methods give an almost identical result, but for practical reasons it is easier to use the latter. The current monitor output provides a voltage signal that is proportional to the current (the proportionality coefficient is 50 mA/V). An example of two output waveforms from one of the amplifiers at different guiding velocities is shown in gray in Fig. 4.11(a,c) in the range of 0.2 ms. The actual current needed to supply the amplified signal is phase-shifted with respect to the voltage and also shown in blue. The frequency domain analysis is performed using a fast Fourier transform (FFT) algorithm. For that purpose, we have recorded 1 ms-long signal at the sampling frequency of 1.6 MHz. The real part of the FFT normalized to the fundamental harmonic in the logarithmic scale is depicted in Fig. 4.11(b,d). To reduce the spectral leakage we selected the Blackman window function. The resulting plots show the fundamental frequency f_0 (the highest peak) as well as higher order harmonics. It can be used to characterize the "purity" of the output signal. In order to quantify this value, we use the coefficient of total harmonic distortion (THD), which is defined as follows:

$$\mathrm{THD} = \frac{\sqrt{\sum_{n=2}^{N} V_n^2}}{V_1}, \tag{4.13}$$

where V_n is the root-mean-square amplitude of the n-th harmonic, and N is related to the bandwidth of the recorded signal. In Fig. 4.12, we show the THD

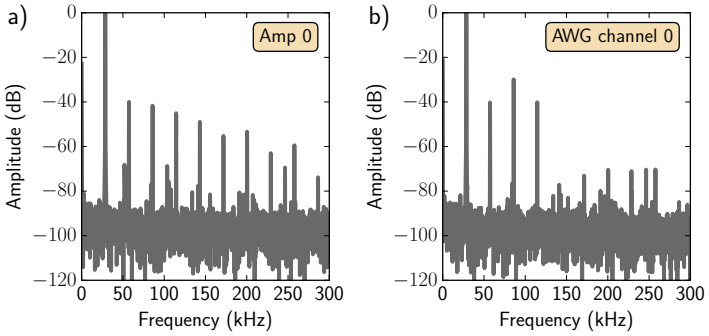

Figure 4.13 | Power spectrum of the amplified (a) and original (b) waveforms for one of the channels. The voltage amplitude is 3.25 kV and the guiding speed is 345 m/s. Starting from the 4-th harmonic the distortions in the amplified signal are visible.

percent values of all HV amplifiers for a number of voltage amplitudes, taking into account first 10 harmonics from the FFT output (the bandwidth is 300 kHz). The same result is expected if one fits the waveforms to a Fourier series with a number of harmonic contributions, i.e. $f(t)=\frac{1}{2}V_0+\sum_{n=1}^{N} V_n \sin(2\pi f_0 nt+\phi_n)$. As one can see, the coefficients of THD stay below 2% for the highest values of the voltage amplitude, that are the most relevant for guiding and deceleration of molecules. The output of Amplifier 3 appears to be less "pure" at relatively small values of the voltage amplitude, which can be caused by different response characteristics of this amplifier in the relevant regime. Similar results are obtained for different fundamental frequencies that correspond to different guiding velocities.

To summarize, the spectral analysis of the waveforms showed a subtle extra distortion of the amplified waveform compared to the input signal. This can be seen from the FFT of the original signal sent to the amplifiers (see Fig. 4.13). It is worth mentioning that we have predistorted the input waveforms from the AWG in order to minimize THD of the applied sinusoidal waves at high voltage amplitudes. This results in the average THD which is less than 2% for all amplifiers in the relevant range of voltage amplitudes and velocities. The waveform fidelity is considered to be satisfactory and comparable with the reported values in Ref. [17] and in the recent studies on HV electronics for TWSD [19]. It is unlikely that this small amount of residual distortions can drive molecular number losses at high voltage amplitudes. However, for a complete understanding of the effect of the waveform parameters, one would also have to include into consideration the relative phase of the higher order harmonics.

4.3. Conclusions

In this chapter, we reported the experimental results on guiding and deceleration of SrF molecules in the world's longest traveling-wave Stark decelerator with a total length of 4.5 meters. It provides a sufficient stopping distance for a beam of heavy molecules to be slowed down for subsequent measurements. We demonstrated the operation of this apparatus at the limits of its specifications. The findings reveal a loss mechanism which has not been observed before in a macroscopic TWSD. The loss is most pronounced at high velocities of moving electric traps and large voltage amplitudes.

In order to qualitatively explain the experimental results, we developed a model to capture the internal state dynamics of a molecule in a rotating electric field. Within this formalism, we derived an adiabaticity criterion, which can be used to predict the evolution of the internal state population. It states that if the effective rotation rate of the external electric field is larger than the energy separation between trappable and any non-trappable quantum states, the probability of a nonadiabatic transition between these states is possible. Inclusion of this model in the numerical trajectory simulations is further discussed in the following chapter.

References

[1] A. Osterwalder, S. A. Meek, G. Hammer, H. Haak, and G. Meijer, *Deceleration of neutral molecules in macroscopic traveling traps,* Phys. Rev. A **81**, 051401 (2010).

[2] J. E. van den Berg, S. C. Mathavan, C. Meinema, J. Nauta, T. H. Nijbroek, K. Jungmann, H. L. Bethlem, and S. Hoekstra, *Traveling-wave deceleration of SrF molecules,* J. Mol. Spectrosc. **300**, 22 (2014).

[3] R. J. Cook, *Photon statistics in resonance fluorescence from laser deflection of an atomic beam,* Opt. Commun. **35**, 347 (1980).

[4] J. J. Gilijamse, S. Hoekstra, S. Y. T. van de Meerakker, G. C. Groenenboom, and G. Meijer, *Near-Threshold Inelastic Collisions Using Molecular Beams with a Tunable Velocity,* Science **313**, 1617 (2006).

[5] S. Hoekstra, J. J. Gilijamse, B. Sartakov, N. Vanhaecke, L. Scharfenberg, S. Y. T. van de Meerakker, and G. Meijer, *Optical Pumping of Trapped Neutral Molecules by Blackbody Radiation,* Phys. Rev. Lett. **98**, 133001 (2007).

[6] H. Nakamura, *Nonadiabatic Transition: Concepts, Basic Theories and Applications* (World Scientific, 2002).

[7] L. Landau, *On the theory of transfer of energy at collisions ii,* Phys. Z. Sowjetunion **2**, 46 (1932).

[8] C. Zener, *Non-adiabatic crossing of energy levels,* Proceedings of the Royal Society of London A: Mathematical, Physical and Engineering Sciences **137**, 696 (1932).

[9] E. Majorana, *Atomi orientati in campo magnetico variabile,* Nuovo Cimento **9**, 43 (1932).

[10] T. E. Wall, *Guiding and decelerating cold, heavy, polar molecules*, Ph.D. thesis, University of London (2010).

[11] L. D. Landau and E. M. Lifshitz, *Quantum Mechanics Non-Relativistic Theory, Third Edition: Volume 3*, 3rd ed. (Butterworth-Heinemann, 1981).

[12] P. R. Berman, L. Yan, K.-H. Chiam, and R. Sung, *Nonadiabatic transitions in a two-level quantum system: Pulse-shape dependence of the transition probability for a two-level atom driven by a pulsed radiation field,* Phys. Rev. A **57**, 79 (1998).

[13] R. K. Malla and M. E. Raikh, *Landau-Zener transition in a two-level system coupled to a single highly excited oscillator,* Phys. Rev. B **97**, 035428 (2018).

[14] M. Kirste, B. G. Sartakov, M. Schnell, and G. Meijer, *Nonadiabatic transitions in electrostatically trapped ammonia molecules,* Phys. Rev. A **79**, 051401 (2009).

[15] S. K. Tokunaga, J. M. Dyne, E. A. Hinds, and M. R. Tarbutt, *Stark deceleration of lithium hydride molecules,* New J. Phys. **11**, 055038 (2009).

[16] T. E. Wall, S. K. Tokunaga, E. A. Hinds, and M. R. Tarbutt, *Nonadiabatic transitions in a Stark decelerator,* Phys. Rev. A **81**, 033414 (2010).

[17] S. A. Meek, G. Santambrogio, B. G. Sartakov, H. Conrad, and G. Meijer, *Suppression of nonadiabatic losses of molecules from chip-based microtraps,* Phys. Rev. A **83**, 033413 (2011).

[18] D. Reens, H. Wu, T. Langen, and J. Ye, *Controlling spin flips of molecules in an electromagnetic trap,* Phys. Rev. A **96**, 063420 (2017).

[19] Y. Shyur, N. J. Fitch, J. A. Bossert, T. Brown, and H. J. Lewandowski, *A high-voltage amplifier for traveling-wave Stark deceleration,* Rev. Sci. Instrum. **89**, 084705 (2018).

5

Numerical trajectory simulations

Computer simulations of real-world systems often help to understand properties of systems and predict an outcome when there is a lack of experimental data. A trust of the simulation greatly depends on the validity of the mathematical model that reflects the system in question. In the following chapter, we describe the Monte-Carlo trajectory simulations of particles with an electric dipole moment in an external inhomogeneous electric field, which corresponds to a motion of SrF molecules inside a traveling-wave Stark decelerator. The efficacy of the model is tested by comparing the simulation outcomes with the high-resolution experimental data. The implementation of nonadiabatic transitions is also discussed in the context of molecular number losses reported in the previous chapter.

5.1. Computational details

In order to model the dynamics of molecular beams inside our apparatus, we have performed full three-dimensional Monte-Carlo trajectory simulations. This procedure allows to compare the experimental results with the numerical calculations, whilst the matching level can be used for verification of the chosen model. Based on the numerical results, we can not only produce "expected" experimental datasets but also reconstruct a number of properties of the molecules at any moment in time. All numerical results are shown for the N=1 rotational level in the electronic ground state of SrF, unless specified otherwise.

5.1.1. Initial conditions and numerical integration

The simulation starts by initializing the phase-space distribution of particles at the source. In our case, we randomly sample the initial phase-space coordinates (3 coordinates and 3 velocity components) using pseudo-random computer generators. The initial instant t=0 is chosen when the synchronous particle is in the plane of the skimmer orifice (see Section 3.1.1). Although the electric field distribution and molecular beam properties are cylindrically symmetric, we use the Cartesian coordinate system throughout the simulations. Thus, the z-axis coincides with the main propagation axis of the molecules, whilst the x-axis points straight up and the y-axis points to the right when looking along the z-axis. All velocity components and the longitudinal position spread follow a normal distribution, and the transverse position distribution is a truncated Gaussian function to accommodate the skimmer geometry. In Fig. 5.1, the initial phase-space coordinates (dots) and one-dimensional histograms of various parameters (dashed lines) are shown for the room-temperature supersonic source.

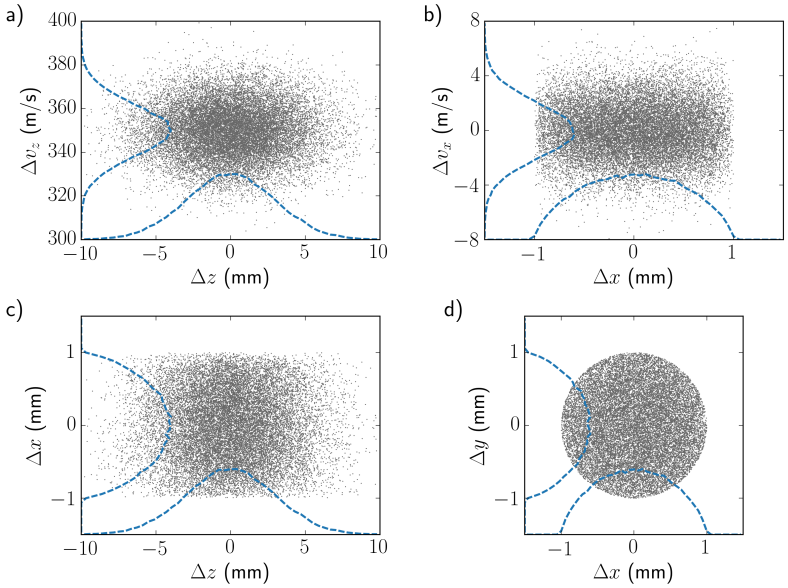

Figure 5.1 | Initial phase-space distribution that corresponds to the room-temperature supersonic beam: forward velocity vs longitudinal position (a), transverse velocity vs transverse position (b), transverse position vs longitudinal position (c), and two transverse position components (d). Each point in the scatter represents one particle. The forward position distribution and all velocity components distributions are modeled by a Gaussian law, whilst the transverse position distribution is a truncated Gaussian. Dashed lines represent projections of the corresponding parameters.

In this case, the mean forward velocity (350 m/s) and all other parameters are selected to fit the experimental dataset in DC guiding mode of operation (see Section 3.1.2). For simulating the molecular beam at lower source temperatures, the mean forward velocity can be changed accordingly, but its FWHM value remains the same, that is around 5% of the mean velocity.

In the following, we give a brief overview of the numerical implementation of an electric dipole moment inside an inhomogeneous electric field and the actual trajectory calculation. The electric potential inside the decelerator is computed using the finite-element package `COMSOL` and is fit using a set of cubic splines. It allows an interpolation of the electric field $\boldsymbol{\mathcal{E}}$ to be obtained as well as the Stark potential $E(\mathcal{E})$ for a given molecular state at any location and moment in time. Finally, the Stark force can be found by taking the negative gradient of the potential (see Section 2.2.1) as $\boldsymbol{F}=-\boldsymbol{\nabla}E(\mathcal{E})=-\frac{dE(\mathcal{E})}{d\mathcal{E}}\boldsymbol{\nabla}\mathcal{E}$. Obviously, it always points towards the local minimum of the electric field. The expression for the Stark energy $E(\mathcal{E})$ is approximated by the 12-th order Taylor expansion of the respective Stark shift obtained with the `PGopher`. For the sake of simplicity, we have set the hyperfine structure constant and the spin-rotation coupling constant to zero, reducing the number of rotational sublevels for a state with a given N to $(N+1)$ (see Fig. 2.4(a)). If the force is known, then the system of equations of motion can be written down for the i-th component of velocity and acceleration:

$$\begin{cases} \dfrac{dx_i}{dt} = v_i \\ \dfrac{d^2x_i}{dt^2} = -\dfrac{1}{m}\dfrac{dE(\mathcal{E})}{d\mathcal{E}}\dfrac{d\mathcal{E}}{dx_i}, \end{cases} \tag{5.1}$$

where m is the mass of the particle. Taking into account the initial conditions, a numerical integration of equations (5.1) takes place using the 5-th order Runge-Kutta method with a fixed time step of 1 μs, which has been optimized to ensure a numerical stability of the results. The `Odeint C++` library has been used for numerical integration routines. More computational details of the simulation package can be found elsewhere [1].

With the aid of the trajectory simulation code, we retrieve various properties of individual particles or of a whole ensemble at any time stamp of integration. Some of these graphs are shown in the remainder of this section and illustrate an ideal propagation of the molecular beam in the decelerator. The time evolution of parameters related to Majorana-type transitions is presented in Section 5.2.

5.1.2. Phase-space acceptance

The concept of phase-stability is crucial for a good understanding of the dynamics of molecular beams inside the decelerator [2]. It explains why only molecules

within a certain range of positions and velocities can be effectively manipulated by external electric forces. When calculated in a traditional Monte-Carlo approach, the phase-space acceptance can be used to quantitatively characterize the phase-space stability. Here we present the numerical results on the longitudinal, transverse and overall phase-space acceptance of the decelerator. Coupling effects between axial and transverse motion are also discussed in the relevant subsection. The phase-space evolution in the co-moving frame of reference for the actual initial conditions is shown in the end.

Longitudinal acceptance

The simplest assessment of the decelerator performance is to calculate its one-dimensional (1D) longitudinal phase-space acceptance. This quantity is defined as the volume in phase space which corresponds to the longitudinally accepted part of the molecular beam. We completely ignore the transverse motion of particles by assigning null values for transverse positions and velocities. Hence, the following calculations give the first order approximation of the total performance of the apparatus.

The 1D longitudinal acceptance is calculated using a Monte-Carlo algorithm. For this, we take uniform random distributions for both the initial molecular positions and their velocities in a range that is larger than the size of the separatrices − imaginary boundaries between stable and unstable motion. Their shapes depend on the voltage amplitude, deceleration strength and a particular shape of the molecular Stark shift. The molecules inside the separatrix remain trapped and can be decelerated. The phase stable area is calculated as a fraction of accepted molecules[1] of the total number at the beginning:

$$A = A_0 \times \frac{N_{\text{accepted}}}{N_{\text{total}}}, \tag{5.2}$$

where A_0 is the total area in phase space ($A_0 = \int\int dz dv_z$). An example of the phase-space distribution at the source is visualized in Fig. 5.2(a). Here, green points represent particles inside the phase stable area (accepted particles) for the case of AC guiding at a voltage amplitude of 5 kV, and blue points represents particles outside this area. The total phase space area A_0 is 112 mm(m/s). The 1D longitudinal separatrix is also drawn as a green curve for the sake of completeness. Numerically, it is obtained as the phase-space trajectory of the particle, that is captured by the central trap of the decelerator and has the largest relative velocity.

[1] We consider a particle to be accepted by the central electric trap if it lies within ±3 mm in the axial direction with respect to the synchronous particle, as follows from the electrode geometry.

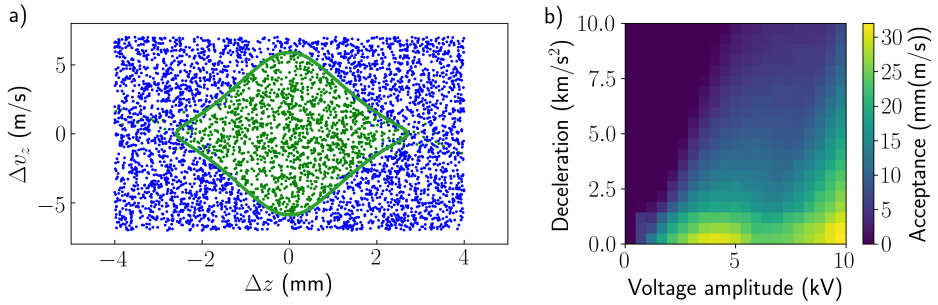

Figure 5.2 | An illustration of the Monte-Carlo numerical integration algorithm used for calculating 1D longitudinal acceptance of the decelerator (a). Green and blue dots represent accepted and non-accepted particles, respectively. The corresponding separatrix is shown as a green curve. The 1D longitudinal acceptance for a range of voltage amplitudes and decelerations (b) in the first order approximation indicate phase stable regions.

In order to assess the 1D longitudinal acceptance under different conditions, we have performed similar numerical simulations for a range of voltage amplitude and deceleration strengths. The overview graph is shown in Fig. 5.2(b). Now and hereafter we scan the applied voltage amplitude (deceleration) in a range of 0−10 kV (0−10 km/s^2) with a step size of 0.5 kV (0.5 km/s^2). As can be seen, the longitudinal acceptance depends on both parameters. For any fixed voltage amplitude, the acceptance decreases with increasing the deceleration, which reflects the lower depth of the potential well. The optimum acceptance is achieved for AC guiding mode of operation at voltage amplitudes of ∼4.5 kV and ∼10 kV. However, as we will see below, the second plateau of high phase-space acceptance is transversely unstable.

Transverse acceptance

Here we show the numerical results regarding transverse acceptance of the decelerator for a range of parameters. Since the transverse confinement depends on the longitudinal position, we also have to take into account the axial motion of particles, making our calculations effectively two-dimensional (2D).

The transverse phase-space acceptance is calculated in the same manner as the longitudinal acceptance. We randomly and uniformly distribute initial positions and velocities in a four-dimensional phase-space volume of A_0=4032 mm^2(m/s)^2 (A_0=$\int\int\int\int dz dx dv_z dv_x$). Then we calculate the total transverse acceptance of the decelerator as the fraction of molecules that end up within a cylinder 2 mm in radius at t=10 ms. The results are shown as a density plot in Fig. 5.3(a) for the same scan of deceleration strengths and voltage amplitudes as in Fig. 5.2(b). Now the situation is markedly different: the total transverse acceptance is nearly

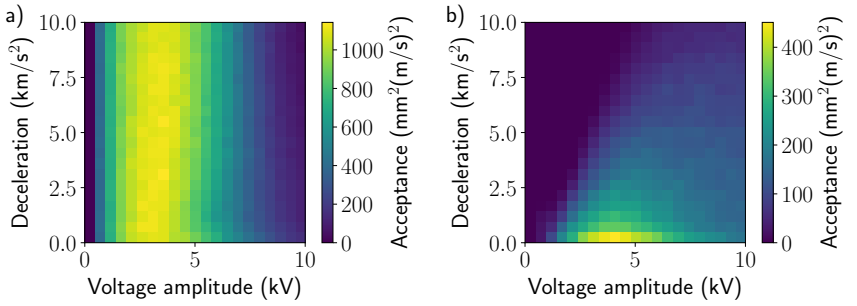

Figure 5.3 | The total 2D transverse acceptance for a range of voltage amplitudes and decelerations (a). The 2D transverse acceptance of the longitudinally accepted particles only (b).

constant as a function of the deceleration and is maximized at a voltage amplitude of ∼3.5 kV. It reflects the almost constant time-averaged transverse potential that molecules experience throughout the decelerator regardless of the velocity of the moving electric field.

The next step is to simulate the transverse acceptance of the longitudinally accepted part of the beam. For this, we select only particles that appear to be within a central moving trap at t=10 ms. The corresponding density plot is shown in Fig. 5.3(b). Now the optimum performance is also achieved at a voltage amplitude of ∼3.5 kV and drops off with increasing deceleration strength. It is noteworthy that coupling of the longitudinal and transverse motion is possible in this 2D numerical calculation. This effect is discussed in more detail in the remainder of this subsection.

Overall phase-space acceptance

The overall phase-space acceptance of the decelerator cannot be obtained as a product of the longitudinal and transverse acceptances [3]. It is rather a complex volume in a six-dimensional phase space which covers the stability regions. To address the question of the total acceptance, we present a full three-dimensional (3D) Monte-Carlo calculation of molecular trajectories in the decelerator, which is the most realistic model of our TWSD.

The initial uniform position and velocity distribution encompasses a six-dimensional phase-space volume of A_0=403200 mm^3(m/s)^3. Then we treat particles within a central trap as being accepted. In Fig. 5.4(a), we show the longitudinal distribution of the transversely accepted part of the beam (transversely non-accepted particles were rejected from the calculations). The 1D longitudinal separatrix is superimposed on the particle distribution. The empty phase-space region close to the separatrix ("halo") implies a coupling

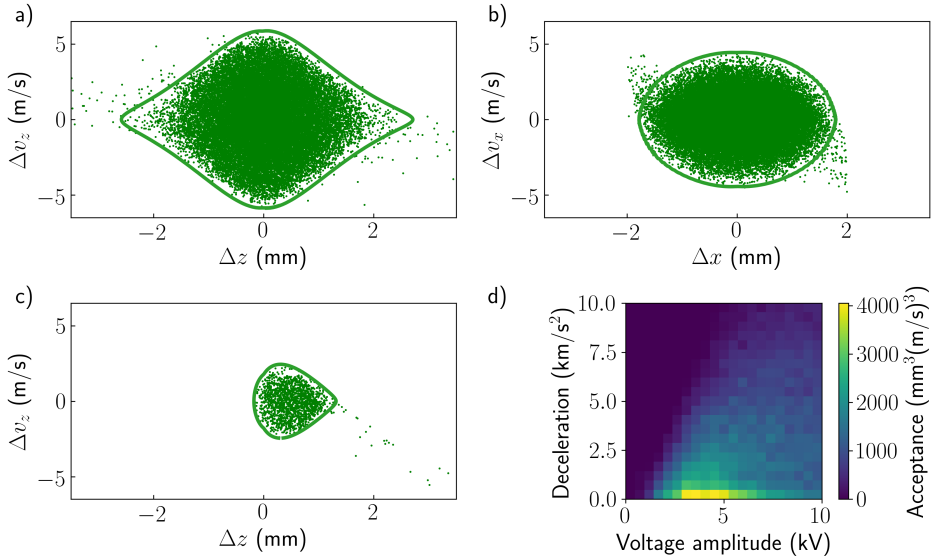

Figure 5.4 | Longitudinal (a) and transverse (b) phase-space distribution of particles in the full 3D trajectory simulations in AC guiding mode. Longitudinal phase-space distribution in deceleration mode (c). The total 3D transverse acceptance for a range of voltage amplitudes and decelerations (d).

effect between longitudinal and transverse oscillations. This reduction of the phase space stable area can be understood from the parametric loss mechanism which occurs whenever the times for longitudinal and transverse revolutions in phase space become very similar (or a multiple of each other). This effect has also been seen in a traditional Stark decelerator [4]. An analogous feature is visible for the transverse phase-space distribution in Fig. 5.4(b), where the 1D transverse separatrix is shown as a green curve. The superiority of the traveling-wave Stark decelerator over the switching-type decelerator is in a high overall acceptance of the former one. Generally, this acceptance does not depend on the final velocity, whilst in a traditional Stark decelerator, transverse defocusing of the beam significantly hinders the performance once very low final velocities ($\sim$50 m/s) are required. To demonstrate this high acceptance of the TWSD, we show the longitudinal phase-space distribution of particles for the case of constant deceleration at 8 km/s^2 (Fig. 5.4(c)). Here the corresponding 1D separatrix is also plotted.

Finally, the total 3D phase-space acceptance is shown for a range of experimental parameters in Fig. 5.4(d). It demonstrates a similar pattern as the 2D transverse acceptance shown above, and yields the maximum phase-space

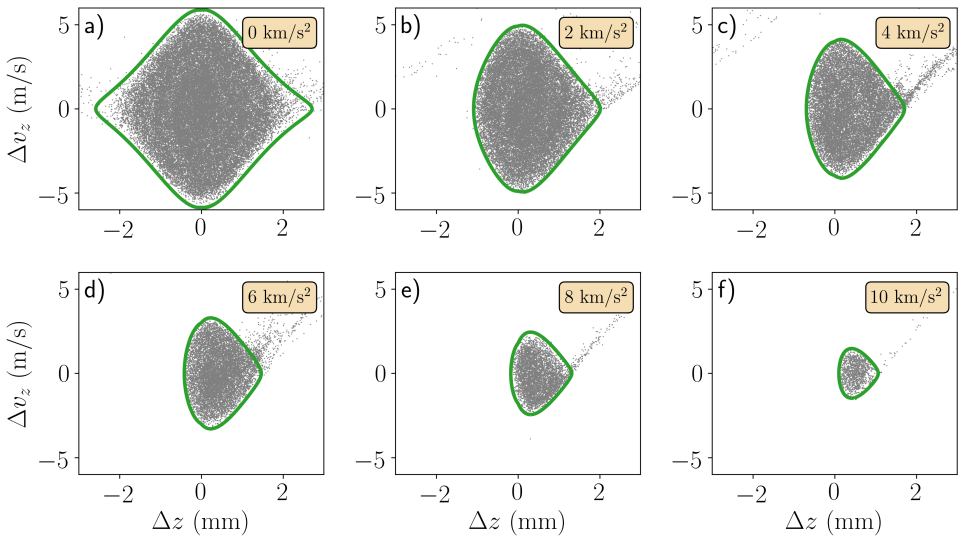

Figure 5.5 | Simulated longitudinal phase-space distribution of molecules at the exit of the decelerator for a range of deceleration strengths with a step of 2 km/s^2. Corresponding separatrices are shown as solid curves.

acceptance of ∼4000 mm^3(m/s)^3 occurring at voltage amplitudes in a range of 3.0−5.0 kV in AC guiding mode of operation. In deceleration mode, the total phase-space acceptance decreases with increasing deceleration, and is about 500 mm^3(m/s)^3 for a deceleration of 8 km/s^2 and a voltage amplitude of 5.0 kV. This value is in a good agreement within a statistical scatter with the previously known values [5].

Phase-space evolution with realistic initial conditions

Here we present the resulting phase-space evolution of molecules in the co-moving frame of reference for a number of deceleration strengths. Initial conditions used for these calculations are shown in Fig. 5.1. In Fig. 5.5, we illustrate the distribution of molecules in the longitudinal phase space (relative velocity vs relative position). Panels of the figure show the reduction of the phase-space acceptance with increasing deceleration strength, which is in agreement with the previous simulations of the phase-space parameters in our decelerator [5]. The corresponding 1D separatrices are also shown as green solid curves. The molecules that initially fall outside separatrices cannot be captured by moving electric traps. These molecules typically move away from the central trap in the co-moving frame, and some of them are still visible in the figure. The capture velocity of the trap can also be easily found from the separatrices. Hence, in the case of a

relatively modest deceleration of 2 km/s^2 (Fig. 5.5(b)), the capture velocity is around 5 m/s and the corresponding trap depth (T=$mv^2/2k_B$) is ∼160 mK. In the case of the strongest simulated deceleration strength of 10 km/s^2 (Fig. 5.5(f)), the capture velocity is 1.5 m/s resulting in a ∼15 mK deep trap. If the moving electric trap comes to rest in the laboratory frame, then the trap depth describes the energy regime of the molecules after the decelerator. Therefore, in this manner, relatively fast molecules originating from a supersonic source can be

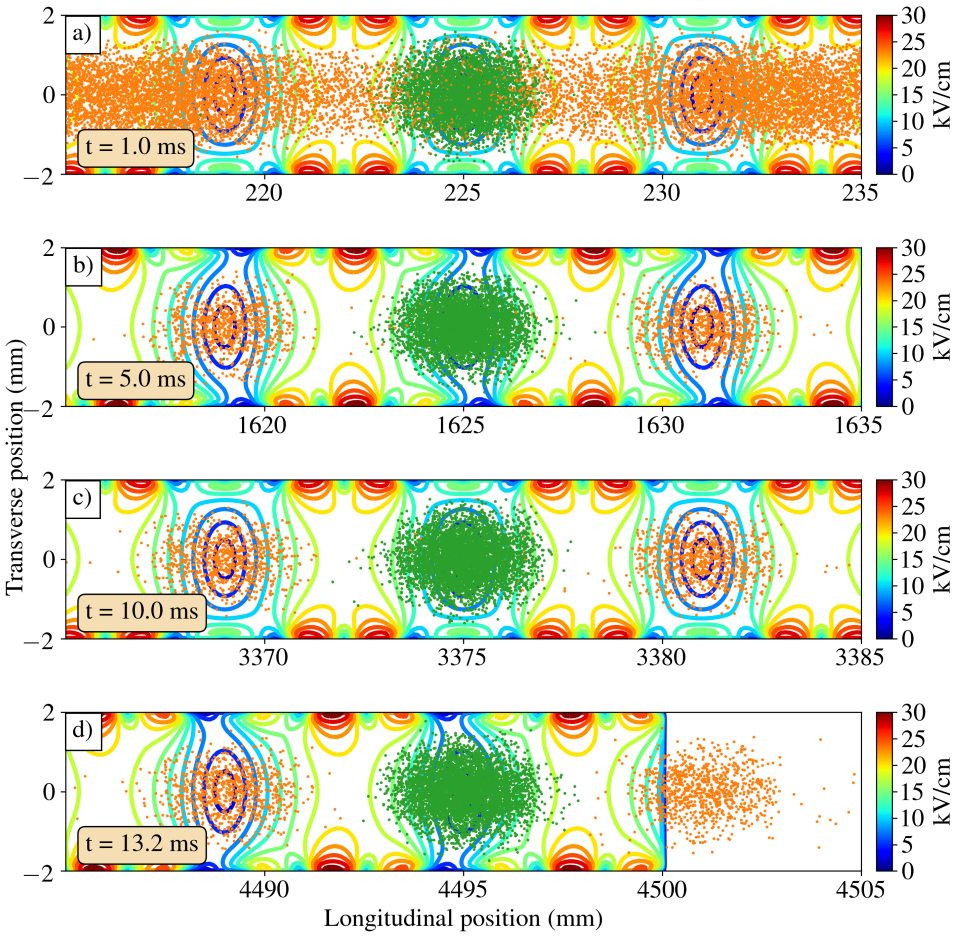

Figure 5.6 | Distribution of molecules (colored dots) inside the electric field of the decelerator (contour lines) in the lab frame of reference in AC guiding mode for four moments in time: few hundred μs after applying the HV waveform (a), when the molecules travel through the decelerator (b,c), and when the molecules start leaving the decelerator (d). Green dots represent molecules that fall within the central trap phase-space acceptance, orange dots are all the rest.

converted into slow in the laboratory frame, to which temperatures of few tens of mK can be attributed.

5.1.3. Phase-space evolution in the laboratory frame

Since the phase-space parameters of molecules can be recorded at any moment in time, the position or velocity distribution can be easily illustrated in the co-moving frame (as shown above) or in the laboratory frame. It is also instructive to see the time evolution of particles in the latter case. An example is shown in Fig. 5.6, where the laboratory frame scatter plot of molecules is superimposed on the electric field distribution inside the decelerator in AC guiding mode at V_a=5.0 kV for four different time stamps (in the legends). Every panel shows a 20 mm-long region around the trap center. The field contour lines are plotted in the same manner as in Fig. 3.2(b,c), but the electrodes are omitted. The molecules that match the trapping condition at the exit of the decelerator are colored green, the other ones are colored orange. In Fig. 5.6(a), the particle distribution is shown at the beginning of the decelerator. Obviously, molecules that are captured by the central electric trap are already located there, whilst other molecules that have another set of phase-space coordinates experience a transverse confinement. In panels (b-c), the situation is markedly different: by this time, the spatial separation of bunches of molecules is visible. Moreover,

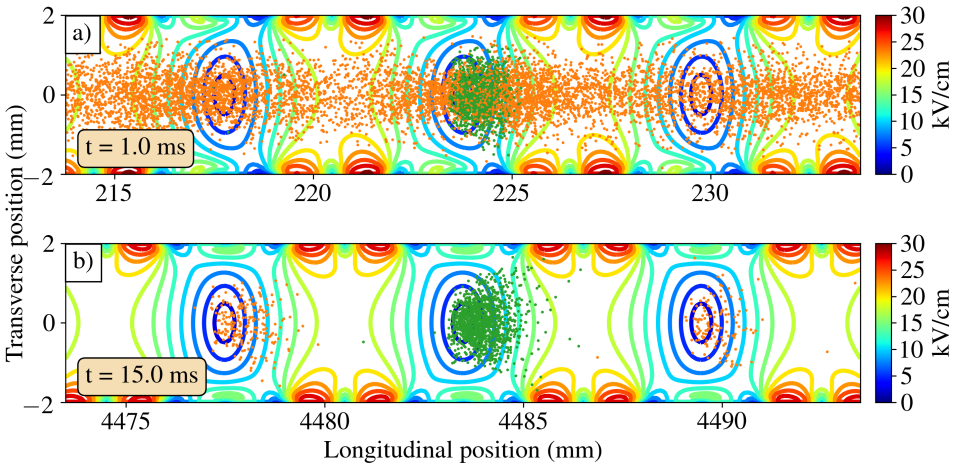

Figure 5.7 | Distribution of molecules (colored dots) inside the electric field of the decelerator (contour lines) in the lab frame of reference in deceleration mode for two moments of time: few hundred μs after applying the HV waveform (a) and when the molecules start leaving the decelerator (b). The color code is the same as in Fig. 5.6.

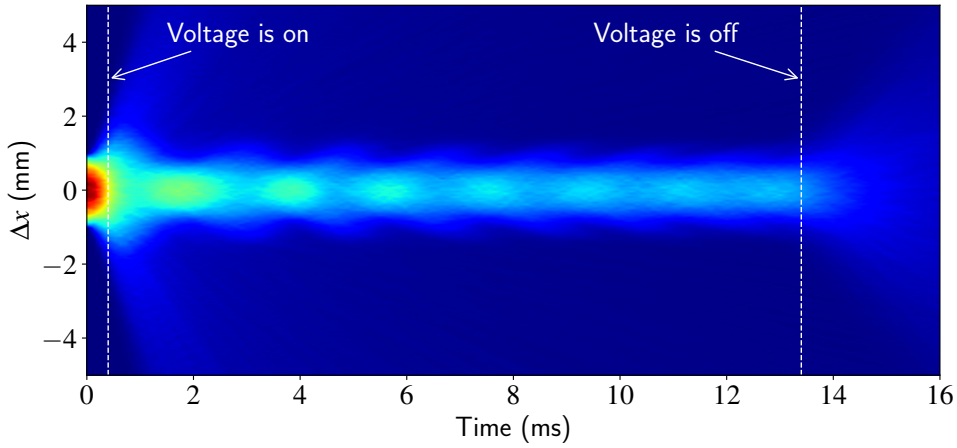

Figure 5.8 | Simulated transverse distribution of the whole molecular ensemble as a function of time in AC guiding mode. The actual experimental timings of the high voltage application are shown by the dashed lines.

some of them occupy the adjacent minima of the electric field. Other molecules, which move too fast or too slow with respect to the synchronous one, are located outside the plot boundaries. In our code, the electric field is calculated throughout the decelerator length until the moment when the center of the trap reaches the decelerator exit (4500 mm). It can be clearly seen in Fig. 5.6(d), where the front part of the beam propagates in a field-free zone, whilst some molecules remain trapped.

A similar phase-space evolution can also be shown for deceleration mode of operation. Two panels of Fig. 5.7 illustrate the particle distribution at the beginning and at the end of the deceleration process, respectively. The deceleration strength is set to 6 km/s^2. The fraction of molecules falling inside the decelerator phase-space acceptance is considerably smaller than that in AC guiding mode. Furthermore, in Fig. 5.7(b) the spatial distribution of molecules inside the moving electric trap changes significantly: they are displaced towards the propagation direction as the result of a pseudo-force exerted on molecules in a non-inertial frame of reference. The occupation of adjacent potential wells is also shifted and proportionally smaller.

In order to assess the transverse confinement of the molecules throughout the decelerator, we have simulated their transverse position distribution as a function of time. First, we perform this numerical calculation without any selection criteria for rejecting particles. The result for AC guiding mode of operation is shown as a density graph in Fig. 5.8. The guiding velocity is 345 m/s, and

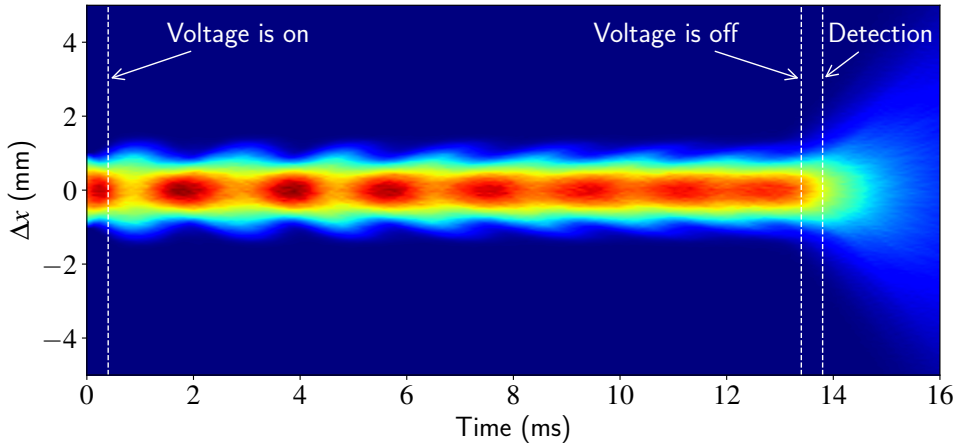

Figure 5.9 | Simulated transverse distribution of the transversely accepted part of the molecular beam as a function of time in AC guiding mode. The actual experimental timings of the high voltage application and the detection of molecules in the central peak are shown by the dashed lines.

the voltage amplitude is 4.5 kV, which matches the experimental conditions in Fig. 4.5. The color code describes the density from low (blue) to high (red). The application of high-voltage waveforms is highlighted by dashed lines and corresponds to the moments when the synchronous molecule passes the first/last ring of the decelerator. The density plot reveals a fast drop of the molecular density at the very beginning of the decelerator, since a substantial part of molecules does not fall within the transverse acceptance of the decelerator (they have too large position and/or velocity in the transverse direction). After leaving the electric field region, the molecular density falls off for the second time as the molecules propagate in a free flight mode.

As we are more interested in molecules that are transversely confined during the guiding process, we show the previous simulation with only this class of particles displayed. The result is depicted in Fig. 5.9. As predicted from Fig. 5.4(b), during the flight through the decelerator molecules remain guided within ∼1.5 mm from the symmetry axis. Nevertheless, the density distribution reveals interesting features of the molecular ensemble, which are also visible in the previous figure but now are more pronounced. Firstly, there is a density modulation at the very beginning of the guiding process, which is attributed to the transverse focusing of the beam. The second important observation is a fast drop of the density in a field-free zone after the decelerator. By the time the synchronous molecule and most of the molecules in the central trap reach the

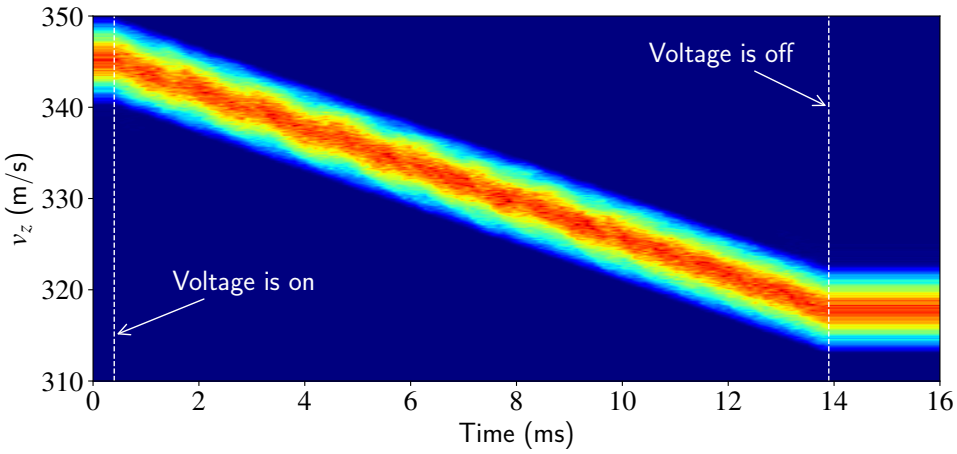

Figure 5.10 | Simulated forward velocity distribution of the molecular ensemble as a function of time in deceleration mode. The actual experimental timings of the high voltage application are shown by the dashed lines.

detection laser beam (also shown by a dashed line), the density falls off by 10% and leads to the lower detection efficiency due to the smaller overlap with the laser beam. Therefore, if the final beam velocity is not zero, it is important to detect slow molecules as close as possible to the decelerator exit. Alternatively, one could perform transverse laser cooling to suppress beam divergence.

Another useful simulation output is the forward velocity distribution at different moments in time. Fig. 5.10 illustrates this distribution in deceleration mode. The initial and final velocities are 345 m/s and 318 m/s, respectively, with the estimated deceleration of 2 km/s^2. Only molecules with an initial velocity above 335 m/s and a final velocity below 325 m/s are shown in the density plot. The gradual chirp of the velocities is seen during the high voltage application (from 0.5 ms till 13.9 ms). Outside this time interval, the forward velocity distribution is constant since there is no force acting on the molecules. Moreover, the velocity range of the decelerated molecules remains the same during the deceleration process and is around 10 m/s (for more details see the next subsection). It is also a direct consequence of the capture velocity of the trap, as shown in Fig. 5.5(b), where identical experimental conditions are used. To summarize, the simulated time evolution of molecular beams inside the decelerator demonstrates stability of the guiding and deceleration processes.

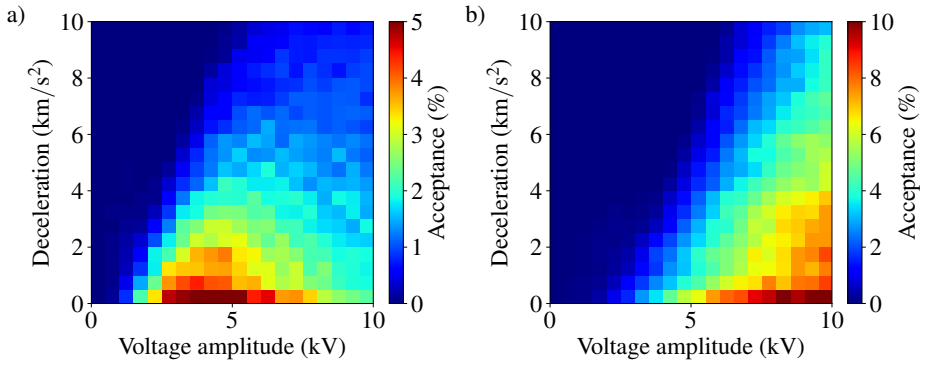

Figure 5.11 | Fraction of SrF molecules in (a) the (N, M_N)=(1, 0) and (b) the (N, M_N)=(2, 0) rotational sublevels in a single trap at the decelerator exit of the total number at the skimmer location.

5.1.4. Overall performance

Finally, the performance of the decelerator with the actual initial phase-space distribution (see Section 5.1.1) is simulated by varying the voltage amplitude of the waveforms and the deceleration strength and recording the amount of molecules captured by the central potential well. It is visualized in Fig. 5.11 for the two lowest trappable rotational states of SrF. The fraction is determined as a ratio of the number of molecules within a single electric trap at the exit of the decelerator (green dots in Fig. 5.6 or Fig. 5.7) and the total number of simulated particles (in this case N=10^4). In Fig. 5.11(a), the fraction of SrF molecules in the (1,0) state is shown. The maximal value of 5% is achieved in AC guiding mode (a=0) at ∼4.5 kV. The turnover point in the Stark curve leads to the reduction of the amount of trapped particles at higher voltage amplitudes. The different shape of the Stark curve for the (2,0) state and consequently the different optimal voltage amplitude are reflected in Fig. 5.11(b). Here the best performance is achieved at ∼10 kV. Furthermore, the absolute amount of trapped molecules is higher by a factor of 2 compared to the (1,0) state as the result of a deeper potential well. It is noteworthy that this increase in the performance is limited by source conditions.

This overview graph can also be used to plan the strategy for the whole experiment. It suggests that the deceleration in the (2,0) rotational sublevel at 10 kV is greatly superior to any other shown conditions. This evidence is also corroborated in the previous studies [6], where the total 3D acceptance of the decelerator has been investigated. In the assumption that the initial population in both states is equal, it will lead to a higher number of molecules at lower

speed in the N=2 level. However, from an experimental perspective, it requires an upgrade of the HV voltage electronics (20 kV_{pp}), which should be capable of a fast sweep from few tens of kHz to few kHz or DC in ∼50 ms. As a general remark, the deceleration in rotational levels with higher N is always more efficient due to the larger Stark shift. On the other hand, one has to take into account the rotational temperature of the molecules at the source, which determines the relative population within the levels. In the simplest rigid rotor approximation, one can find the population probability of a given rotational level N, using the rotational partition function $Z_N(T)=\sum_{N=0}^{\infty}(2N+1)\exp(-\frac{BN(N+1)}{k_BT})$ [7]. From this, we estimated that at a rotational temperature of ≥2.8 K the population in the N=2 level becomes larger that the population in the N=1 level.

5.2. Implementation of a nonadiabatic loss mechanism

So far, all the simulation outputs were obtained in an ideal scenario, when the only loss mechanism was related to the coupling of the axial and transverse motion. To address the question of electric-field dependent molecular number losses (or Majorana losses), we investigate the effects of nonadiabatic transitions in the simulation code. One way to implement this is by comparing the instantaneous amplitude of the angular frequency of a particle $|\omega|\sim v/r$ with the energy splitting ΔE between the trappable and the next non-trappable states [8], later referred to as an effective loss mechanism. However, it does not take into account the actual rotation of the electric field. Therefore, we decided to treat the relative magnitude of two angular frequencies ω_{rot} and ω_{sep} as the adiabaticity criterion, as was pointed out in Section 4.2.2. It allows the effect of rotational coupling between lfs and hfs levels at a single particle level to be seen. Due to the large computational complexity of this method, we cannot run this simulation for a large ensemble of particles. Hence, in the next section, where the simulation outputs are compared with the experimental ones, we use an effective loss mechanism, taking into consideration the angular frequencies of the particles.

By definition, the rotation rate of the electric field is the time derivative of the field vector angle ϕ. The instantaneous value of this angle can be computed from the scalar product of the electric field vector at two consecutive moments separated by Δt. Then, the angular frequency of the electric field rotation at time t_i is given by:

$$\omega_{\mathrm{rot}}(t_i) = \frac{1}{\Delta t}\arccos\frac{\boldsymbol{\mathcal{E}}(t_i)\cdot\boldsymbol{\mathcal{E}}(t_i+\Delta t)}{\mathcal{E}(t_i)\mathcal{E}(t_i+\Delta t)}. \tag{5.3}$$

The energy separation between levels is a function of the electric field strength. Numerically, its instantaneous value can be found from the differential Stark shift as follows:

$$\omega_{\mathrm{sep}}(t_i) = \frac{1}{\hbar}\left(E_{M_N=0}(\mathcal{E}(t_i)) - E_{|M_N|=1}(\mathcal{E}(t_i))\right). \tag{5.4}$$

Examples of two angular frequencies retrieved from the trajectory simulations inside the decelerator for one particle are shown in Fig. 5.12. They give rise to various scenarios of the survival probability. The numerical solutions of the time-dependent Schrödinger equation with a time step of 1 μs (the same as in the numerical integration) provide the probability of finding a molecule in states M_N=0 (black) or $|M_N|$=1 (orange). In all three cases, the angular separation frequency ω_{sep} approaches the electric field rotation rate ω_{rot}. In the first case (Fig. 5.12(a,d)), when the rate of approach is rather small, there is no nonadiabatic coupling between rotational levels, and the system is considered to be totally immune against Majorana-type losses. In the other cases, the angular frequencies evolve differently and almost cross at some point. Note also

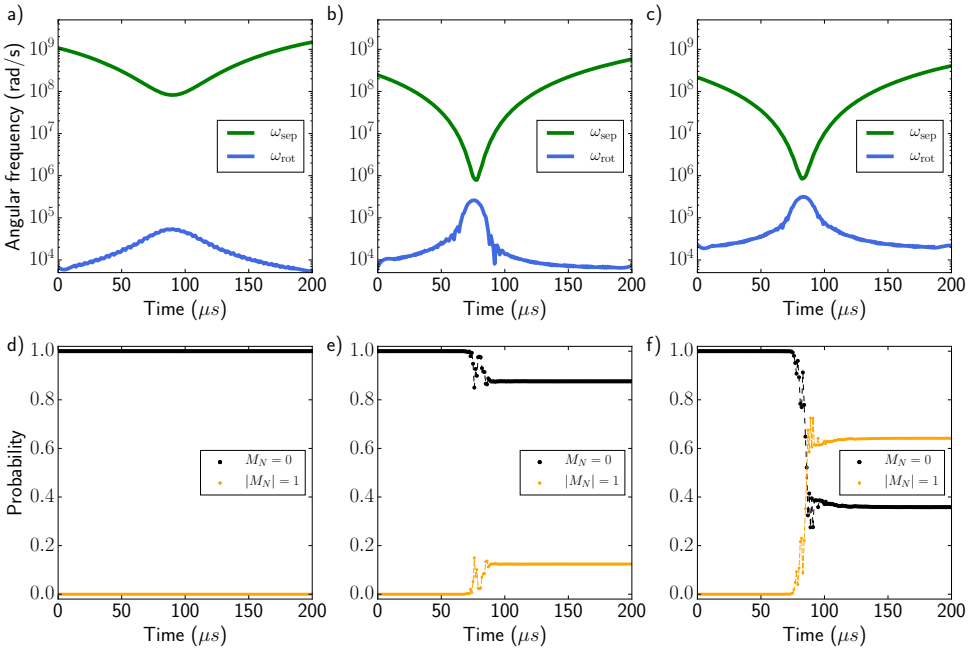

Figure 5.12 | Time evolution of the angular separation frequency ω_{sep} and the electric field rotation rate ω_{rot} (a,b,c) for three sample trajectories from the trajectory simulations, and the corresponding evolution of rotational level populations (d,e,f).

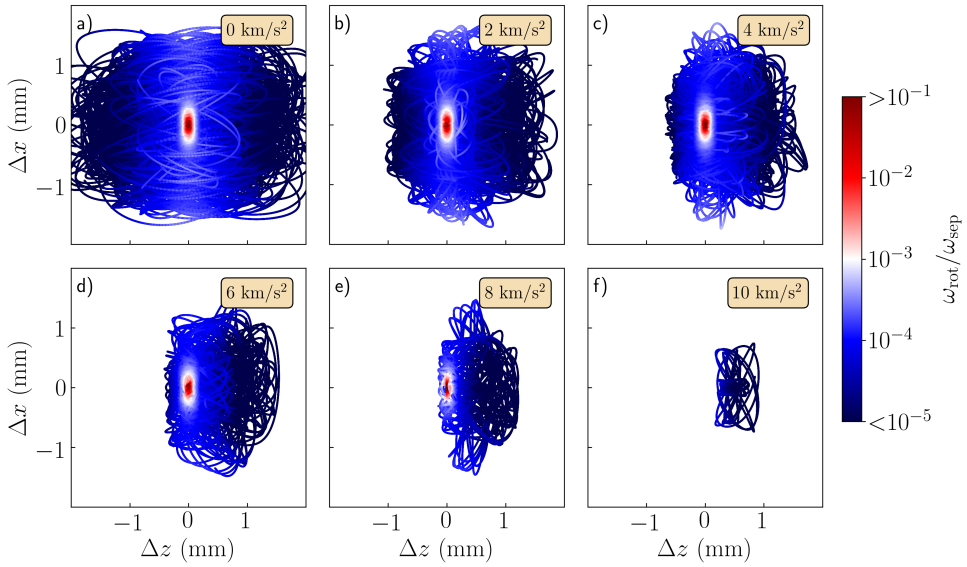

Figure 5.13 | Trajectories of the molecules in the moving frame of reference for a range of deceleration strengths with a step of 2 km/s^2, as shown in the insets. The colormap indicates the instantaneous ratio of the electric field rotation rate ω_{rot} and the angular frequency separation between levels ω_{sep}, which is relevant for the nonadiabatic transitions.

a much faster electric field rotation in panels (b-c), which becomes greater than 10^5 rad/s. As a result, the transition probability becomes significant around t=80 μs for both cases, and its strength depends on the particular shapes of the coupling parameters. The likelihood that the molecule remains in the trappable lfs state during such a process is equal ∼90% and ∼40% for cases (b) and (c), respectively, leading to molecular number losses. Here we also effectively ignore an effect of the Stark force, since the change of the character from lfs to hfs will change the trajectory of the molecule as well as values of the nonadiabatic parameters.

In order to visualize the effect of a rotational coupling for an ensemble of particles, one can trace the adiabaticity parameter $\omega_{\mathrm{rot}}/\omega_{\mathrm{sep}}$ as a function of time. The result is shown in Fig. 5.13, where the 2D trajectories (transverse position vs longitudinal position) relative to the center of the moving trap have been recorded during 12 ms for a number of deceleration strengths. All subplots cover the same 16 mm^2 region, and the color code denotes the adiabaticity parameter. At relatively small deceleration strengths (panels a-c), there is a substantial volume in space (closer to the red edge) where the nonadiabatic losses can in principle occur. In this region, the adiabaticity criterion ($\omega_{\mathrm{rot}} \ll \omega_{\mathrm{sep}}$) may break down. When the deceleration is significant (panels d-e), the average displacement

of the molecules with respect to the trap center is large, leading to a smaller probability for particles to be transferred to the non-trappable state. In the case of the largest simulated deceleration of 10 km/s^2 (Fig. 5.13(f)), the transition probability can be practically neglected. However, in this case, the amount of particles that remain in the trap is also much less compared to other cases, which reflects a different effective potential depth. To conclude, it is conceivable that during the deceleration process there is a competition between reduction in molecular number due to the Stark force and suppression of the nonadiabatic transitions due to spatial displacement in the co-moving reference frame. This conclusion is also in agreement with the simulations in a traditional switching type Stark decelerator [9].

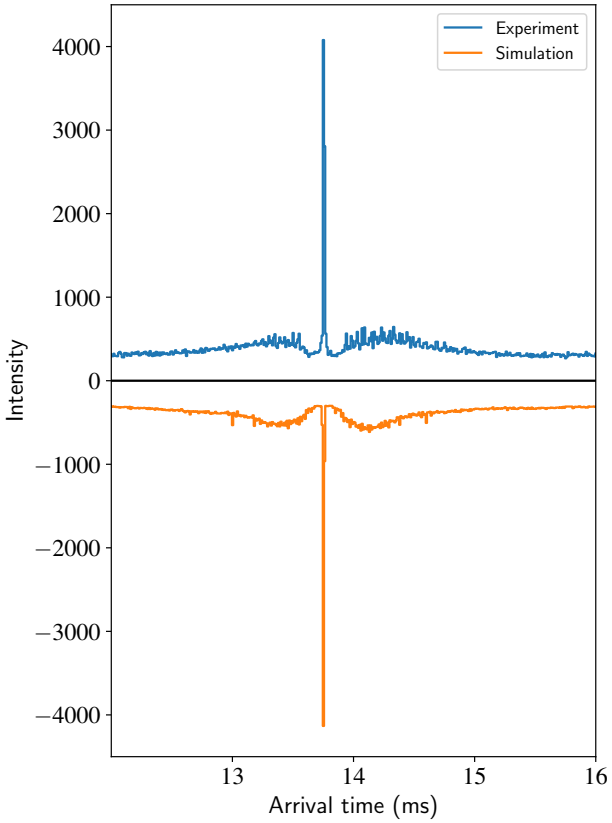

Figure 5.14 | Experimental (blue) and simulated (orange) time-of-flight histograms obtained for identical experimental conditions (bin size: 10 μs). The simulated output has a vertical offset and is reflected for clarity.

5.3. Comparison of simulations with experimental results

Here the comparison of simulation outputs with the experimental data from Chapter 4 is presented. Since all measured information about the molecular beams comes from the binned time-of-flight (TOF) histograms of the laser-induced fluorescence signal (see Section 4.1.1), we obtain the same histograms from the numerical simulations. Care has been taken to ensure the identical binning of the simulated outputs. We also introduce a Gaussian noise in the simulated TOF, to accommodate the intrinsic noise in the chosen detection method.

As mentioned in Chapter 3, under some experimental conditions, there is a good agreement between experiment and simulations in an ideal lossless scenario. This is illustrated in Fig. 5.14, where time-of-flight histograms are shown in AC guiding mode for both outputs in the 4.5 m long TWSD. The set of experimental parameters is identical: the voltage amplitude is 3.0 kV, and the guiding velocity is 345 m/s. As can be seen, all essential features of the experimental TOF (the height of the central peak, the shape and asymmetry of the wings) are reproduced in the simulation without the necessity to include any loss mechanisms.

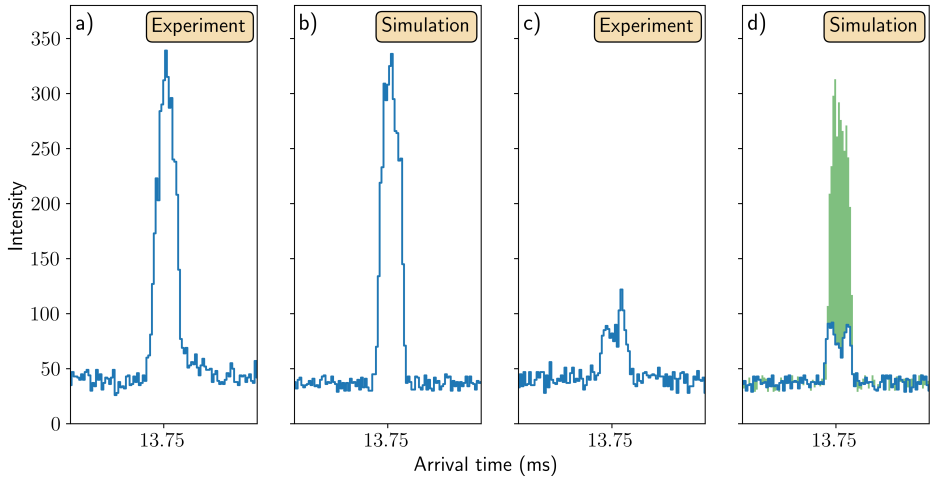

Figure 5.15 | Experimental (a,c) and simulated (b,d) time-of-flight histograms obtained in AC guiding mode at a velocity of 345 m/s. The applied voltage amplitude is 3.0 kV (a,b) and 4.5 kV (c,d). The green shaded area represents the time-of-flight histogram in a lossless scenario. The time window for every plot is 13.7−13.8 ms and the bin size is 1 μs.

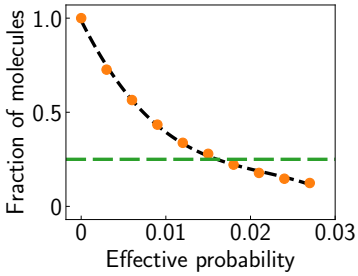

Figure 5.16 | Reduction of number of molecules with an increase of the effective probability for nonadiabatic transitions. Green dashed line shows the experimentally observed 25% fraction of remaining molecules.

Panels (a) and (b) in Fig. 5.15 reproduce the TOFs from Fig. 5.14 for experiment and simulation outputs, respectively, with a focus on the central peak. These peaks match well also with different quantization of the time axis. Fig. 5.15(c) depicts the experimental TOF histogram at a voltage amplitude of 4.5 kV, which reveals molecular number loss (see Section 4.1.2). The simulated TOF histogram for these conditions in a lossless scenario is shown on the last panel of the figure by a solid background. There is an obvious mismatch between the expected and reported results. In order to reconcile these outcomes, we run the simulation code with the nonadiabatic transition probabilities implemented. This is shown on the last panel as a blue TOF histogram, with a good agreement between the two results. The loss is implemented by scanning the effective loss

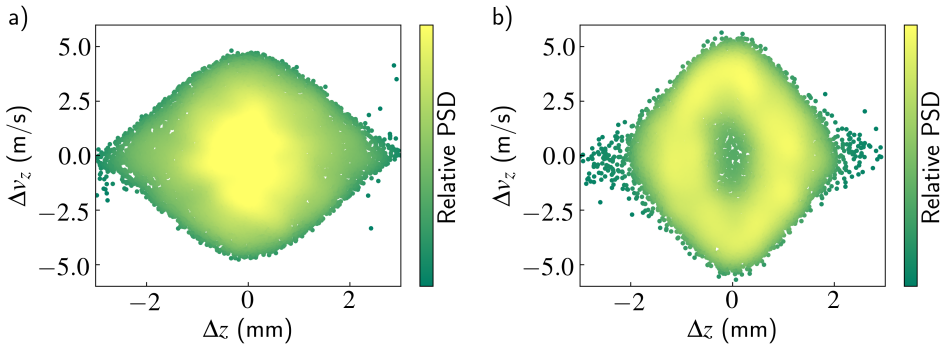

Figure 5.17 | Longitudinal phase-space distribution of particles that corresponds to the time-of-flight histograms from Fig. 5.15. Voltage amplitudes are (a) 3.0 kV and (b) 4.5 kV. The color code denotes the relative phase-space density.

probability and selecting the best match with the experimental result, which is visualized in Fig. 5.16. Hence, for the simulated TOF histogram in Fig. 5.15(d) we used an effective probability of 1.6%.

Finally, we investigate the effect of nonadiabatic transitions in the phase space. This is illustrated in Fig. 5.17, where we plot longitudinal positions and velocities of the molecules at the last moment of the high-voltage application (t=13.0 ms). The relative phase-space density changes from low (green) to high (yellow). The panel (a) shows a dense phase-space occupation occurring at a voltage amplitude of 3.0 kV, which corresponds to the TOF histogram in Fig. 5.15(b). As anticipated, Fig. 5.17(b) shows a significant depletion of the phase-space density at the center of the trap at a voltage amplitude of 4.5 kV that is related to the smaller integral shape of the TOF histogram in Fig. 5.15(d). This phase-space distribution demonstrates a significant reduction of molecules with small position or velocity components.

5.4. Conclusions

In this chapter, we reported the results of the numerical trajectory simulations of polar molecules inside a time-dependent and spatially inhomogeneous electric field. These simulations are developed in order to gain insight into criteria for stable operation of a traveling-wave Stark decelerator. In the first part of the chapter, we tested the numerical model in an ideal scenario (without any loss mechanisms). The full three-dimensional phase-space acceptance is found for the case of SrF molecule in the $X^2\Sigma^+$ (N, M_N)=$(1, 0)$ state. It reaches its maximum value of $\sim$4000 mm^3(m/s)^3 in guiding mode at a voltage amplitude of 3.0−5.0 kV. In deceleration mode, the total phase-space acceptance decreases with increasing deceleration strength.

The second part of the chapter is about simulating molecular trajectories taking into account the rotational coupling between lfs and hfs states. By tracing the instantaneous rotation frequencies of the electric field and the separation energies between the (N, M_N)=$(1, 0)$ and (N, M_N)=$(0, 0)$ levels, we conclude that close to the trap center the adiabaticity criterion can indeed break down. Comparison of the experimental data with the trajectory simulations shows good agreement. The enhancement of loss rates at high voltage amplitudes remains an open question.

References

[1] J. Muller, *Electric fields and molecule motion in a traveling-wave Stark decelerator* (Bachelor's thesis. University of Groningen, 2017).

[2] H. L. Bethlem, F. M. H. Crompvoets, R. T. Jongma, S. Y. T. van de Meerakker, and G. Meijer, *Deceleration and trapping of ammonia using time-varying electric fields,* Phys. Rev. A **65**, 053416 (2002).

[3] K. Dulitz, N. Vanhaecke, and T. P. Softley, *Model for the overall phase-space acceptance in a Zeeman decelerator,* Phys. Rev. A **91**, 013409 (2015).

[4] S. Y. T. van de Meerakker, N. Vanhaecke, H. L. Bethlem, and G. Meijer, *Transverse stability in a Stark decelerator,* Phys. Rev. A **73**, 023401 (2006).

[5] J. E. van den Berg, S. H. Turkesteen, E. B. Prinsen, and S. Hoekstra, *Deceleration and trapping of heavy diatomic molecules using a ring-decelerator,* Eur. Phys. J. D **66**, 235 (2012).

[6] J. E. van den Berg, *Traveling-wave Stark deceleration of SrF molecules*, Ph.D. thesis, University of Groningen (2015).

[7] I. V. Hertel and C.-P. Schulz, *Atoms, Molecules and Optical Physics 2* (Springer, Berlin, Germany, 2015).

[8] M. Buisman, *Non-adiabatic losses in traveling-wave Stark deceleration* (Bachelor's thesis. University of Groningen, 2017).

[9] T. E. Wall, *Guiding and decelerating cold, heavy, polar molecules*, Ph.D. thesis, University of London (2010).

6

Summary and Outlook

The most accurate and predictive theory of modern physics, the Standard Model of elementary particles, has some intrinsic problems. How to solve these problems is an open question. A large number of Beyond-the-Standard-Model (BSM) extensions have been proposed to make the Standard Model more complete. New speculative models typically involve the existence as-of-yet undiscovered particles or interactions. The validation or rejection of these extensions requires a new generation of experiments with increased sensitivity. Given its high-precision experimental methods, atomic, molecular and optical (AMO) physics is uniquely positioned to contribute to the search for "New Physics", which can be just "around the corner".

Molecules are excellent candidates in the search for new phenomena in a manner that is complementary to high-energy experiments in accelerators and colliders. This is possible due to very specific internal properties of some molecules (usually heavy ones in which relativistic effects play a prominent role). By specific properties we mean enhanced sensitivity of the molecular energy level structure to a number of parameters predicted by the Standard Model. Any discrepancy between predicted and observed parameters would immediately indicate BSM physics. Despite this enhancement, the exploration of molecules for fundamental physics tests is limited by experimental control over molecules. One way to increase the sensitivity is to prepare slow and cold molecular samples, that allows for a longer coherent interaction time. Recent advances in the control of molecules by means of external fields and laser light render this approach feasible. This also motivated the work described in this dissertation.

Molecules in the low-temperature regime are typically divided into cold and ultracold with temperature ranges of 1 mK$-$1 K and $<$1 mK, respectively. They

can be used in many other applications apart from fundamental physics tests. For example, cold molecules are interesting as a platform to study dipole-dipole interactions and controlled chemistry. Ultracold molecules can be used to study new phases of matter (quantum degeneracy) and provide a promising testing bed for quantum information processing. The rich diversity of possible scientific explorations of cold and ultracold molecules makes this challenging branch of modern AMO physics very attractive and active.

In this thesis, we describe the operation of the traveling-wave Stark decelerator at the edge of its functionality required for the production of intense and slow beams of heavy molecules. This apparatus is designed for slowing down relatively fast (300−350 m/s) beams of selected molecular species by means of controllable inhomogeneous electric fields. Such an approach is based on the Stark shift, the underlying physics of which is concisely described in **Chapter 2**. Any polar molecule possesses a molecule-frame electric dipole moment and is therefore susceptible to an external electric field. The molecule-field interaction leads to the splitting and shift of the energy levels depending on the internal structure of the molecule. Molecules in some quantum states are strongly attracted to, while others are repelled from a local minimum of the electric field strength. These states are referred to as low-field seeking and high-field seeking states, respectively. The creation and precise control of the electric field distribution is a key concept of Stark decelerators for low-field seeking molecules.

In **Chapter 3**, the design and characterization of the 4 meter long traveling-wave Stark decelerator are given. The detailed description of the main structural components of the experimental setup comprises the first part of the chapter. The setup is schematically depicted in Fig. 6.1. It consists of a supersonic source of SrF molecules, modular ring-type decelerator, and detection system. The oscillating voltage applied to the rings of the decelerator forms moving 3-dimensional traps for molecules in low-field seeking states.

The choice of SrF molecule for these experiments is motivated by its unique properties. SrF is a moderately heavy free radical (its mass is 107 amu) with a predicted high sensitivity to violation of parity symmetry. Furthermore, the energy level structure of SrF is favorable to laser cooling − it was the first molecule to be laser-cooled. The remainder of the chapter is dedicated to the experimental results obtained with the apparatus. The strongest deceleration strength achieved was around 9 km/s^2: a supersonic beam of heavy molecules has been slowed down from 290 m/s to 120 m/s. This result sets the record for the kinetic energy removal in decelerators: the molecular packet at the exit of the apparatus has only 15% of its initial kinetic energy. The experimental results could in almost all cases be reproduced by numerical trajectory simulations.

According to the trajectory simulations, in an ideal scenario, a 4.5 meter

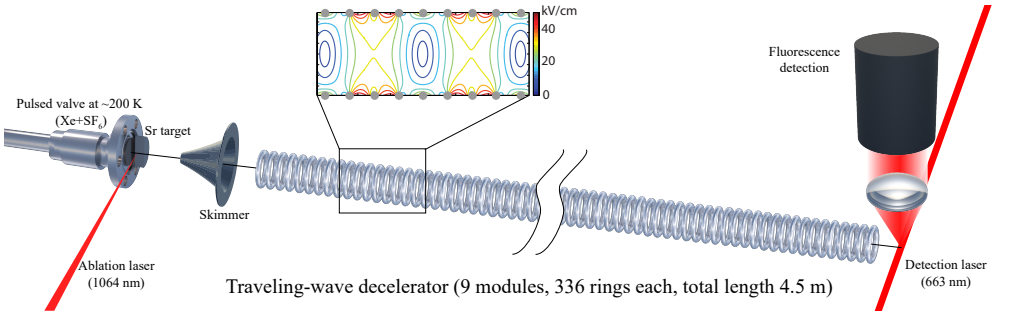

Figure 6.1 | A schematic overview of the experimental setup for creating, decelerating and detecting heavy diatomic molecules. It consists of a supersonic source of SrF molecules, modular traveling-wave Stark decelerator, and laser-induced fluorescence detection zone.

long Stark decelerator provides sufficient stopping distance to bring a sizable fraction of a supersonic beam of SrF molecules to rest in the laboratory frame. The characterization of this apparatus, consisting of 9 modules, is presented in **Chapter 4**. The experimental results on guiding and deceleration reveal under certain conditions systematic deviations from optimum performance of the decelerator, which are discussed in the second part of the chapter. The aforementioned deviations represent molecular number losses and are clearly observed in experimental time-of-flight profiles. The losses can be seen from a position-dependent depletion of molecules from the trap center, whilst in a scenario without losses, the distribution of molecules has a maximum in the trap center. In order to investigate this loss mechanism, we have developed a model that incorporates the rotation rate of the electric field inside our apparatus. This model gives the relevant criterion for adiabatic motion of a molecule in a time-varying electric field. If the rotation frequency of the field is much smaller than the angular frequency separation between trappable and non-trappable quantum states, the molecule can follow the temporal evolution of the field. Otherwise, a non-zero probability of a nonadiabatic transition between states exists, leading to molecular number losses. This concept is schematically visualized in Fig. 6.2.

In order to validate the hypothesis of nonadiabatic transitions driving losses in the traveling-wave Stark decelerator, we have developed numerical trajectory simulations with an effective implementation of these transitions. The simulation of an ideal beam propagation throughout the apparatus and the loss-related parameters are discussed in **Chapter 5**. The numerical results in the ideal scenario include: the phase-space distribution of individual molecules at any moment in time in both laboratory and co-moving frames of reference, the longitudinal and transverse separatrices of the stable phase-space regions, resulting in an overall review of the performance. The induced coupling between low-field seeking and

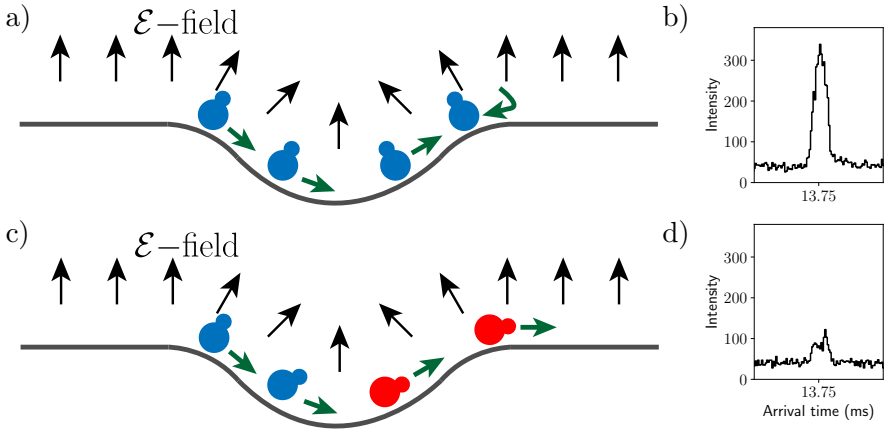

Figure 6.2 | A schematic illustration of the adiabatic motion of a molecule in a one-dimensional electric field trap (a) and the corresponding experimental time-of-flight histogram for an ensemble of molecules (b). In this case, the molecules can follow the change of the electric field direction and remain in the trappable quantum state. A nonadiabatic transition can occur at the trap center for a single molecule (c) and the resulting time-of-flight histogram is shown in (d). In this case, the molecules cannot maintain the quantization axis and make a transition into a non-trappable quantum state with a certain probability, leading to losses.

high-field seeking states is investigated by tracing the rotation rate of the electric field and the energy separation between these states. The numerical results with an effective model of loss mechanism confirms our hypothesis, however it does not completely explain why the losses are the most prominent at high voltage amplitudes, as we observe in our experiments.

Losses due to the nonadiabatic transitions in our Stark decelerator significantly hinder a complete deceleration of a supersonic molecular beam to a standstill. Even though the losses can be suppressed in deceleration mode, the slowest molecules detected in the 4.5 meter long decelerator have a velocity of 220 m/s, which is larger than the lowest velocity achieved in the 4 meter long apparatus. Therefore, the experimental findings of these Majorana-type losses in the traveling-wave decelerator and their thorough analysis are of importance for future experiments with cold molecules, where the number of slow molecules should be maximized.

Outlook

A motivation for the experiments reported in this thesis was the production of an intense and slow beam (<100 m/s) of heavy molecules, which would represent a major step towards the test of fundamental physics at record sensitivity using molecules. The results presented with SrF molecules in this thesis show the limitations of the experimental approach in its current implementation. Here we discuss various options to mitigate the observed losses in molecular number and the main implications for the future experiments.

When decelerating from supersonic beam velocities, we pushed the performance of the decelerator to its limits, discovering a regime with significant instabilities. These unwanted losses have not been observed at lower initial molecular beam velocities. Therefore, a natural way around this problem is to use a cryogenic buffer gas source. The benefits of this molecular production method are twofold: it is proven to deliver a much brighter beam compared to a supersonic source, and the terminal velocities of such beams are typically a factor of 1.5−2.0 lower compared to the slowest supersonic beams. The large pulse length that these beams typically have should not cause any limitation for a slow-beam experiment, since many moving electric traps can be populated and slowed down in parallel. Generally, while coupling the cryosource to the decelerator, care has to be taken to ensure optimal matching of the phase-space distribution of the beam to the phase-space acceptance of the decelerator. In this regard, it is anticipated that collimating a beam passively (through a special geometry of the nozzle) or actively (an electrostatic lens or a laser cooling stage) should deliver even more particles for the ultimate experiment.

In practice, the number of molecules in the desired quantum state at the end of the decelerator critically depends on the combined settings of the molecular source and the decelerator. To address the optimization procedure, a promising approach could be to use computer-controlled exploration of the parameter space by e.g. evolutionary algorithms.

Motivated by a potential to discover new physics, an experiment with a slow and intense beam of BaF molecules is currently being prepared in our group. The slow beam for this experiment will be attained in the Stark decelerator coupled to a cryosource. In order to produce an intense beam of slow BaF molecules, one has to supply to the decelerator electrodes a sinusoidal waveform with an amplitude of 20 kV_{pp}. Apart from voltage amplification, which is already quite challenging given the bandwidth of the waveforms, the fidelity of the high-voltage waveforms is also a major concern for a stable performance of the Stark decelerator. Even though we did not find it to limit our experiments, jitter of the waveform signal can lead to the enhanced rotation rate of the effective electric field inside the trap.

Moreover, neighboring electrodes in a long decelerator represent a capacitive load. Hence, to maintain a high waveform fidelity, the high-voltage electronics should be able to supply sufficient current.

In order to completely suppress nonadiabatic transitions in the traveling-wave Stark decelerator one can consider decelerating molecules in exclusively low-field seeking states, i.e. states that are energetically far removed from high-field seeking states. This approach should provide practically zero probability for losses via this channel. Examples of Stark-deceleratable molecules with such energy level structure are ammonia (NH_3) and methanol (CH_3OH). Unfortunately, all molecules laser-cooled so far have a degeneracy of quantum levels of opposite character at zero electric field strength. Applying a constant bias electric or magnetic field is also a promising approach for an electrostatic trap. However, for a ring geometry of our decelerator, it seems to be practically impossible.

Another important direction in the field of cold molecules is trapping experiments. In this case clouds of molecules can be coherently interrogated by means of laser spectroscopy, or used to explore cold controlled chemistry. Recent advances in the laser cooling and trapping of various species demonstrate a promising path to reach dense and ultracold samples of molecules. An important parameter in this regard is the capture velocity, which determines the requirements for loading into a conservative optical or magnetic trap. A combination of the cryosource and the Stark decelerator followed by a brief period of laser cooling can be used as a way to load molecules in e.g. an optical dipole trap, which under so-called "magic conditions" offers a practically state-independent trapping potential. With this approach, large samples of heavy laser-coolable molecules, such as SrF, BaF, and perhaps even polyatomic molecular species, can be held in an optical potential for over one second. This promises to be an ideal platform for table-top tests searching for new physics with unprecedented precision.

7

Nederlandse Samenvatting

Het Standaardmodel van de elementaire deeltjesfysica is tot nu toe de meest betrouwbare theorie in de moderne natuurkunde, maar bevat ook intrinsieke problemen. Hoe deze problemen op te lossen is nog een open vraag. Om deze probleem te overkomen zijn een groot aantal voorbij-het-Standaardmodel (VSM) aanvullingen voorgesteld. Karakteristiek voor de nieuwe aanvullingen is de introductie van nieuwe nog niet ontdekte deeltjes of wisselwerkingen. De toetsing van deze aanvullingen vergt een nieuwe generatie van experimenten met verhoogde precisie. Gegeven de hoge precisie waarmee metingen gedaan kunnen worden in atoom-, molecuul-, en optische (AMO) fysica is deze tak van de natuurkunde veelbelovend om bij te dragen aan de zoektocht naar "nieuwe natuurkunde", welke binnen handbereik kan zijn.

In de zoektocht naar nieuwe natuurkundige verschijnselen hebben experimenten met moleculen een uitstekende positie om hoge-energie botsingsexperimenten met deeltjesversnellers te complementeren. Dit wordt mogelijk gemaakt door zeer specifieke interne eigenschappen van sommige moleculen (vooral zware moleculen waarin relativistische effecten prominent aanwezig zijn). Met de specifieke interne eigenschappen wordt vooral een verhoogde gevoeligheid van de moleculaire energiestructuur voor een aantal van de door het Standaardmodel voorspelde parameters bedoeld: elke meetuitkomst die afwijkt van de door het Standaardmodel voorspelde parameterwaarde duidt VSM natuurkunde aan. Ondanks deze verhoogde gevoeligheid wordt het testen van fundamentele natuurkunde met moleculen beperkt door onvoldoende experimentele controle over de moleculen. Eén manier om de gevoeligheid te vergroten is het voorbereiden van langzame ultrakoude molecuulbundels, die voor een langere coherente interactietijd zorgen. Recente ontwikkelingen omtrent de controle over moleculen met behulp van

externe velden en laserlicht maken deze benadering mogelijk. Dit is ook de motivatie voor het onderzoek in dit proefschrift.

Moleculen met een lage temperatuur worden doorgaans ingedeeld in koude en ultrakoude moleculen met respectievelijke temperatuurgebieden 1 mK−1 K en <1 mK. Naast de hierboven beschreven toepassingen in het testen van fundamentele natuurkundige theorieën kunnen deze moleculen ook gebruikt worden voor andere doeleinden. Ultrakoude moleculen kunnen bijvoorbeeld ook gebruikt worden voor het bestuderen van dipool-dipoolwisselwerkingen en gecontroleerde scheikunde. Ze kunnen ook gebruikt worden voor het bestuderen van nieuwe aggregatietoestanden van materie (kwantumontaarding) en zijn ze veel belovend voor het testen van kwantuminformatieverwerking. De veelzijdigheid van wetenschappelijk onderzoek met ultrakoude moleculen maakt deze tak van AMO-fysica zeer aantrekkelijk en actief.

In dit proefschrift beschrijven we de werking van de lopendegolf-Starkafremmer op de grens van zijn mogelijkheden; dit is nodig voor de productie van intense en langzame bundels van zware moleculen. Dit apparaat is ontworpen voor het afremmen van relatief snelle (300−350 m/s) bundels van geselecteerde molecuulsoorten door middel van gecontroleerde niet-homogene elektrische velden. De werking is gebaseerd op de Starkverschuiving, de fysische principes hiervan worden uitgebreid beschreven in **Hoofdstuk 2**. Elke polaire molecuul bevat een elektrisch-dipoolmoment in zijn eigen coördinatenstelsel en is dus beïnvloedbaar door externe elektrische velden. De wisselwerking tussen het molecuul en het veld leidt tot splitsingen en verschuivingen van energieniveaus, afhankelijk van de interne moleculaire structuur. De elektrisch-veld minima trekken moleculen in bepaalde kwantumtoestanden aan, terwijl anderen hiervan worden afgestoten. Deze kwantumtoestanden worden respectievelijk aangeduid als laagveldzoekende en hoogveldzoekende toestanden. Het genereren en precies controleren van een elektrisch-veld verdeling is een doorslaggevende eigenschap van Starkafremmers voor laagveldzoekende moleculen.

In **Hoofdstuk 3** zijn het ontwerp en de karakterisatie van de 4 meter lange lopendegolf-Starkafremmer beschreven. Het eerste gedeelte hiervan bestaat uit een gedetailleerde beschrijving van de structurele hoofdonderdelen van de experimentele opstelling. De opstelling is schematisch weergegeven in Figuur 7.1. Het bestaat uit een supersonische bron van SrF moleculen, de modulaire ringafremmer en een detectiesysteem. De oscillerende spanning over de ringen van de afremmer vormt driedimensionale vallen waarin laagveldzoekende moleculen ingevangen kunnen worden.

Er is voor SrF gekozen omdat deze speciale eigenschappen heeft. SrF is een relatief zware vrije radicaal (massa is 107 atomaire massaeenheden) met een hoge voorspelde gevoeligheid voor pariteitschending. Verder is de energieniveau-

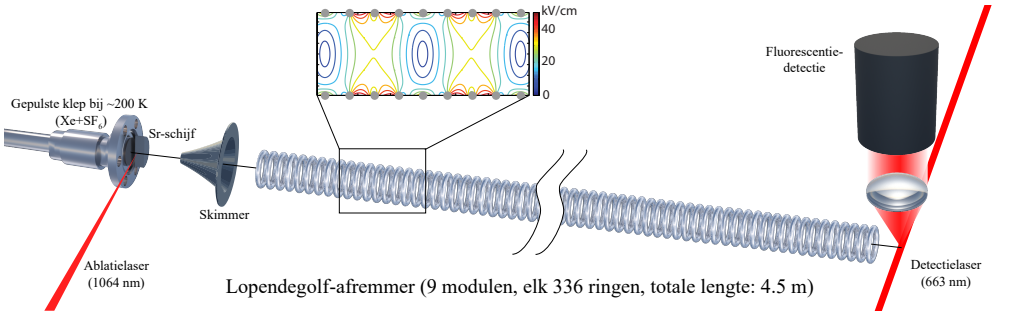

Figuur 7.1 | Een schematische overzicht van de experimentele opstelling voor het produceren, afremmen en detecteren van zware tweeatomige moleculen. Het bestaat uit een supersonische bron voor SrF moleculen, een modulaire lopendegolf-Starkafremmer en een fluorescentiedetectiesysteem

structuur van SrF geschikt voor laserkoeling. Het is het eerste lasergekoelde molecuul ooit. De rest van het hoofdstuk is toegewijd aan de experimentele resultaten verkregen met de opstelling. De grootste afremkracht bereikt is rond 9 km/s^2: een supersonische bundel van zware moleculen is vertraagd van 290 m/s naar 120 m/s. Dit resultaat is een record in reducering van kinetische energie in Starkafremmers. Aan het einde van de afremmer heeft de molecuulbundel slechts 15% van zijn initiële kinetische energie over. Het was mogelijk deze experimentele resultaten voor bijna alle gevallen te reproduceren met numerieke trajectsimulaties.

De trajectsimulaties laten zien dat een 4.5 meter lange Starkafremmer in ideale omstandigheden lang genoeg is om een significant deel van een supersonische bundel SrF moleculen tot stilstand te brengen in het laboratoriumcoördinatenstelsel. De karakterisatie van dit apparaat, bestaande uit 9 modulen, wordt beschreven in **Hoofdstuk 4**. De experimentele resultaten voor het begeleiden en afremmen van de bundel wijken in bepaalde condities systematisch af van de optimale prestaties van de afremmer; dit wordt beschouwd in het tweede gedeelte van het hoofdstuk. De eerdergenoemde afwijkingen lijden tot een reductie van het aantal moleculen en dit is duidelijk terug te zien in de experimentele vliegtijdprofielen. De reductie is te zien als een positieafhankelijke uitdunning van moleculen in het midden van de val, terwijl zonder verliezen de verdeling van moleculen een maximum heeft in het midden van de val. Om dit verliesmechanisme te onderzoeken, hebben we een model ontwikkeld waarin de rotatiesnelheid van het elektrisch veld in ons apparaat is opgenomen. Dit model geeft de relevante voorwaarde voor adiabatische beweging van een molecuul in een tijdvariërende elektrisch veld. Als de rotatiefrequentie van het veld veel kleiner is dan het hoekfrequentieverschil tussen invangbare en niet-invangbare kwantumtoestan-

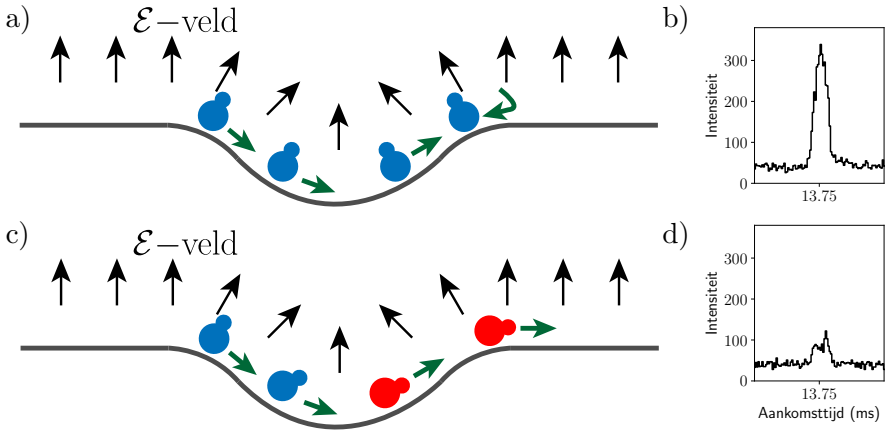

Figuur 7.2 | Een schematische weergave van de adiabatische beweging van een molecuul in een eendimensionale elektrostatische val (a) en de experimentele vliegtijdhistogram, voor een reeks moleculen (b). In dit geval kunnen de moleculen veranderingen in de richting van het electrisch veld volgen om zo in een invangbare kwantumtoestand te blijven. In het midden van de val is een niet-adiabatische overgang van een molecuul mogelijk (c) en de bijbehorende vliegtijdhistogram is weergegeven in (d). In dit geval zullen sommige moleculen hun kwantisatie-richting niet behouden en met een bepaalde waarschijnlijkheid de overgang naar een niet-invangbare kwantumtoestand maken, wat leidt tot verliezen.

den kan het molecuul de tijdafhankelijke verandering van het veld volgen. Zo niet, ontstaat er een mogelijkheid voor niet-adiabatische overgangen tussen de kwantumtoestanden. Dit idee is schematisch weergegeven in Figuur 7.2.

Om de hypothese van molecuulverliezen in de lopendegolf-Starkafremmer door niet-adiabatische overgangen tussen toestanden te toetsen, hebben we numerieke trajectsimulaties ontwikkeld die effectief deze overgangen nabootsen. De simulaties van een ideale bundelvoortplanting door het apparaat en de verliesgerelateerde paramaters worden beschreven in **Hoofdstuk 5**. De numerieke resultaten in het ideale geval bevatten: de faseruimte verdeling van individuele moleculen op elk tijdstip in zowel het laboratoriumcoördinatenstelsel als de meebewegende referentiecoördinatenstelsels en de longitudinale en transversale separatrices van stabiele faseruimtegebieden, resulterend in een algemene beschouwing van de prestaties. De geïnduceerde koppeling tussen laagveldzoekende en hoogveldzoekende kwantumtoestanden wordt onderzocht door het bijhouden van de rotatiesnelheid van het elektrisch veld en het energieverschil tussen deze toestanden. De numerieke resultaten bevestigen onze hypothese, maar verklaren nog niet waarom deze verliezen meer tot uiting komen bij hoge spanningen, zoals geobserveerd tijdens de experimenten.

Verliezen door niet-adiabatische overgangen in onze Starkafremmer zijn een

significante beperking voor de complete afremming van een supersonische molecuulbundel. Hoewel de verliezen beperkt kunnen worden tijdens het afremmen, hebben de langzaamst gemeten moleculen in een 4.5 meter lange afremmer een snelheid van 220 m/s, dit is sneller dan de langzaamst gemeten moleculen in een 4 meter lange afremmer. De experimentele bevindingen van deze Majorana-achtige verliezen in een lopendegolf-afremmer en hun grondige analyse zijn daarom van belang voor toekomstige experimenten met koude moleculen waarin het aantal vertraagde moleculen geoptimaliseerd moet worden.

Vooruitzicht

Een motivatie voor de experimenten beschreven in dit proefschrift is de productie van een intense en langzame bundel (<100 m/s) zware moleculen, welke een grote stap zou zijn richting het testen van fundamentele natuurkunde met de hoogste gevoeligheid ooit. De in dit proefschrift beschreven resultaten voor SrF moleculen tonen de beperkingen van de huidige experimentele benadering. Hier beschouwen we verschillende mogelijkheden om de geobserveerde verliezen in molecuulaantal te beperken en de belangrijkste gevolgen voor toekomstige experimenten.

Tijdens het afremmen van moleculen hebben we de afremmer op de grens van zijn mogelijkheden gebruikt; hierdoor ontdekten we een domein met significante instabiliteit. Deze ongewenste verliezen zijn niet geobserveerd bij lage beginsnelheden van de molecuulbundel. Hieruit blijkt dat het gebruik van een cryogene molecuulbron een mogelijke oplossing is voor dit probleem. Een dergelijke bron heeft twee voordelen. Het is bewezen dat het een hogere molecuulproductie heeft ten opzichte van een supersonische bron, en de geproduceerde bundel heeft een 1.5-2.0 keer lagere snelheid ten opzichte van de langzaamste supersonische bundels. De typerende lange bundel zou geen beperking moeten zijn voor een langzame-bundel experiment, aangezien meerdere lopende elektrische vallen bezet kunnen worden en zo tegelijkertijd worden afgeremd. Bij het koppelen van de cryogene bron aan de afremmer moet ervoor gezorgd worden dat faseruimteverdeling van de bundel zo goed mogelijk past in de faseruimteacceptantie van de afremmer. In dit opzicht is het aanneembaar dat collimatie van de bundel zal resulteren in een verhoging van het aantal moleculen voor het uiteindelijke experiment. De collimatie kan zowel passief (middels een bepaalde vorm van de bronuitgang) als actief (middels een elektrostatische lens of laserkoeling) plaatsvinden.

In de praktijk is het zo dat het aantal moleculen in de gewenste kwantumtoestand aan het einde van de afremmer sterk afhankelijk is van de instellingen van zowel de molecuulbron als de afremmer. Om de instellingen te optimaliseren zou gebruik gemaakt kunnen worden van een veelbelovende benadering, namelijk computergestuurde optimalisatie van de parameters door bijvoorbeeld evolutionaire algoritmen.

Gedreven door de mogelijke ontdekking van nieuwe natuurkunde wordt in onze groep een experiment met een intense en langzame bundel van BaF moleculen voorbereid. De langzame bundel voor dit experiment zal verkregen worden met de Starkafremmer gekoppeld aan een cryogene molecuulbron. Om een intense en langzame bundel van BaF moleculen te produceren, moeten de elektroden van de afremmer gevoed worden met een sinusoïde spanningsvorm met een amplitude van 20 kV_{pp}. Naast spanningsversterking, die al een uitdaging

vormt vanwege de bandbreedte van de spanningsvormen, is een goede kwaliteit van de hoogspanningsvormen van groot belang voor een stabiele werking van de Starkafremmer. Hoewel het geen beperking vormde tijdens onze experimenten kan vervorming van de spanningsvorm leiden tot verhoging van de rotatiesnelheid van het effectieve elektrisch veld in de val. Verder geldt dat naastgelegen elektroden in een lange afremmer een capacitieve belasting vormen. Om een hoge spanningsvormkwaliteit te behouden, moet de hoogspanningselektronica in staat zijn genoeg stroom te leveren.

Om niet-adiabatische overgangen in de lopendegolf-Starkafremmer tegen te gaan, kan ervoor gekozen worden om alleen moleculen in een laagveldzoekende toestand af te remmen, oftewel toestanden die energetisch ver verwijderd zijn van hoogveldzoekende toestanden. Deze benadering voorkomt praktisch alle verliezen door toestandsovergangen. Voorbeelden van Starkafrembare moleculen met een dergelijke energiestructuur zijn ammoniak (NH_3) en methanol (CH_3OH). Helaas is het zo dat tot nog toe alle laserkoelbare moleculen een tegenovergestelde kwantumontaarding hebben in de afwezigheid van een netto elektrisch veld. Het toevoegen van een constant elektrisch of -magnetisch veld is ook een veelbelovende oplossing voor dit probleem in een elektrostatische val, maar voor de ringgeometrie van onze afremmer blijkt deze methode praktisch niet toepasbaar.

Een andere belangrijke tak op het gebied van koude moleculen betreft valexperimenten waarin ingevangen molecuulbundels coherent onderzocht worden met behulp van laserspectroscopie of gebruikt worden voor het bestuderen van gecontrolleerde scheikunde. Recente ontwikkelingen op het gebied van laserkoelen en invangen van verschillende molecuulsoorten laten veelbelovende methoden zien voor het verkrijgen van compacte en ultrakoude molecuulbundels. Een belangrijke paramater hierbij is de invangsnelheid, welke de voorwaarden bepaalt voor het laden van een traditionele optische of magnetische val. Een combinatie van een cryogene bron en Starkafremmer gevolgd door een korte periode van laserkoeling kan gebruikt worden om moleculen te laden in bijvoorbeeld een optische dipoolval, die onder zogenoemde “magische condities” toestandonafhankelijke invanging mogelijk maakt. Op deze manier kunnen grote aantallen zware laserkoelbare moleculen zoals SrF, BaF en eventueel polyatomische moleculen ingevangen worden in een optisch potentiaal voor langer dan één seconde. Dit is een veelbelovend beginpunt voor kleinschalige experimenten op zoek naar nieuwe natuurkunde met ongeëvenaarde precisie.

Acknowledgments

My long and exciting PhD research has come to an end. This thesis encompasses my scientific accomplishments that would not have been possible without the support of many people. The work presented here was performed in the Fundamental Interactions and Symmetries (FIS) group of the Van Swinderen Institute and funded by the Netherlands Organisation for Scientific Research (NWO). I would like to thank the Graduate School of Science and Engineering of the University of Groningen for offering a number of useful and well-organized courses on hard and soft skills. I also want to thank the facility management at KVI-CART for providing a healthy and safe working environment. I express special thanks to the skilled personnel of the KVI-CART mechanical workshop for manufacturing all required mechanical pieces.

I am first and foremost deeply indebted to my daily supervisor, Steven Hoekstra for his continuous support during all the years of my research.
Dear Steven, thank you so much for each piece of advice you gave me and for your patient guidance. It was a great pleasure for me to work in the challenging and motivating environment that you have established. And I greatly appreciate the freedom you have given me in running the experiment which helped to develop my professional skills and scientific intuition.

I also owe sincere gratitude to my co-promotor, Klaus Jungmann who offered much invaluable help and asked many insightful questions.
Dear Klaus, I always admired your way of thinking, dedication and enthusiasm. Thank you for the professional feedback and instructive discussions, which constantly motivated me during the course of my research.

I wish to acknowledge other senior staff members within the FIS group for inspiring attitude.
Dear Lorenz, thank you for offering prompt help on any experimental issues and suggesting apt solutions to solve them.
Dear Gerco, I appreciate your time and help on the statistical error analysis.

I would like to thank the members of the assessment committee, Prof. George Palasantzas, Prof. Elisabetta Pallante and Prof. Wim Ubachs for carefully reading my manuscript and making helpful suggestions to improve it.

I am sincerely thankful to Hilde van der Meer, whose positive attitude and professional support tremendously helped me to go through all the challenges of the university and government administrative formalities.

I feel a deep sense of gratitude to my colleagues in the Cold Molecules group, Joost and Corine for guiding me at the very beginning of my PhD and teaching how to operate complex laboratory equipment.

I want to offer my special thanks to my colleague and friend Sreekanth with whom I spent many days and evenings in the Coldmol lab trying to combat all challenges we faced.

Dear Sreekanth, it was a great pleasure to be in the same team aiming towards the same goals. I enjoyed both our scientific pursuits and the ping-pong sessions at 3 p.m. in the basement of KVI-CART.

I would like to thank my paranymphs for keeping me motivated and enthusiastic during the second half of my PhD.

Dear Parul and Kevin, I appreciate that we always were able to reach a consensus during our very interesting discussions. I really enjoyed exploring with you new places here in the Netherlands and even overseas. And I have no doubt that everything will go smoothly during my defense. Dear Kevin, thank you for translating the summary into Dutch.

I cannot imagine the successful accomplishment of this work without the technical support from Leo Huisman and Oliver Böll.

Dear Leo, you have given me so many useful tips on various matters that it is impossible to mention all of them here! I also appreciate your kind offer to give us a tour of Bedum, particularly of its local church, which, to my big surprise, has Europe's steepest leaning tower.

Dear Oliver, thank you for your countless pieces of advice on optics-related subjects and for sharing your experience with me.

And of course, I want to express my thanks to all former and current fellow colleagues within the FIS and eEDM groups for their encouragement and interesting discussions on both scientific and general topics: Amita, Anno, Auke, Carlos, Elwin, Ginny, Hidde, Janko, Jeroen, Kees, Lucas, Maarten, Mina, Nivedya, Olivier, Rutger, Sander, Thomas, Thya, and Yanning. I cannot help mentioning our paper discussion club and particularly colleagues from the Nijenborgh building who helped to broaden my knowledge on various theoretical aspects of molecular and particle physics: Anastasia, Pi, Yongliang, Malika, Yangyang, Alexander, and Diewertje. I also want to thank Rick Bethlem for many fruitful discussions.

I wish to thank the local programming gurus, Jeroen Muller and Mark Buisman for their great work in developing, adapting and testing the numerical simulation package.

For their support and encouragement, I am so utterly grateful to my Ukrainian friends whom I met amongst the Dutch: Dmitry Maksimenko, Dmitry Storozhuk, Daria, Maria, and Alexander. A special credit goes to Leonid for helping me to stay fit both mentally and physically.

I cannot forget to thank my close friend Dmitry Budkov who always supported me despite being miles away.

I would also like to express appreciation to my supervisor of the Bachelor's and Master's research projects, Leonid Levchuk who became my first mentor in the field of particle physics.

Undoubtedly, my school and university teachers instilled my sincere interest in science. Во-первых, хочу поблагодарить Оксану Михайловну Скачкову и Николая Григорьевича Гарбуза за то, что привили любовь к науке в общем и к физике в частности. Также выражаю благодарность всем своим школьным учителям Богодуховского лицея №3, а также профессорско-преподавательскому составу физико-технического факультета ХНУ им. Каразина, за ваш невероятный и почётный труд. Отдельное спасибо Тамаре Михайловне Мельниковой, Валерию Дмитриевичу Ходусову и Юрию Михайловичу Бережному.

And finally, I want to thank my beloved parents for their endless support, care and encouragement. Дорогие мама и папа! Спасибо вам за вашу безмерную поддержку и заботу. Спасибо за терпение и доброту. Вы прекрасно знаете, что я вряд ли добился бы таких высоких достижений, если бы не ваша мотивация, которую я всегда ощущал, даже на расстоянии. Надеюсь, что в плане образования оправдал все ваши ожидания.

Artem Zapara
April 2019, Groningen